Antenna Arrays for Co-channel Interference Mitigation in Wireless Communications

by

Thibaud Gabillard

A Thesis submitted in fulfilment of requirements for
the degree of Doctor of Philosophy (PhD)
and
the Diploma of Imperial College London (DIC)

October 2017

Supervisor: Prof. A. Manikas

Imperial College London

Department of Electrical and Electronic Engineering

Abstract

In this thesis, the capability of antenna arrays to combat co-channel interference is investigated. Initially, a parametric channel model based on the array manifold is presented and then exploited in various parts of the thesis. An emphasis is given to the impact of the antenna array geometry on the overall system performance, even in the case of systems that employ large antenna arrays (massive MIMO).

Furthermore, the worst-case scenario of an interfering signal being received within a small angular separation from a source is investigated. With this, the performance of a set of array geometries is ascertained for the tasks of detection, estimation and beamforming. Links between the performance metrics and the underlying array manifolds are made and it is demonstrated that some array manifold features are more desirable for certain tasks than others. This sets the ground for the design of novel antenna arrays that would be specialised for certain telecommunication tasks.

Then the novel concept of capacity loss, that is the loss of channel capacity due to the presence of interference is introduced and expressed as a function of the antenna array geometry and the signals directions of arrival. It is demonstrated that large antenna arrays with very long manifold curves do not necessarily perform the best, and smaller antenna arrays with optimised geometry could be considered instead.

Finally, the parametric channel model that the thesis is based upon is utilised to present a novel blind channel estimation and complete interference cancellation beamformer.

Throughout the thesis, extensive computer simulations are presented to analyse and illustrate the performance of the proposed algorithms.

Declaration of Originality

I hereby declare that this thesis is my own work. Where other sources of information have been used, they have been acknowledged.

Copyright Declaration

The copyright of this thesis rests with the author and is made available under a Creative Commons Attribution Non-Commercial No Derivatives licence. Researchers are free to copy, distribute or transmit the thesis on the condition that they attribute it, that they do not use it for commercial purposes and that they do not alter, transform or build upon it. For any reuse or redistribution, researchers must make clear to others the licence terms of this work.

Acknowledgments

A Ph.D is a very long journey that demands lots of sacrifices. I would like to take this opportunity to thank all the people who made this adventure possible, directly or indirectly.

Firstly, the warmest thanks go to my supervisor and mentor, Prof. Athanassios Manikas for his dedication and support throughout my Ph.D. His passion and enthusiasm inspired me to learn and push the limit of the field always further. Also, I would like to thank Charlotte and Prof. Holmes for their invaluable help with administrative matters.

I would like to express gratitude to my colleagues and friends in the array processing research group, Zexi Fang, He Ren, Akinbiyi Akindoyin, Evangelos Venieris and Cooper Liu, and particularly Vidhya Sridhar for the endless passionate discussions we had throughout the projects we did together. In the wider research group, Jinwen, Hamdi, Georgia, John, David, Mudasar, Apit, Therasak, Wilhem and Enrico for their friendships and also my friend Maxime Ferreira Da Costa for his encyclopaedic knowledge and our passionate discussions about Maths. My thanks also go to my colleague and dear friend Mohamed Mikaty for his excellent friendship and all our exciting lunchtime conversations.

I wouldn't be who I am without my parents, Annie and Daniel,

who never hesitated to invest all their efforts and heart into their children. Also, I would like to have a particular thought about my grandparents, Jean, Madeleine, Eli and Jeanne who instilled me the thirst for knowledge and the importance of education; I hope to make the best use of their legacy. I would also like to thank the great Michel et Véronique, for teaching me how to appreciate life, and especially good food and wine. Nonetheless, I would like to have a special word for my brother, Baptiste, this amazingly strong and inspiring person, for all the fantastic discussions we had together.

I owe a great debt of gratitude to the fantastic Marie, for her patience tolerating my unforgiving work schedule and for steadying the ship whenever I started tearing my hair out. Her unlimited support and attention largely contributed to the quality of my PhD.

I would also like to thank Yukiko, Adrien, Kirsten, Emy, Khaled, Philippe, Cynthia, Natasha und Matthias, Peter, Laura, Carla, Audrey, Carolyn and Gerald and all our London friends who contributed greatly to make our time in London so special. Finally, I would like to express my gratitude to all the teachers who contributed to my curriculum throughout the years, and, particularly, I would like to acknowledge Mr Lopez, my primary school teacher, who instilled in me the passion for questioning everything and thinking on my own.

Table of Contents

Abstract **2**
Declaration of Originality **3**
Acknowledgments **5**
Table of Contents **7**
List of Figures **10**
List of Tables **13**
Publications Related to this Thesis **14**
List of Notations **15**
List of Main Symbols **16**
List of Abbreviations **17**
Chapter 1 Introduction **19**
1.1 Massive MIMO 20
1.2 Parametric Signal Modelling 23
1.3 Thesis Scope and Organisation 24
Chapter 2 The Array Manifold **25**
2.1 MIMO Channel Modelling 25
2.2 The Array Manifold 31
2.2.1 Array Manifold Curves 32
2.2.2 The Frame and Cartan Matrices 32
2.2.3 Hyperhelical Curves 34
2.3 Inner Products on the Array Manifold 37

2.3.1 Approximation with Geodesic and Euclidean Distances 38
2.3.2 Inner Product and Manifold Radii 40
2.3.3 Inner Product on the α and β-Curves 42
2.4 Summary 44
Chapter 3 Importance of the Antenna Arrays Geometries 45
3.1 Introduction 46
3.2 Preliminary Tasks of Wireless Communication Systems 48
3.3 Beamforming Performance with Antenna Arrays . . . 55
3.3.1 Steering Vector Beamformer 55
3.3.2 Null Beamformer 58
3.4 Summary 62
Chapter 4 Channel Capacity Loss 63
4.1 Introduction 63
4.2 Channel Capacity Loss 65
4.2.1 Second Order Statistics 65
4.2.2 Mutual Information and MIMO Channel . . . 66
4.2.3 The Loss of Channel Capacity 68
4.3 Evaluation of Capacity Loss on Curves 69
4.3.1 Capacity Loss on Hyperhelical Curves 79
4.3.2 Capacity Loss Threshold 79
4.4 Summary 82
Appendix 4.A Structure of Eq. 4.16 83
Appendix 4.B Proof of the Capacity Loss Threshold 85

Chapter 5 Spatiotemporal Channel Estimator and Beamformer for 5G **86**

5.1 Introduction 87

5.1.1 mmWave Beamformers and 5G 87

5.1.2 Extension of Degrees of Freedom and Interference Cancellation 88

5.1.3 Parametric Channel Estimation 91

5.2 MIMO Communications System Model 94

5.2.1 Transmitter Model 94

5.2.2 Simplification to Single-Carrier System: . . . 97

5.2.3 Channel Model Based on the Manifold Vectors 99

5.2.4 Receiver Model 101

5.2.5 Fundamental Performance Bounds 106

5.3 Proposed Spatiotemporal Beamformer Design 107

5.3.1 Joint Delay-Velocity Estimation 109

5.3.2 DOA Estimation 110

5.3.3 Combined Fading Coefficient Estimation . . . 111

5.3.4 Design of the Rx Spatiotemporal Beamformer Weights 113

5.4 Computer Simulation Studies 115

5.4.1 Channel Estimation Studies 116

5.4.2 Reception Studies 119

5.5 Summary 125

Chapter 6 Conclusions and Further Work **126**

6.1 List of Contributions 128

6.2 Suggestions for Further Work 129

References **131**

List of Figures

2.1 The multipath multiuser MIMO channel. 26
2.2 Baseband parametric representation of the multiuser MIMO channel. 29
2.3 The antenna array geometries that will be examined in this thesis. 30
2.4 Illustration of a manifold p-curve embedded in the N-dimensional complex space. 33
2.5 Two array manifold vectors and the circular approximation of the manifold curve joining their corresponding points. 38

3.1 The tasks of a receiver utilising an antenna array. . . 47
3.2 Illustration of two sources on the manifold surface. . 49
3.3 Probabilities of detection 50
3.4 Two-sources detection thresholds versus varying elevation angle and equal azimutal and elevation separations. 51
3.5 Two-sources detection thresholds versus varying elevation angle and different azimutal and elevation separations. 51
3.6 Illustration of MUSIC performance when approaching the resolution threshold. 53

3.7 Comparison of the resolution threshold versus varying azimuth angle. 53
3.8 Comparison of the resolution threshold versus varying elevation angle. 54
3.9 Comparisons of the performance of steering vector beamformer against the array geometries of Fig. 2.3 for varying elevation angles. 57
3.10 Comparisons of the performance of steering vector beamformer against the array geometries of Fig. 2.3 for varying azimuth angles. 58
3.11 Comparisons of the performance of subspace vector beamformer against the array geometries of Fig. 2.3 for elevation angles. 60
3.12 Comparison between the steering vector beamformer and subspace-based beamformer 61

4.1 Representation of the M users manifold vectors on the manifold θ-curve. 71
4.2 Capacity loss for the second set of geometries 73
4.3 Capacity loss for the first set of geometries 75
4.4 Capacity loss for varying number of users. 77
4.5 Capacity loss for the case that the desired user is located at the center of the interferer cluster. 78
4.6 Illustration of the capacity loss threshold 81

5.1 Basic representation of the proposed system consisting of signal design. 93
5.2 Baseband representation of the transmitter and the MIMO channel. 95

5.3 The 3D data cube and its vectorisation to form the spatiotemporal snapshot x. 97
5.4 Baseband representation of the transmitter and the MIMO channel for the i-th user of the SC-DS-CDMA system. 98
5.5 Block diagram of the preprocessor, channel estimator and beamformer. 102
5.6 Desired user's channel parameter estimation. 117
5.7 Evaluation of the proposed spatiotemporal estimator algorithm. 118
5.8 Comparison of the beampatterns of the proposed Doppler-STAR approach and a spatial-only massive MIMO system. 120
5.9 Beampattern of a spatiotemporal massive MIMO system with 500 antennas. 121
5.10 Comparison of the beampatterns of the proposed Doppler-STAR approach and a spatial-only massive MIMO system in a scenario where two multipaths arrive with the same DOA albeit different path delays 122
5.11 Comparative study of the performance of the proposed Doppler-STAR subspace receiver with other spatiotemporal and spatial-only receivers in terms of the NFR. (200 trials). 123
5.12 Performance of the Doppler-STAR-subspace receiver with varying number of subcarriers and data copy over subcarriers (50 trials). 124

List of Tables

2.1 Approximations of the inner product between two array manifold vectors 39

3.1 Performance ranking of antenna array geometries for the task of detection 50

4.1 Comparison (ranking) of the two sets of five array geometries based on the capacity loss. 74

5.1 Simulation Parameters 116

Publications Related to this Thesis

The following papers were published during the PhD:

1. T. Gabillard, V. Sridhar and A. Manikas, "*Capacity Loss and Antenna Array Geometry*", in *Processing of IEEE International Conference on Communications (ICC)*, May 2017, Paris, France. [1]

2. V. Sridhar, T. Gabillard and A. Manikas, "*Spatiotemporal-MIMO channel estimator and beamformer for 5G*", *IEEE Transactions Wireless Communications*, vol. 15, no. 12, pp. 8025–8038, Dec. 2016. [2]

3. T. Gabillard, V. Sridhar and A. Manikas, "*Comparative Study of 2D Grid Antenna Array Geometries for Massive Array Systems*", in *Proceedings of IEEE Global Conference on Communications (GLOBECOM)*, Dec. 2015, San Diego, USA. [3]

List of Notations

a, A	Scalar
$\underline{a}$, $\underline{A}$	Column Vector
$\mathbf{a}$, $\mathbb{A}$	Matrix
$(\cdot)^*$	Conjugate
$(\cdot)^T$, $(\cdot)^H$	Transpose and Hermitian transpose
$\hat{(\cdot)}$, $\tilde{(\cdot)}$	Nominal values and uncertainties
$\exp(\underline{A})$	Element by element exponential of vector $\underline{A}$
$\underline{A}^b$	Element by element power
$\text{row}_k(\mathbb{A})$	k^{th} row of the matrix $\mathbb{A}$
$\lvert\cdot\rvert$	Absolute value
$\lVert\underline{A}\rVert$	Euclidean norm of vector $\underline{A}$
$\text{Trace}(\mathbb{A})$	Trace of matrix $\mathbb{A}$
$\mathcal{E}\{\cdot\}$	Expectation operator
$\simeq$	Approximately equal
$\odot$	Hadamard product
$\otimes$	Kronecker product
$\underline{0}_N$	Column vector of N zeros
$\underline{1}_N$	Column vector of N ones
$\mathbb{I}_N$	$N \times N$ Identity matrix
$\mathbb{O}_N$	$N \times N$ Matrix of zeros
$\text{expm}\{\mathbb{A}\}$	Matrix exponential of the matrix $\mathbb{A}$

List of Main Symbols

$\mathcal{A}$	Array manifold
$\underline{\mathrm{a}}$, $\underline{S}$	Array manifold vector
$\mathbb{C}$	Cartan matrix
C	Channel capacity
i	Index for the i-th user
j	Index for the j-th subcarrier
k	Index for the k-th multipath
L	Number of snapshots
M	Number of signals
N	Number of antenna element of the RX array
$\overline{N}$	Number of antenna element of the TX array
$\mathbf{r}$	Cartesian coordinates of the antennas of an array
s	Array manifold arc length
$\underline{x}$	Received signal vector
α, β	Cone-angle propagation parameters
θ, ϕ	Azimuth and elevation angles
κ_i	Curvature (i-th)

List of Abbreviations

AIC	Akaike information criterion
AWGN	additive white Gaussian noise
BER	bit error rate
CDMA	code division multiple access
CRB	Cramer-Rao lower bound
CSI	channel state information
CP	cyclic prefix
DOA	direction of arrival
DOD	direction of departure
GNSS	global navigation satellite system
HSPA	high speed packet access
IEEE	Institute of Electrical and Electronics Engineers
ISI	inter symbol interference
LOS	line-of-sight
LTE-A	long term evolution - advanced
MAI	multiple access interference
MIMO	multiple-input multiple-output
MUSIC	multiple signal classification
ML	maximum likelihood
mm-wave	millimetre-wave
NFR	near-far ratio

NLOS	non-line-of-sight
RMSE	root mean square error
SNIR	signal-to-noise-plus-interference ratio
SNR	signal-to-noise ratio
STAR	spatiotemporal array
TDL	tapped-delay line
TOA	time of arrival
UCA	uniform circular array
ULA	uniform linear array
WCDMA	wideband code division multiple access

Chapter 1

Introduction

The plans for network densification, the booming popularity of mobile data on smartphones and tablets, and the generalisation of embedded internet connections (the internet of things) are about to change the wireless landscape completely. The number of devices making use of mobile networks is predicted to explode, creating congestions and degrading spectral efficiency dramatically. These forecasts on very high co-channel interferences are one of the greatest challenges of the future generations of mobile communication [4].

In this context, multiple-antenna systems are undoubtedly one of the major solutions to provide very high spectral efficiency. They have been playing a role in modern mobile telecommunication standards such as 3G, 3.5 and 4G mobile communication systems with WCDMA, HSPA, HSPA+ and LTE-A [5] and they will be a big part of 5G, undoubtedly [6], but also part of other wireless systems. On the satellite communications side, multiple-antenna systems contribute significantly to the performance of the new generation of high throughput satellites [7, 8], to the new GNSS systems [9], the multimedia service [10] and in inter-satellite links [11]. On RADAR, the

synthetic aperture radars are very popular [12]. In radio-astronomy, antenna arrays are coupled with large reflectors to achieve both high gain and selectivity [13, 14]. They are also used for marine exploration, where ships drag large towed-arrays [15].

This concept exploits the spatial domain to discriminate the users and/or utilise the spatial diversity offered by the channel. In a multiuser environment, all can transmit at the same time on the same frequency band.

1.1 Massive MIMO

A major part of the wireless communication literature dedicated to multiple-antennas systems refers to the probabilistic i.i.d (independent and identically distributed) channel model, where each antenna experiences independent fading. One of the early analysis of the capacity of multiple-antenna communication systems was made by Foschini and Gans [16]. This approach, based on the Rayleigh fading model, is an idealised representation of the multiple-antenna propagation channel where the antennas are modelled as decorrelated by the propagation environment and assumed to be composed of a considerable number of scatterers. Given this, the point-to-point high-SNR regime Shannon channel capacity scales linearly with the number of antennas. As described in [17], this model tailored for systems where the base-station is elevated and unobstructed and local scatterers surround each of the users.

To accommodate more users, it was recently proposed to drastically increase the number of antennas [6]; these systems utilise large antenna arrays and are called massive MIMO (MaMI). Noticeably,

when the number of antennas is large, and the propagation channel is assumed to be experiencing i.i.d fading, the distribution of the channel Eigenvalues follows a deterministic function, borrowed from the random matrix theory [18]. In [19], computer simulation studies were provided to display the i.i.d channel model in the case where the base-station was operating with 100 antenna elements and the channel was composed of 400 scatterers. An analysis of the inter-cell interference brought by the so-called pilot contamination was made in [20].

More recently, the i.i.d channel model has been reported to be unrealistic by recent measurement campaign [21, 22] for MaMIs, as the scattering environment cannot be rich enough. An outdoor measurement campaign with a 128 antenna element cylindrical antenna array base station was presented in [23]. The user-side comprised of 8 pedestrians holding a single-antenna handset and moving slowly within a 5-m circle. The separability of the users as a function of the number of antenna elements of the base station was examined by studying the singular value spread of the channel matrix. This analysis was extended in [24], where a comparison with i.i.d Rayleigh fading was made, and, in [25], a uniform linear array (with 128 omni-directional elements) and a cylindrical antenna array base station (with 64 dual-polarised elements), all-together in half-wavelength spacing. They were employed to receive eight handsets roughly distributed uniformly in the field of view. Several fundamental comments were made:

(A) It was reported in [24] that the discrepancy between the i.i.d Rayleigh fading and real measurement is exacerbated when the

users are closely spaced in the angular domain, in the LOS scenario,

(B) It was observed in [25] that the contribution of each antenna was very different and that a large number could be turned off without any significant loss of performance,

To address this, a series of publications intended to improve the channel modelling when the number of multipath is equal to or inferior to the number of antennas. This was modelled in terms of correlations matrices introduced by the antennas locations [26, 27, 28] and by assuming Laplacian distributions of the signals DOA around the principal signals' DOA [29, 30]. However, the analysis from this model is made difficult, particularly because the transmit and receive correlation cannot be distinguished.

A series of research modelled the correlation with the Kronecker model [31, 32, 33]. But it was reported in [34] that this model underestimates the channel capacity systematically. For more details about this model, please refer to [35].

In more recent studies, the asymptotic case was considered when the number of antennas grows very large [36, 37]. In [38], the capacity of a MIMO channel with a finite number of scatterers was considered, with the number of Tx/Rx antennas growing to infinity. Furthermore, several papers have investigated the effect of both antenna correlation and co-channel interference simultaneously and hence helping the separability of the sources [39, 40, 41, 42].

Nevertheless, statistical techniques don't give clear insights into (A) and (B). The effect of the antenna array geometry on the capability to mitigate interference is missing and hence a deterministic

characterisation of the impact of the interference is not possible.

As an illustrative example, in [25], it was concluded that given the large difference between the theoretical i.i.d Rayleigh and the real measurement, a new MIMO propagation model would be useful.

1.2 Parametric Signal Modelling

Utilising parametric channel models present many advantages compared to statistical models, and the most obvious advantages are their ability to deliver an intelligible and tractable analysis of what constitutes the performance of a particular system. The multiple-antenna wireless communication literature poses a handful of contributions utilising parametric models, like [43] and [44], but without giving special attention to the array geometry. Excellent comparisons between channel models can be found in [45, 35].

On the other hand, the array processing literature proposes a powerful framework called the antenna array manifold [46], that provides a complete characterisation of the underlying antenna array. In this framework, the array response is a mathematical object embedded in a high dimensional complex space and is function of a set of parameters that characterises the propagation environment. This framework yields a complete analytical description of the entire communication system and a comprehensive analysis of the performance of arrayed systems facing interference.

1.3 Thesis Scope and Organisation

This thesis is concerned with antenna arrays and their use to combat co-channel interference in a very dense signal environment. The main assumption is that the antenna arrays are fully calibrated. The outline of this thesis is the following. In Chapter 2, the framework of antenna array manifold is presented, its most important underlying parameters are introduced along with theoretical results about array manifold curves. In Chapter 3, the importance of the array geometry is assessed against several communication tasks, and also through their beamsteering and subspace-based beamforming performance. In Chapter 4, the impact of the presence of interference on the channel capacity is ascertained, and the influence of the array geometry is studied. Lastly, in Chapter 5, a novel space-time channel estimator and space-time beamformer that is suitable for the environment of 5G are proposed and their performances are ascertained. Finally, in Chapter 6, the main contributions of the thesis are presented, the conclusions are drawn and ideas for further work are presented.

Chapter 2

The Array Manifold

This chapter is concerned with presenting the generic MIMO channel model, the framework of the array manifold and new theoretical derivations that will be employed in the later chapters. Section 2.1 presents the generic MIMO channel model and offers a description of the array geometries that are utilised in this thesis as examples Section 2.2 presents the array manifold as a mathematical object, along with novel characterisations. Section 2.3, based on the theory introduced in Section 2.2, is dedicated to describing the inner products between array manifold vectors. Novel results that will be crucial for the rest of the thesis are presented.

2.1 MIMO Channel Modelling

An array of N antennas operating in the presence of M co-channel users is considered and each user utilises an antenna array to transmit a set of $\mathcal{N}_{sc}$ subcarriers. We use the subscripts i, j and k to index the users, subcarriers and multipath respectively (i-th user, k-th multipath and j-th subcarrier). The signals of each user experience a severe multipath fading of K_i multipath (frequency selective channel).

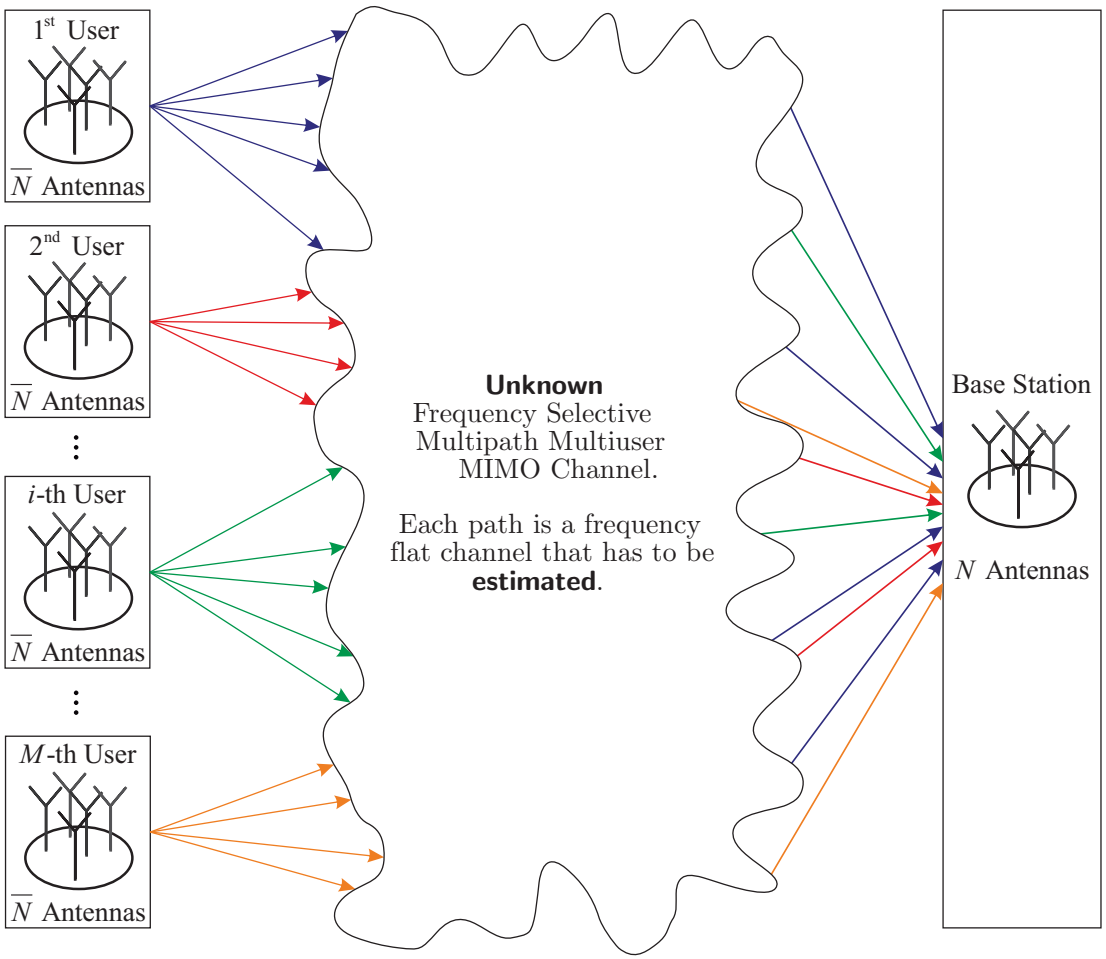


Figure 2.1: The multipath multiuser MIMO channel.

Figure 2.1 provides a conceptual illustration of a multipath multiuser MIMO system/channel. We adopt the general channel modelling assumption that the electromagnetic field is a superposition of plane waves [47]. It is also assumed that the first user is the "desired" user (i.e. index $i = 1$) and the $M - 1$ other users ($i \in [2, M]$) are co-channel interference. The $(N \times 1)$ complex vector $\underline{a}$ that is termed as antenna array manifold vector, or antenna array response vector, is the response of the receive antenna array to a plane-wave arriving from the direction of arrival (DOA) parametrised by an azimuth θ

and elevation ϕ. This complex vector is formally defined as

$$\underline{\mathrm{a}} \triangleq \underline{\mathrm{a}}\left(\theta, \phi, F_j\right) \triangleq \exp\left(-j2\pi \frac{F_c + F_j}{c} \mathbf{r}\underline{u}(\theta,\phi)\right), \tag{2.1}$$

where F_c and F_j are the central and subcarrier frequencies, and where $\underline{u}(\theta, \phi)$ denotes the vector pointing towards the direction (θ, ϕ) as

$$\underline{u}(\theta, \phi) \triangleq \left[\cos\theta\cos\phi, \sin\theta\cos\phi, \sin\phi\right]^T. \tag{2.2}$$

Let us now come back to the general case. The real matrix $\mathbf{r}$ is used to denote the x-y-z Cartesian coordinates of the N antennas in meters, and it is defined as

$$\mathbf{r} = \left[\underline{r}_x, \underline{r}_y, \underline{r}_z\right] \in \mathcal{R}^{N\times 3} \tag{2.3}$$

where $\underline{r}_x$, $\underline{r}_y$ and $\underline{r}_z$ are the coordinates of the N sensors in the x, y and z direction respectively. Alternatively, the antenna array geometry can be presented as

$$\mathbf{r} = \left[\underline{r}_1, \underline{r}_2, \ldots, \underline{r}_N\right]^T, \tag{2.4}$$

where $\underline{r}_k \in \mathcal{R}^{3\times 1}$ is the location of the m-th antenna[1]. There is a variety of interesting classes of antenna array geometries that have symmetrical properties and convenient analytical simplifications. An important class of antenna array geometry called *3D-grid array* was formally defined in [46] by their common property

$$\left[\underline{r}_x, \underline{r}_y, \underline{r}_z\right]^T \left[\underline{r}_x, \underline{r}_y, \underline{r}_z\right] = \rho^2 \mathbb{I}_3 \text{ where } \rho \in \mathcal{R}. \tag{2.5}$$

The antennas location vectors $\underline{r}_x$, $\underline{r}_y$ and $\underline{r}_z$ have equal norms and the antenna array centroid is chosen as the array reference point, yielding

$$\underline{r}_x^T \underline{1}_N = \underline{r}_y^T \underline{1}_N = \underline{r}_z^T \underline{1}_N = 0. \tag{2.6}$$

[1]Please note that the terms sensor and antenna are used interchangeably.

Alternatively, a *2D-grid array* is a special case of 3D-grid arrays where $\underline{r}_z = 0$.

We use a "bar" at the top of a symbol to denote all equivalent parameters associated with the transmit side, and we define the transmit array manifold $\underline{\overline{\mathrm{a}}}$ and pointing vector $\underline{\overline{u}}$ similarly to Eqs. 2.1 and 2.2, with the associated direction of departure (DOD) ($\overline{\theta}$ and $\overline{\phi}$), and the transmit geometry $\left[\overline{r}_x, \overline{r}_y, \overline{r}_z\right] \in \mathcal{R}^{\overline{N}\times 3}$ as

$$\underline{\overline{\mathrm{a}}} \triangleq \underline{\overline{\mathrm{a}}}\left(\overline{\theta}, \overline{\phi}, F_j\right) \triangleq \exp\left(-j2\pi \frac{F_c + F_j}{c} \left[\overline{r}_x, \overline{r}_y, \overline{r}_z\right] \underline{\overline{u}}(\overline{\theta}, \overline{\phi})\right), \tag{2.7}$$

and

$$\underline{\overline{u}}(\overline{\theta}, \overline{\phi}) \triangleq \left[\cos\overline{\theta}\cos\overline{\phi}, \sin\overline{\theta}\cos\overline{\phi}, \sin\overline{\phi}\right]^T. \tag{2.8}$$

As mentioned earlier, with this framework, the antenna array geometry $\mathbf{r}$ is a central component of the framework.

The channel's branches are modelled in terms of a Tx and Rx antenna array manifold vectors $\underline{\mathrm{a}}_{ijk}$ and $\underline{\overline{\mathrm{a}}}_{ijk}$ respectively, a Doppler frequency shift $\mathcal{F}_{ijk}$, a time delay τ_{ik} and a path fading coefficient β_{ijk}.

The vector-signal received by the antenna array at instant t can be expressed as follows

$$\underline{x}(t) = \sum_{i=1}^{M} \sum_{j=1}^{\mathcal{N}_{\mathrm{sc}}} \sum_{k=1}^{K_i} \beta_{ijk} \exp\left(\mathrm{j}2\pi\mathcal{F}_{ijk}t\right) \underline{\mathrm{a}}_{ijk} \underline{\overline{\mathrm{a}}}_{ijk}^H \times \left(\underline{\overline{w}}_{ij} \odot \underline{m}_{ij}(t - \tau_{ijk})\right) + \underline{\mathrm{n}}(t), \tag{2.9}$$

where $\underline{m}_{ij}(t) \in \mathcal{C}^{\overline{N}\times 1}$ and $\underline{\overline{w}}_{ij}$ represent the baseband signal transmitted and the transmit weights over the j-th subcarrier by the i-th user respectively. Also, $\underline{\mathrm{n}}(t)$ is the AWGN channel noise at instant t. Figure 2.2 gives a representation of the i-th user's channel model. The antenna array geometries that are to be utilised as examples are

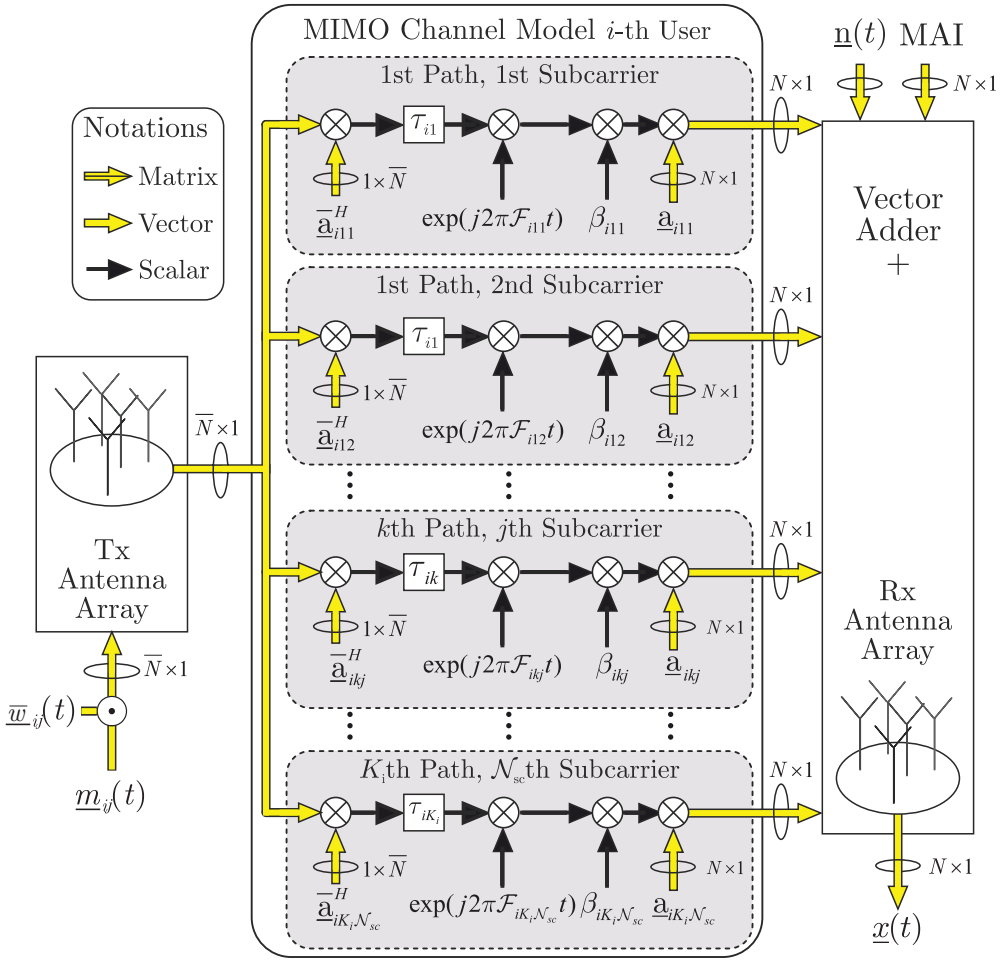
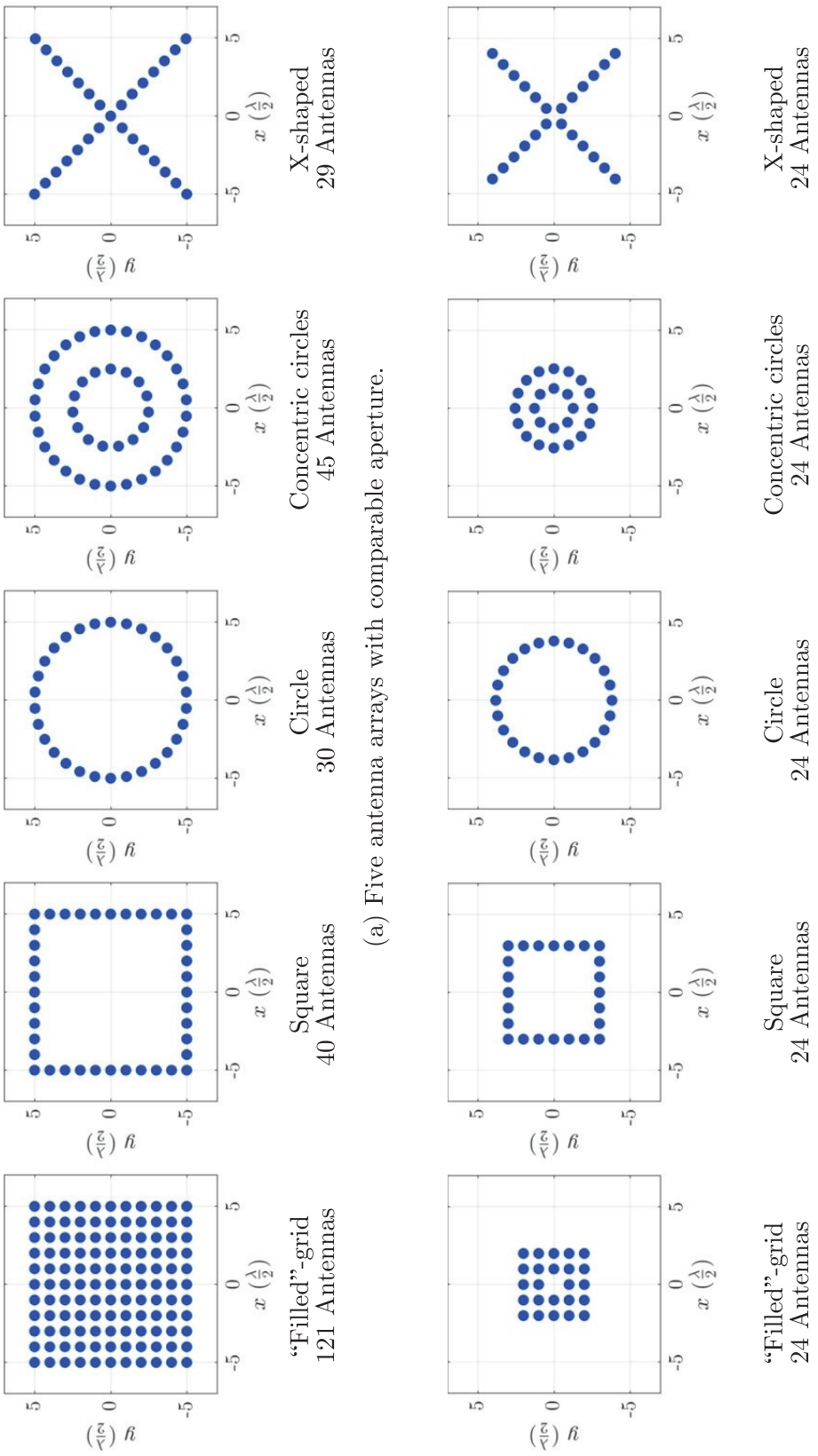


Figure 2.2: Baseband representation of the MIMO channel for the i-th user. The channel is modelled in terms of the Tx and Rx array manifold vectors, a path delay, a Doppler frequency shift and a complex path fading coefficient.

presented in Fig. 2.3. They have been constructed from five shapes that are the "filled"-grid, the square, the circle, the concentric circles and the X-shaped. The geometries presented above belong to the class of 2D-grid arrays. Figure 2.3.a presents the design of these five shapes for a different number of antennas and similar aperture. On the other hand, on Fig. 2.3.b, the array geometries have the same number of sensors but different apertures.



(a) Five antenna arrays with comparable aperture.

(b) Five antenna arrays with constant number of antennas(N = 24).

Figure 2.3: The antenna array geometries that will be examined in this thesis.

2.2 The Array Manifold

It is important to note that, although the (θ, ϕ) parametrisation is the most popular, other formulations exist. This is why, for the sake of generality, the array manifold vector is simply denoted as $\underline{\mathrm{a}}(\underline{p})$, where $\underline{p}$ is a vector of parameters. We formally define the mathematical object of antenna array manifold as follows

Definition 1 (Antenna Array Manifold)**.** *The locus of all the array manifold vectors for the range of parameters $\underline{p}$ called antenna array manifold or simply array manifold, is denoted as $\mathcal{A}$, and defined as*

$$\mathcal{A} \triangleq \left\{\underline{\mathrm{a}}(\underline{p}), \forall \underline{p} \in \Omega_{\underline{p}}\right\}. \tag{2.10}$$

The M array manifold vectors of the corresponding M sources lie onto this mathematical object. Hence, its study is of primary importance as it defines the distances between the response vectors $\underline{\mathrm{a}}_i$ of Eq. 2.9, and intrinsically the ability of the receiver to extract the desired message $m_1(t)$ from the antenna array output $\underline{x}(t)$.
The array manifold can be function of one or several propagation parameters. When the locus of the array manifold vectors is function of one parameter, i.e. $\underline{p} = p$, the array manifold is a curve embedded in N complex dimensions $\mathcal{C}^N$, termed as the p-curve. For two parameters, the array manifold is a surface. The study of the geometrical properties of array manifold surfaces are more difficult than the curves, nevertheless it has been previously demonstrated that an array manifold surface can be described by a family of constant-parameter curves [46].

2.2.1 Array Manifold Curves

While considering a family of curves, we utilise the "dot" to define the first derivative with respect to the parameter p, i.e.,

$$\dot{\underline{\mathrm{a}}}(p) \triangleq \frac{d\underline{\mathrm{a}}(p)}{dp}. \tag{2.11}$$

While studying the array manifold p-curve, the length of the arc in the N-dimensional complex space is of particular interest. We define the length $s(p)$ of a particular p-curve of the array manifold $\mathcal{A}$ from its origin as

$$s(p) \triangleq \int_{p_o}^{p} \|\dot{\underline{\mathrm{a}}}(\mathrm{p})\| \, d\mathrm{p}, \tag{2.12}$$

where $p_0 = 0$ and the rate of change of arc length $\dot{s}(p)$ is

$$\dot{s}(p) \triangleq \|\dot{\underline{\mathrm{a}}}(p)\| \,. \tag{2.13}$$

Figure 2.4 gives an illustration of the particular array manifold p-curve. The length of the arc offers an alternative way of parametrising the array manifold, $\underline{\mathrm{a}}(s)$. We denote the derivative of the array manifold vector with respect to its length with a "prime". That is,

$$\underline{\mathrm{a}}'(s) \triangleq \frac{d\underline{\mathrm{a}}(s)}{ds}. \tag{2.14}$$

Parametrising the manifold in terms of the length presents many advantages, since the parameter s is invariant (i.e. $\|\underline{\mathrm{a}}'(s)\| = 1$) and the norm of the resulting tangent vector is constant and unitary.

2.2.2 The Frame and Cartan Matrices

Given the *Fundamental Theorem of Space Curves*, a p-curve on the array manifold $\mathcal{A}$ can be described in a complete manner with its

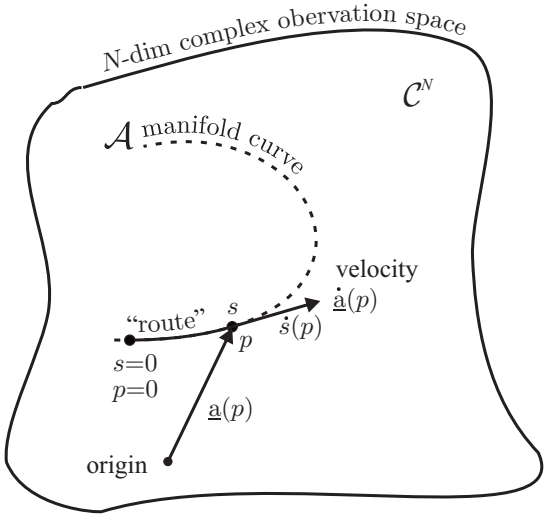


Figure 2.4: Illustration of a manifold p-curve embedded in the N-dimensional complex space.

length $s(p)$ and its d curvatures. Please refer to [46] for more informations about d. At a point s the *frame* matrix $\mathbb{U}(s)$ forms a basis of the tangent space to the array manifold p-curve at point s as follows:

$$\mathbb{U}(s) \triangleq [\underline{u}_1(s), \underline{u}_2(s), \ldots, \underline{u}_N(s)]\,. \tag{2.15}$$

Furthermore, the matrix $\mathbb{U}'(s)$ that contains the derivatives of the coordinates vectors, as

$$\mathbb{U}'(s) \triangleq [\underline{u}'_1(s), \underline{u}'_2(s), \ldots, \underline{u}'_N(s)]\,, \tag{2.16}$$

and this gives the set of *Frenet Equations*

$$\mathbb{U}'(s) = \mathbb{U}(s)\mathbb{C}(s), \tag{2.17}$$

with $\mathbb{C}(s)$ being the important *Cartan Matrix* which is defined as

$$\mathbb{C}(s) \triangleq \begin{bmatrix} \underline{u}_1^H \underline{u}_1'(s), & -\kappa_1(s), & 0, & \dots & 0, & 0 \\ \kappa_1(s), & \underline{u}_2^H \underline{u}_2'(s), & -\kappa_2(s), & \dots & 0, & 0 \\ 0, & \kappa_2(s), & \underline{u}_3^H \underline{u}_3'(s), & \dots & 0, & 0 \\ \vdots & \vdots & \vdots & \ddots & \vdots & \vdots \\ 0, & 0, & 0, & \dots & \underline{u}_{N-1}^H \underline{u}_{N-1}'(s), & -\kappa_{N-1}(s) \\ 0, & 0, & 0, & \dots & \kappa_{N-1}(s), & \underline{u}_N^H \underline{u}_N'(s) \end{bmatrix}. \tag{2.18}$$

Here, the Cartan matrix offers a linear mapping between the frame matrix and its derivative. The diagonal and purely imaginary elements of the Cartan matrix described in 2.18 are a consequence of the orientation of the array manifold, that is, the angle between the array manifold vector $\underline{\mathrm{a}}(s)$ and the linear space spanned by the columns of the matrix $\mathbb{U}$, i.e. $\mathcal{L}[\mathbb{U}(s)]$. Interestingly, when the antenna array is a grid array, the Cartan matrix becomes real with a null diagonal.

However, the analysis of the generic p-curves is a difficult task, particularly because their curvatures $\kappa_i(s)$ are complicated to track, due to the fact that they vary along the curve.

2.2.3 Hyperhelical Curves

A class of array manifold curves of constant curvatures are the *hyperhelical curves*. For reference, the concept of hyperhelical curve was first introduced in [46] and more formally described in [48].

Definition 2 (Hyperhelical Curve)**.** *An array manifold $\mathcal{A}$ is a hyperhelix in the parameter interval Ω_p if and only there is a constant*

real vector $\underline{\tilde{r}} \in \mathcal{R}^{N\times 1}$ *and a constant complex vector* $\underline{v} \in \mathcal{C}^{N\times 1}$ *that obey*

$$\|\underline{v} \odot \underline{\tilde{r}}\| = 1 \tag{2.19}$$

$$\text{sum}\{\underline{\tilde{r}}\} = 0 \tag{2.20}$$

such as

$$\underline{\mathrm{a}}(s) = \underline{v} \odot \exp\left(j\underline{\tilde{r}} \cdot s\right) \in \mathcal{C}^{N\times 1} \tag{2.21}$$

is a natural representation of $\mathcal{A}$*.*

This definition can be rewritten as[2]

$$\underline{\mathrm{a}}(s) = \exp\left(j\left(\underline{\tilde{r}}s - \pi\underline{r} + \underline{v}\right)\right), \tag{2.22}$$

where $\underline{r}$ and $\underline{v}$ are constant vectors independent of the parameter s, and $\underline{\tilde{r}}$ is a normalisation of $\underline{r}$,

$$\underline{\tilde{r}} \triangleq \frac{\underline{r}}{\|\underline{r}\|}. \tag{2.23}$$

On these special curves, the analysis of the array manifold is made easier because of the linear mapping between the frame matrix and its derivative is constant (the Cartan matrix $\mathbb{C}$ is invariant with s). In this case, the length of the arc $s(p)$, as defined by Eq. 2.12, is

$$s(p) = \pi\|\underline{r}\|\left(1 - \cos p\right), \tag{2.24}$$

and the rate-of-change of the arc length with respect to the parameter can be simply derived as (see footnote)

$$\dot{s}(p) = \|\pi\underline{r}\sin p \odot \underline{\mathrm{a}}(p)\| = \pi\|\underline{r}\|\sin p. \tag{2.25}$$

A particular parametrisation called cone-angle can be employed to have the hyperhelical properties of both parameters for planar

[2]And can be also written as $\underline{\mathrm{a}}(p) = \exp\left(-j\left(\pi\underline{r}\cos p + \underline{v}\right)\right)$.

array geometries [46]. This transformation is a rotation of the x-y plane by an angle of Θ into a new $\check{x}$-$\check{y}$ plane that is parametrised by (α, β). The new (α, β) parameters are expressed as

$$\cos\alpha = \cos\phi\cos\left(\theta - \Theta\right) \tag{2.26a}$$

$$\cos\beta = \cos\phi\sin\left(\theta - \Theta\right), \tag{2.26b}$$

and the rotation Θ is

$$\Theta = \tan^{-1}\left(\frac{\cos\phi_1\cos\theta_1 - \cos\phi_2\cos\theta_2}{\cos\phi_2\sin\theta_2 - \cos\phi_1\sin\theta_1}\right). \tag{2.27}$$

One can note that this transformation is independent of the geometry. The array geometry $\mathbf{r}$ of the x-y-z planes is rotated to the new Cartesian frame with

$$\underline{r}(\Theta) \triangleq \underline{r}_x\cos\Theta + \underline{r}_y\sin\Theta, \tag{2.28}$$

and the new wavenumber vector (equivalent to the one introduced in Eq. 2.2) can be written as

$$\underline{\check{k}}(\alpha,\beta) = \pi\left[\cos\alpha, \cos\beta, \sqrt{1-\cos^2\alpha-\cos^2\beta}\right]^T. \tag{2.29}$$

In this case, the array manifold vector can be written with the new transformation as

$$\underline{\mathrm{a}}(\alpha,\beta) = \exp\left(-j\pi\left(\underline{r}(\Theta)\cos\alpha + \underline{r}\left(\Theta+\frac{\pi}{2}\right)\cos\beta\right)\right) \tag{2.30}$$

where both the α- and β-curves are hyperhelical. The manifold vector of a β-curve is written as

$$\underline{\mathrm{a}}(\beta) = \exp\left(-j\pi\left(\underline{r}\left(\Theta+\frac{\pi}{2}\right)\cos\beta + \underline{v}\right)\right) \tag{2.31}$$

where $\underline{v}$ is defined as $\underline{v} \triangleq \underline{r}(\Theta)\cos\alpha$ and is constant over the β-curve. The rate of change of the arc length of a β-curve, $\dot{s}(\beta)$, following the

definition of Eq. 2.25 is

$$\dot{s}(\beta) = \|\dot{\underline{a}}(\beta)\| = \pi \left\| \underline{r} \left(\Theta + \frac{\pi}{2} \right) \right\| \sin \beta. \tag{2.32}$$

This is a straightforward manner to compute the length of a given array manifold β-curve. Given the *geodesic* nature of these curves [46], the measured distance on the β-curve presented here is the shortest distance on the array manifold. Thus, for any point P1 and P2, it is possible to rotate the Cartesian system by an angle Θ to select an appropriate β-curve that link P1 and P2. This way, Eq. 2.32 for $\dot{s}(\beta)$ can be utilised to have

$$\Delta s = \int_{\beta_1}^{\beta_2} \dot{s}(\beta) d\beta = \pi \left\| \underline{r} \left(\Theta + \frac{\pi}{2} \right) \right\| (\cos \beta_1 - \cos \beta_2). \tag{2.33}$$

This measure is sufficient to assess the distance between two vectors that are closely spaced, however, as the vectors move apart this measure fails since the shortest distance between them does not lie on the manifold any longer.

2.3 Inner Products on the Array Manifold

The measure of the inner product on the array manifold is difficult to characterise as a function of the differential geometry parameters. To get an idea of the motivations leading to this section, let us take the illustrative example where an antenna array receives two signals. In the N-dimensional complex space, they are represented by two distinct points on the array manifold. The system capability to process the two sources individually is necessarily function of the distance between the two points in the N-dimensional complex space $\|\underline{a}_2 - \underline{a}_1\|^2$, which is necessarily the same as $\underline{a}_1^H \underline{a}_2$.

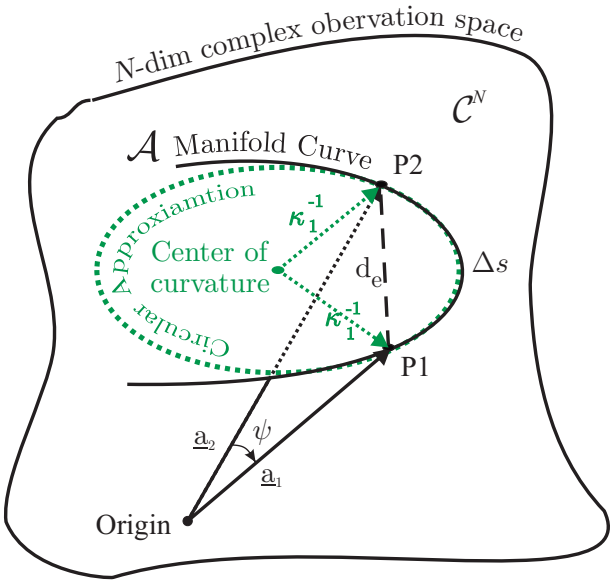


Figure 2.5: Two array manifold vectors and the circular approximation of the manifold curve joining their corresponding points.

In this section, we will describe how good measures of this product can be provided, noticably with the Geodesic distance, with the Euclidean distance and with the manifold radii. Geodesic and Euclidean distances are two standard metrics to describe the distances on a manifold.

2.3.1 Approximation with Geodesic and Euclidean Distances

Let us consider two antenna array manifold vectors $\underline{a}_1$ and $\underline{a}_2$, their corresponding points on the manifold P1 and P2, displayed on Fig. 2.5, and their separation angle ψ[3]. Simple geometry yields

$$\begin{aligned} \|\underline{a}_2 - \underline{a}_1\|^2 &= \|\underline{a}_1\|^2 + \|\underline{a}_2\|^2 - 2\,\|\underline{a}_1\|\,\|\underline{a}_2\|\cos\psi \\ &= 2N - 2\mathrm{Re}\{\underline{a}_1^H \underline{a}_2\}, \end{aligned} \tag{2.34}$$

[3]Please note that ψ is the angle between the two vectors and not the DOA separation

where ψ is the angle between the two manifold vectors. For the particular class of dense 3D-grid array, the inner product is strictly real and can hence be written as

$$\underline{\mathrm{a}}_1^H \underline{\mathrm{a}}_2 = N - \frac{1}{2} \left\| \underline{\mathrm{a}}_2 - \underline{\mathrm{a}}_1 \right\|^2 . \tag{2.35}$$

The norm $\|\underline{\mathrm{a}}_2 - \underline{\mathrm{a}}_1\|$ is the "straight" distance between P1 and P2, or, more formally, the *Euclidean distance* called $\mathrm{d_e}$ here. Let us now try to investigate the Euclidean distance. Table 2.1 displays the various available approximation of the inner product. Please note that the circular approximation is novel.

Table 2.1: Approximations of the inner product between two array manifold vectors

Approximation	Expression
1. Taylor Series Expansion	$N - \frac{1}{4}\Delta s^2 + \frac{1}{64}\Delta s^4$
2. Linear Approximation	$N - \frac{1}{2}\Delta s^2$
3. Circular Approximation	$N - \frac{2}{\kappa_1^2} \sin^2\left(\frac{\kappa_1 \Delta s}{2}\right)$

1. A Taylor-series expansions of the manifold vector at the order 2 at the midpoint s_0 (i.e. $s_0 = \frac{s_1+s_2}{2}$) have been used broadly in the array signal processing literature, e.g.

$$\underline{\mathrm{a}}_2 = \underline{\mathrm{a}}_0 + \underline{\mathrm{a}}_0' \frac{\Delta s_0}{2} + \underline{\mathrm{a}}_0'' \frac{\Delta s_0^2}{8} + \mathrm{o}\left(\Delta s^3\right) \tag{2.36}$$

$$\underline{\mathrm{a}}_1 = \underline{\mathrm{a}}_0 - \underline{\mathrm{a}}_0' \frac{\Delta s_0}{2} + \underline{\mathrm{a}}_0'' \frac{\Delta s_0^2}{8} + \mathrm{o}\left(\Delta s^3\right) . \tag{2.37}$$

2. In a majority of the literature on array processing, the angle ψ was often assumed small and the Euclidean distance was approximated with the Geodesic distance [46, Eq. 8.104] [49, Eq. 4.70]. With this approximation, the contribution of the principal curvature κ_1 is not completely included, because κ_1 plays a role in the higher derivative of the manifold, as described in

[9, Eq. (2.38)]. As displayed on Fig 2, the inner product $\underline{\mathrm{a}}_1^H \underline{\mathrm{a}}_2$ (that illustrates the angle between the two manifolds as well) can be linked to the distance between P1 and P2, using simple trigonometry: Let us assume that the manifold curve $\mathcal{A}$ is a straight line between P1 and P2, in this case, the Euclidean distance $\mathrm{d_e}$ can be approximated as being equal to the Riemannian distance Δs

$$\mathrm{d_e} \approx \Delta s \tag{2.38}$$

and hence

$$\underline{\mathrm{a}}_1^H \underline{\mathrm{a}}_2 \approx N - \frac{1}{2}\Delta s^2. \tag{2.39}$$

We call Eq. 2.39 the linear approximation of the inner product. This is a flawed approximation for several reasons.

3. We propose a novel and simple analytical description of the dot product. The local β-curve between P1 and P2 can be described as a circle of radius κ_1^{-1}. With this, the Euclidean distance is the length of the chord, as shown in Fig. 2.5.

2.3.2 Inner Product and Manifold Radii

As derived previously, the moving frame matrix $\mathbb{U}(s)$, along with the curvatures, gives a complete local description of an array manifold curve. With these, the orientation of the array manifold curve at a particular instant can be assessed with the concept of *manifold radii*.

Definition 3 (Manifold Radii Vector)**.** *The manifold radii vector is the dot product between the array manifold vector and the coordinate*

matrix at a point s of a p-curve:

$$\begin{aligned}\underline{\mathcal{R}}(s) &= \mathbb{U}^H(s)\underline{\mathrm{a}}(s) \\ &= \left[\underline{u}_1^H(s)\underline{\mathrm{a}}(s), \underline{u}_2^H(s)\underline{\mathrm{a}}(s), \ldots, \underline{u}_N^H(s)\underline{\mathrm{a}}(s)\right]. \end{aligned} \tag{2.40}$$

An observation of Eq. 2.18 leads to the interesting conclusion that, when the coordinate vector derivative $\underline{u}_k'(s)$ is not linearly dependent of $\underline{u}_k$ (i.e. $\underline{u}_k'^H\underline{u}_k = 0$), the definitions of the Cartan matrix and manifold radii vector simplify to the one made earlier in [46]. This occurs when the antenna array employed is fully symmetrical. The Manifold Radii vector can now be utilised to define a new distance measure on the array manifold.

Lemma 4 (Inner Product on an Array Manifold Curve)**.** *The Inner product between two array manifold vectors of the same hyperhelical array manifold curve can be written as*

$$\begin{aligned}\underline{\mathrm{a}}^H(s)\underline{\mathrm{a}}(s+\Delta s) &= \underline{\mathcal{R}}^H(s) \\ &\quad \times \mathrm{expm}\{s\mathbb{C}(s) - (s+\Delta s)\mathbb{C}(s+\Delta s)\}\underline{\mathcal{R}}(s+\Delta s). \end{aligned} \tag{2.41}$$

Proof. Given the definition of manifold radii, the inner product of two array manifold vectors on a particular manifold p-curve can be written as

$$\begin{aligned}\underline{\mathrm{a}}^H(s)\underline{\mathrm{a}}(s+\Delta s) &= \underline{\mathcal{R}}^H(s)\mathrm{expm}\{s\mathbb{C}(s)\}\mathbb{U}(0) \\ &\quad \times \mathbb{U}^H(0)\mathrm{expm}\{(s+\Delta s)\mathbb{C}^H(s+\Delta s)\}\underline{\mathcal{R}}(s+\Delta s). \end{aligned} \tag{2.42}$$

Utilising the orthonormal nature of $\mathbb{U}(s)$ and the skew-symmetricity of $\mathbb{C}(s)$, Eq. 2.42 yields Eq. 2.41. □

This highlights that, on an array manifold p-curve, the inner product depends on the number of antennas N, the Riemannian distance

between the two vectors Δs and the $N-1$ curve's curvatures of the Cartan matrix $\mathbb{C}(s)$. Please note that, for the sake of notation simplicity, we will denote the "metric matrix"of the quadratic form of 2.41 as

$$\mathbb{M}_{s_1,s_2} = \text{expm}\{s_1\mathbb{C}(s_1) - s_2\mathbb{C}(s_2)\}. \tag{2.43}$$

2.3.3 Inner Product on the α and β-Curves

On hyperhelical curves, due to the tractability of the curvatures, the manifold radii and Cartan matrix become constant over the whole curve, and the inner product is

Lemma 5 (Inner Product on an Hyperhelical Array Manifold Curve)**.** *The Inner product between two array manifold vectors of the same hyperhelical array manifold curve is written as*

$$\underline{\mathrm{a}}^H(s)\underline{\mathrm{a}}(s+\Delta s) = \underline{\mathcal{R}}^H\text{expm}\{-\Delta s\mathbb{C}\}\underline{\mathcal{R}}. \tag{2.44}$$

This illustrates that, on an hyperhelical curve, the inner product is independent of the parameter s, and depends on the curvatures and the distance between the array manifold vectors only. This makes a more straightforward characterisation of the inner product possible. The array manifold having a constant norm of $\|\underline{\mathrm{a}}\| = \sqrt{N}$, the inner product is upper-bounded and lower-bounded by N and $-N$, respectively.

Proof. Given the definition of manifold radii, the inner product of two array manifold vectors on one hyperhelical manifold curve can be written as

$$\underline{\mathrm{a}}^H(s)\underline{\mathrm{a}}(s+\Delta s) = \underline{\mathcal{R}}^H\text{expm}\{s\mathbb{C}\}\mathbb{U}(0)\mathbb{U}^H(0)\text{expm}\{(s+\Delta s)\mathbb{C}^H\}\underline{\mathcal{R}}. \tag{2.45}$$

Following the orthonormal nature of $\mathbb{U}(s)$ and the skew-symmetricity of $\mathbb{C}$, Eq. 2.45, is

$$\underline{\mathrm{a}}^H(s)\underline{\mathrm{a}}(s+\Delta s) = \underline{\mathcal{R}}^H \mathrm{expm}\{-\Delta s\mathbb{C}\}\underline{\mathcal{R}}. \tag{2.46}$$

This forms the proof of the theorem. □

This important result can be simplified with a very good approximation, that is

$$\underline{\mathrm{a}}^H(s)\underline{\mathrm{a}}(s+\Delta s) = N - \Delta s\underline{\mathcal{R}}^H\mathbb{C}\underline{\mathcal{R}}. \tag{2.47}$$

Indeed, the terms of the Taylor series expansion of Eq. 2.46 are of a quadratic form and are upper bounded by λ_0, the largest eigenvalue of $\mathbb{C}$. At the k-th order, the residual error is

$$\left|\underline{\mathcal{R}}^H \mathrm{expm}\{-\Delta s\mathbb{C}\}\underline{\mathcal{R}} - \sum_{k=0}^{K} \underline{\mathcal{R}}^H \frac{(-\Delta s\mathbb{C})^k}{k!}\underline{\mathcal{R}}\right| \leq N \sum_{k=K+1}^{\infty} \frac{(-\Delta s\lambda_0)^k}{k!}. \tag{2.48}$$

The Taylor series expansion can be made by the first two terms of 2.48, i.e.,

$$\underline{\mathrm{a}}^H(s)\underline{\mathrm{a}}(s+\Delta s) = \underline{\mathcal{R}}^H \left((\mathbb{I}_d - \Delta s\mathbb{C}) + \mathrm{o}(\Delta s^2\mathbb{C}^2)\right)\underline{\mathcal{R}}. \tag{2.49}$$

Thus, the error made while doing this approximation decreases exponentially. It can be observed, following the new expression of 2.47, that the term $\Delta s\underline{\mathcal{R}}^H\mathbb{C}\underline{\mathcal{R}}$ is always positive, because the inner product is always smaller than N.

2.4 Summary

This chapter introduced the framework of array manifold and the most important differential geometry parameters that serve the characterisation of an array manifold curve. Along with that, a study of the different tools available to ascertain the inner products between two array manifold vectors was presented. The framework that provides the link between the inner product and the array manifold vectors curve parameter was presented, for hyperhelical and non-hyperhelical curves.

Chapter 3

Importance of the Antenna Arrays Geometries

This chapter presents a novel study of the impact of the antenna array geometry on the worst case scenario when two sources are closely spaced in the angular domain[1]. This case is particularly worth investigating because this is the scenario where the role of the antenna array geometry is exacerbated. This is highly relevant and timely for future 5G networks where a dramatical increase in user density is expected. The array geometry is reflected through the array manifold mathematical object and the derivations introduced in Chapter 2. Based on that, it was demonstrated that the antenna arrays that have the largest number of antenna elements do not necessarily perform the best. This is the stepping stone towards designs optimising the array geometry while keeping the number of antennas reasonable.

[1]Please note that part of the content of this chapter was presented at the Global Conference on Communications 2015 (GlobeCom2015) in San Diego, CA, USA [3].

3.1 Introduction

The next generation of wireless communication systems is expected to employ antenna arrays, called large or massive antenna arrays, that contain hundreds or thousands of antenna array elements. Such wireless systems are called massive MIMO or MaMI. The signals from all these array elements are processed and combined simultaneously, providing, for instance, high resolution and cochannel interference cancellation [50]. The literature contains lots of contributions on this trend [51]. However, utilising an independent RF chain for each antenna element of a large array is not sustainable with the given constraints of power, manufacturing cost and available area (array aperture). Some methods in the literature propose a rollback to analogue or hybrid beamforming [52, 53] as a method to function with a lower number of RF chains at the cost of reduced beamforming performance and accuracy.

In the literature, most of the array design techniques have been geared towards optimising the array geometries to achieve the desired performance criterion. Some performance criteria examples are maintaining a uniform parameter estimation performance across the whole field-of-view [54], resolving ambiguities [55], providing increased coverage [56], reducing sidelobe level [57], improving direction finding capabilities [58] and designing linear arrays (non-uniform or uniform) and planar arrays with predefined detection–resolution thresholds [59].

Typical studies assume multiple users to be randomly distributed in space. However, the worst case scenario is when the interfering users are located close to the desired user in space. This is the

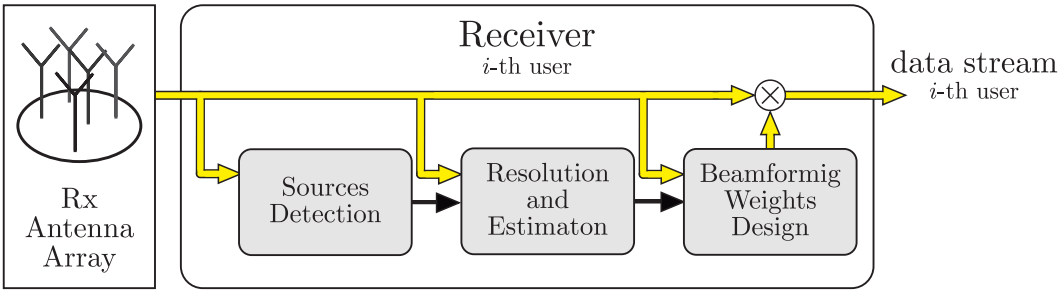


Figure 3.1: The tasks of a receiver utilising an antenna array.

scenario that stresses the system the most and when the array geometry takes the most importance. This is the scenario that is considered/studied in this chapter. Towards this, we present a novel study of the impact of the antenna array geometry on the wireless communication system tasks performed by antenna arrays. Particularly, we present a task-oriented analysis of the antenna array performance. It is well known that the presence of interfering users affects the performance of detecting, resolving and receiving the desired signal and that the worst case scenario is dictated by the user who is located closest to the desired user and this forms the motivation of analysing the scenario of two closely spaced users interfering with each other. The remainder of this Chapter is organised as follows. In Section 3.2, the impact of the antenna array geometry on preliminary tasks of wireless communications is assessed. In Section 3.3, the impact of the antenna array geometry on beamforming is investigated. Finally, the Chapter is summarised in Section 3.4

3.2 Preliminary Tasks of Wireless Communication Systems

Consider a calibrated antenna array system consisting of N antennas operating in the presence of a desired source and several interferers. Figure 3.1 displays the sequential tasks of the multiple-antenna wireless receiver that are detection, resolution & estimation, and reception with beamforming. Over a particular observation interval, during which the channel remains constant, the receiver collects L snapshots and constructs the best possible estimate of the signal subspace. The limited number of snapshots and the presence of channel noise create uncertainty in the N-dimensional complex space on the location of the sources. The uncertainties around the array manifold vectors of each source are represented by an *uncertainty sphere* [46] of radius σ_{e_i} (uncertainty sphere on the i-source)

$$\sigma_{e_i} = \sqrt{\frac{1}{2(\mathrm{SNR} \times L)}}. \tag{3.1}$$

It is straightforward to see from Eq. 3.1 that this sphere shrinks with a growing number of snapshots and a reducing noise level. The N-dimensional observation spaced hence contains two uncertainty spheres around the array manifold vectors.

The primordial task that a receiver has to achieve is the detection task, as displayed in Fig. 3.1. The detection capability of a particular array system is the ability to estimate the number of sources contributing to the received signal [46]. According to [60], two sources can be detected if and only if the uncertainty spheres do not make contact.

Based on Chapter 8 of [61] and with reference to Fig. 3.2, it can

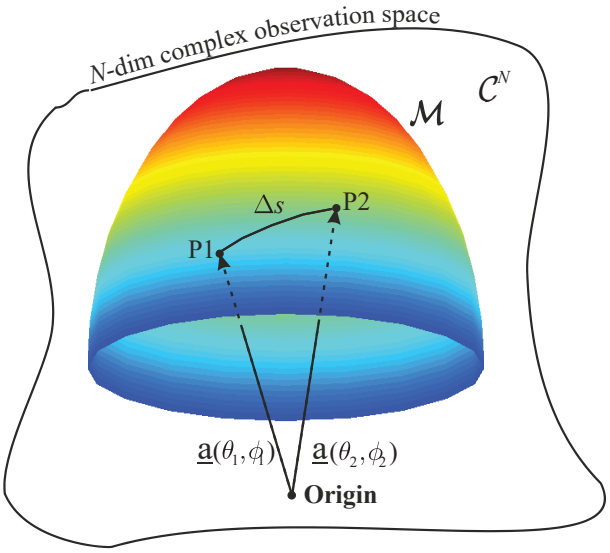


Figure 3.2: Illustration of the manifold surface $\mathcal{M}$, the manifold vectors $\underline{\mathrm{a}}\,(\theta_1, \phi_1)$ and $\underline{\mathrm{a}}\,(\theta_2, \phi_2)$ and the arc length Δs of a geodesic curve between two points P1 and P2 on $\mathcal{M}$.

be shown that for two points P1 and P2 on the manifold surface $\mathcal{M}$ the minimum $(\mathrm{SNR}\times L)_{\mathrm{det}}$ for the system to detect two users located close to each other in space (i.e. $\Delta\theta$ and $\Delta\phi$ are small) is given by

$$(\mathrm{SNR}\times L)_{\mathrm{det}} = \frac{2}{\Delta s^2}. \tag{3.2}$$

Figure 3.3 illustrates the probability of detection versus varying SNR for two users with a fixed separation of 0.5 degrees along the azimuth and elevation ($\Delta\theta = \Delta\phi = 0.5^{\mathrm{o}}$) and with $L = 200$ snapshots across different grid geometries. In this trial, the Akaike Information Criterion (AIC) [62] detection algorithm has been employed and a particular detection iteration is considered successful when the algorithm returns two users instead of one. The results indicate that the best geometry is the "filled"-grid array while the circular array achieves the worst performance. To get clearer insights into that, Figures 3.4 and 3.5 illustrate the detection threshold presented in Eq. 3.2 for the five grid array geometries under consideration. The mid eleva-

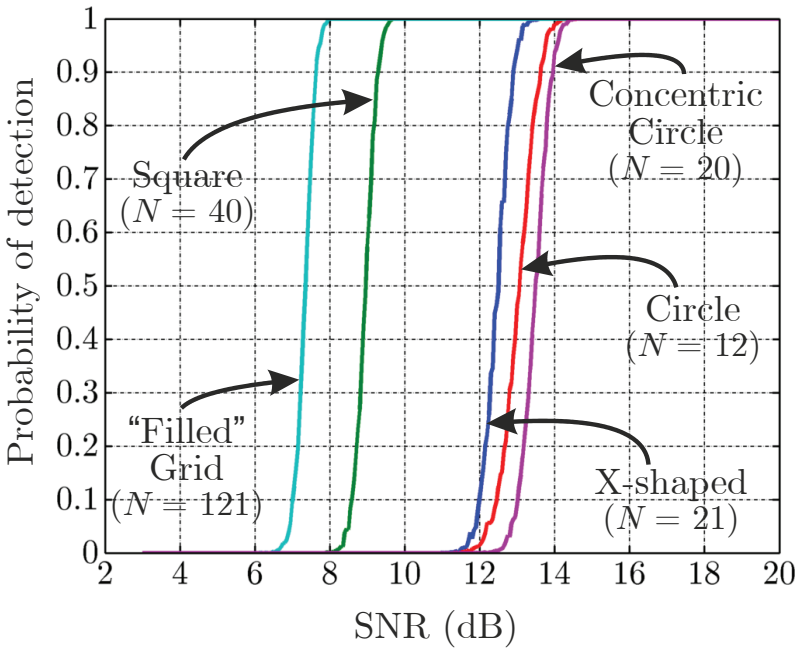


Figure 3.3: Comparison of the probabilities of detection versus input SNR for the grid array geometries under evaluation (1000 iterations).

tion angle $\phi_0 = (\phi_1 + \phi_2)/2$ is varied while $\theta_0 = (\theta_1 + \theta_2)/2$ remains constant at 90°. In Fig. 3.4, $\Delta\theta = \Delta\phi = 0.5°$, while in Fig. 3.5, $\Delta\theta = 0.5°$ and $\Delta\phi = 1°$. As derived earlier, the detection threshold displays a dependence on elevation when $\Delta\theta \neq \Delta\phi$. Please note that the simulation results with respect to varying azimuth are not exhibited as the performance is constant with azimuth at all times as predicted by Eq. 3.2.

Table 3.1: Performance ranking of antenna array geometries for the task of detection

Performance Order	Geometry
1st	"Filled"-Grid
2nd	Square
3rd	X-Shaped
4th	Concentric Circle
5th	Circle

As reported by Table 3.1, the "filled"-grid array followed by the

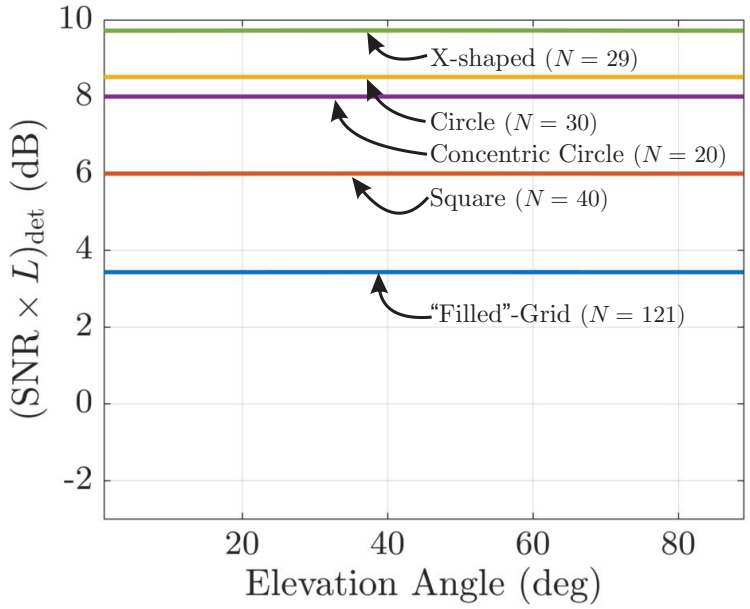


Figure 3.4: Detection threshold in terms of $(\text{SNR}\times L)_{\text{det}}$ versus varying elevation angle for the grid array geometries under evaluation when $\Delta\theta = \Delta\phi = 0.5°$ ($\theta_0 = 90°$)

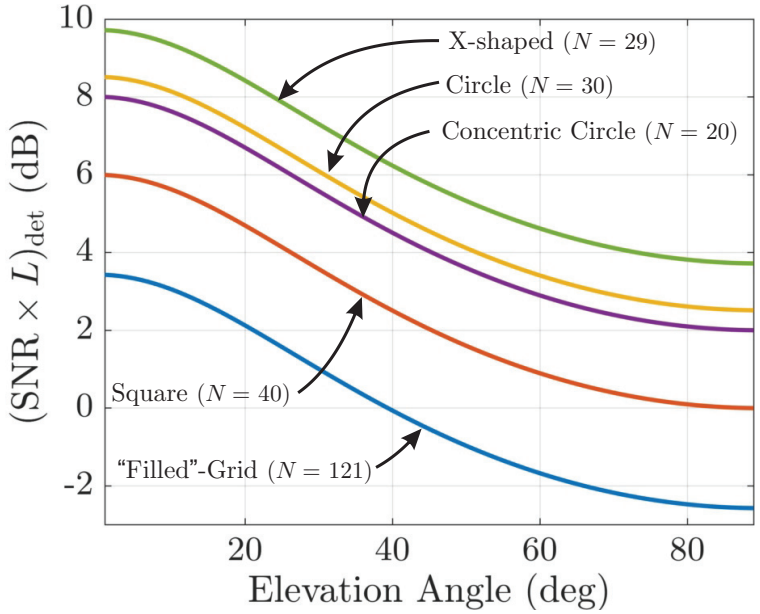


Figure 3.5: Detection threshold in terms of $(\text{SNR}\times L)_{\text{det}}$ versus varying elevation angle for the grid array geometries under evaluation when $\Delta\theta = 0.5°$ and $\Delta\phi = 1°$ ($\theta_0 = 90°$).

square array provides the best performance while the circular and concentric circular arrays perform the worst. One can observe that the number of antennas is the crucial factor that determines the detection threshold. However, the result shows that the square array yields an acceptable detection threshold for a much lower number of antennas than the "filled"-grid array. This is due to the fact that $(\mathrm{SNR}\times L)_{\mathrm{det}}$ is determined by $\|\underline{r}_x\|$ (remember $\|\underline{r}_x\| = \|\underline{r}_y\|$ for all grid arrays) rather than the number of antennas N itself. This implies that by optimising the placement and inter-antenna spacing, for the same number of antennas N, a lower detection threshold may be obtained. Hence, among the geometries considered, for a massive MIMO array communication system, a square geometry for detection would suffice to keep the system energy efficient. On the other hand, for applications requiring extremely precise target detection such as RADAR, one may use the "filled"-grid array at the start and track with the square array subsequently.

Successful detection does not imply that the two sources may be resolved. The resolution capability is the ability to perceive two distinct spectral peaks/nulls.

Figure 3.6 illustrates this idea by presenting the performance of the MUSIC direction finding algorithm for the circular, square and "filled"-grid geometries. For the same $(\mathrm{SNR} \times L)$, the circular array almost fails to resolve the two sources whereas the square and the "filled"-grid array do so. This forms the motivation of this section in utilising the resolution threshold to select the appropriate geometry for this task.

The resolution threshold with respect to points P1 and P2 in

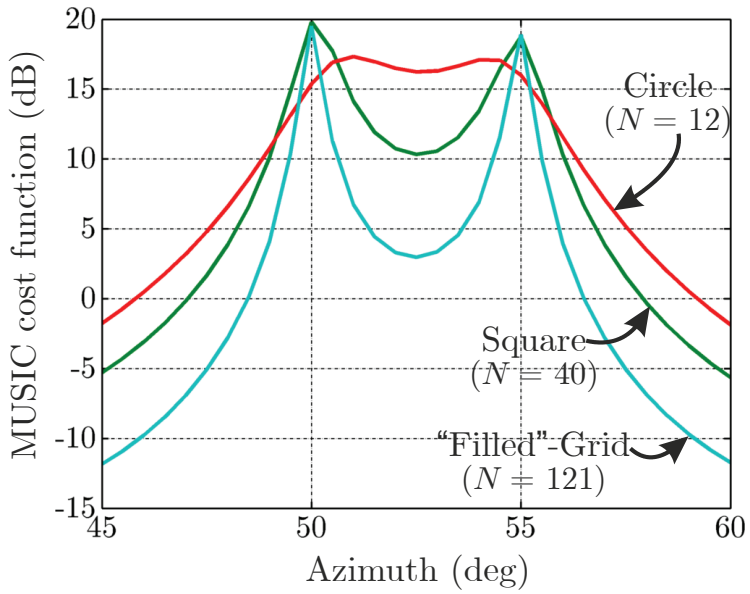


Figure 3.6: Illustration of MUSIC cost function versus azimuth for the filled square, square and circular array geometries for a scenario of 2 equipowered users located at (50°, 30°) and (55°, 30°) (SNR $= -1dB$, $L = 200$).

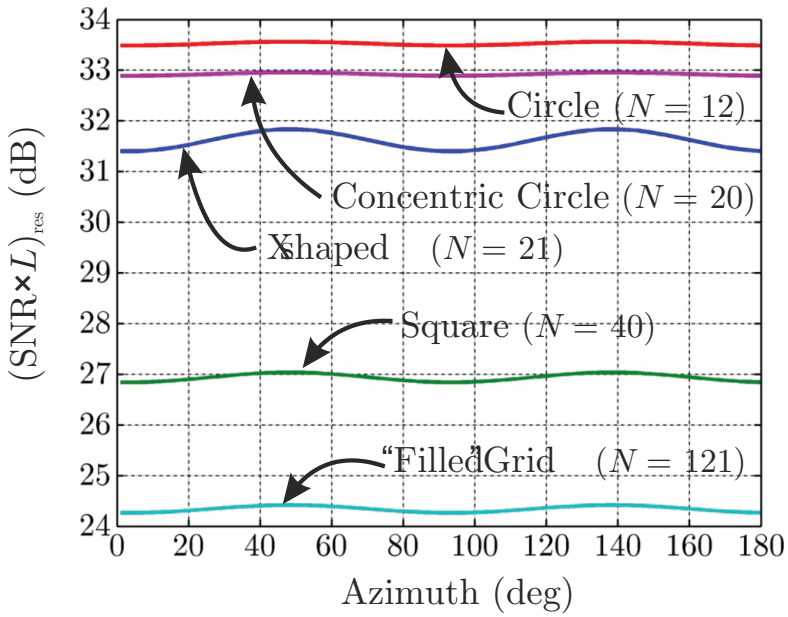


Figure 3.7: Resolution threshold in terms of $(\mathrm{SNR}\times L)_{\mathrm{res}}$ versus varying azimuth angle for the array geometries under evaluation ($\phi_0 = 40^o$).

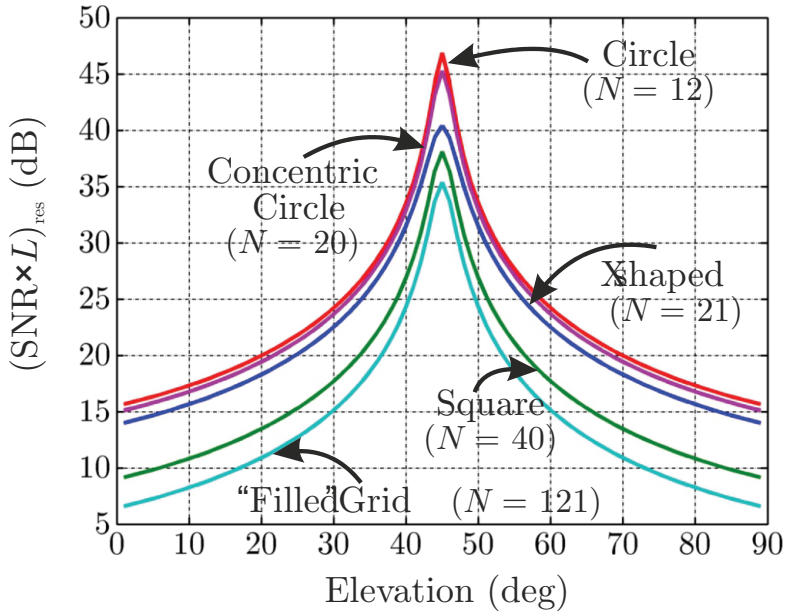


Figure 3.8: Resolution threshold in terms of $(\mathrm{SNR}\times L)_{\mathrm{res}}$ versus varying elevation angle for the array geometries under evaluation ($\theta_0 = 80^o$).

Fig. 3.2 provides a minimum $(\mathrm{SNR}\times L)_{\mathrm{res}}$ for the system to resolve the two sources,

$$(\mathrm{SNR}\times L)_{\mathrm{res}} = \frac{32}{\Delta s^4 \left(\kappa_1^2 - \mathrm{sum}^2\left(\widetilde{\underline{R}}^3\left(\Theta + \frac{\pi}{2}\right)\right) - \frac{1}{N}\right)}. \tag{3.3}$$

Equation 3.3 indicates that, unlike detection, $(\mathrm{SNR}\times L)_{\mathrm{res}}$ depends on both azimuth and elevation since a different curve yielding a different curvature κ_1 will be chosen for every pair $(\underline{\mathrm{a}}_1, \underline{\mathrm{a}}_2)$.

Figures 3.7 and 3.8 present the resolution threshold for varying azimuth and elevation angles (θ_0, ϕ_0) respectively. A separation angle of $\Delta\theta = \Delta\phi = 0.5^{\mathrm{o}}$ has been utilized. The performance grading of the array geometries is similar to that of detection, i.e. the "filled"-grid array performs the best while the circular array performs the worst. We can conclude that the number of antennas has the largest impact on the performance on the tasks of detection and resolution.

3.3 Beamforming Performance with Antenna Arrays

Beamforming is creating a beam towards a particular direction of interest by applying a set of complex weights on the antenna. This way, the spatial dimension is used to maximise the gain of the antenna array towards the source and minimise it towards interference. For more discussions about beamforming itself, please refer to Section 5.3. The impact of the antenna array geometry on the beamforming performance forms the scope of this section[2].

3.3.1 Steering Vector Beamformer

To study this, let us consider a simpler case of the received signal vector $\underline{x}(t)$ presented in Section 1.2 where the environment is composed of only a desired-source and one interference, and one multipath per user. In this case, the received signal vector is

$$\underline{x}(t) = \underline{\mathrm{a}}_1 m_1(t) + \underline{\mathrm{a}}_2 m_2(t) + \underline{\mathrm{n}}(t) \tag{3.4}$$

with $m_1(t)$ and $m_2(t)$ denoting the message signals of the two users with powers P_1 and P_2 respectively and $\underline{\mathrm{n}}(t)$ is the white Gaussian noise of zero mean and covariance $\mathbb{R}_{\mathrm{n}} = \sigma_{\mathrm{n}}^2 \mathbb{I}_N$. Hence, the covariance matrix $\mathbb{R}_{xx}$ can be constructed to obtain the second order statistics of $\underline{x}(t)$ as

$$\mathbb{R}_{xx} = \mathcal{E}\left\{\underline{x}(t)\,\underline{x}(t)^H\right\} = \overbrace{P_1 \underline{\mathrm{a}}_1 \underline{\mathrm{a}}_1^H}^{\mathbb{R}_{\text{desired}}} + \overbrace{P_2 \underline{\mathrm{a}}_2 \underline{\mathrm{a}}_2^H + 2\mathrm{Re}\left\{\rho_{12} \underline{\mathrm{a}}_1 \underline{\mathrm{a}}_2^H\right\}}^{\mathbb{R}_{\text{undesired}}} + \overbrace{\sigma_{\mathrm{n}}^2 \mathbb{I}_{\mathrm{n}}}^{\mathbb{R}_{\mathrm{n}}},$$

where $\mathbb{R}_{\text{desired}}$ is the covariance matrix of user 1 and $\mathbb{R}_{\text{undesired}}$ contains the covariance matrices of user 2 and the term arising from

[2]Please note that the steering vector beamformer is also known as "matched beamformer" and that the subspace beamformer is also known as "null beamformer".

ρ, the cross-correlation coefficient of the messages transmitted by users 1 and 2. Also, $\mathbb{R}_{\mathrm{n}}$ is the noise covariance matrix. To receive the message of user 1, one can steer a beam towards (θ_1, ϕ_1) by employing the manifold vector $\underline{\mathrm{a}}_1$ as a weight vector $\underline{w}$ (this is called a steering vector). For the moment, we employ the steering vector beamformer in order to isolate the effect of the array geometry alone on handling interference. Without any loss of generality, it has been assumed that $\rho_{12} = 0$, implying that the messages transmitted by users 1 and 2 are uncorrelated. In this case, the beamformer performance to mitigate interference can be characterised by the signal-to-noise plus interference ratio at its output, $\mathrm{SNIR}_{\mathrm{out}}$, as

$$\begin{aligned}\mathrm{SNIR}_{\mathrm{out}} &= \frac{\underline{w}^H \mathbb{R}_1 \underline{w}}{\underline{w}^H \left(\mathbb{R}_2 + \mathbb{R}_{\mathrm{n}}\right) \underline{w}} \\ &= \frac{P_1 \underline{\mathrm{a}}_1^H \underline{\mathrm{a}}_1 \underline{\mathrm{a}}_1^H \underline{\mathrm{a}}_1}{P_2 \underline{\mathrm{a}}_1^H \underline{\mathrm{a}}_2 \underline{\mathrm{a}}_2^H \underline{\mathrm{a}}_1 + \sigma_{\mathrm{n}}^2 \underline{\mathrm{a}}_1^H \underline{\mathrm{a}}_1} \\ &= \frac{N^2 P_1}{P_2 \left|\underline{\mathrm{a}}_1^H \underline{\mathrm{a}}_2\right|^2 + \sigma_{\mathrm{n}}^2 N}. \end{aligned} \tag{3.5}$$

As we are dealing with a case that presents only two users, and hence two points on the manifold, it is straightforward to find a β-curve (hyperhelix) to join P1 and P2. Hence, Equation 3.5, in conjunction with Eq. 2.46, provides

$$\boxed{\mathrm{SNIR}_{\mathrm{out}} = \frac{N^2 P_1}{P_2 \left|\underline{\mathcal{R}}^H \mathrm{expm}\{-\Delta s \mathbb{C}\} \underline{\mathcal{R}}\right|^2 + \sigma_{\mathrm{n}}^2 N}}. \tag{3.6}$$

Equation 3.6 reveals a trade-off between the product $\underline{\mathcal{R}}^H \mathrm{expm}\{-\Delta s \mathbb{C}\} \underline{\mathcal{R}}$ that contains the characterisation of the shape of the array manifold curve[3] and the number of antennas N. Hence, different geometries

[3]Let us recall that the manifold radii $\underline{\mathcal{R}}$ and Cartan matrix $\mathbb{C}$ depend only on the curvatures, hence the product $\underline{\mathcal{R}}^H \exp\{\Delta s \mathbb{C}\} \underline{\mathcal{R}}$ is a function of the curvatures and the arclength Δs only

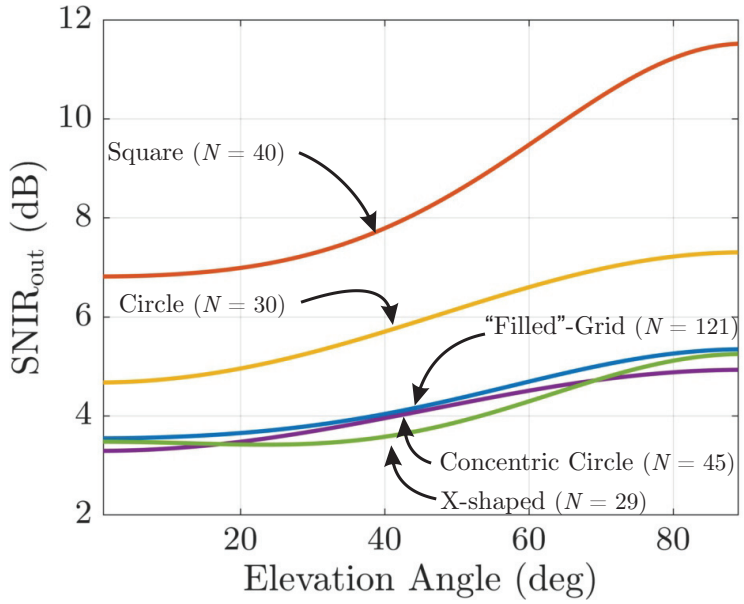


Figure 3.9: Steering vector beamformer performance for the array geometries shown in Fig. 2.3.a. The $\text{SNIR}_{\text{out,ste}}$ (dB) versus azimuth angle for the array geometries under evaluation ($\phi_0 = 50^o$) is presented.

present different performance depending on their curvatures, the arc length and the number of antennas N. There exists a trade-off between the number of antennas and the antenna array geometry.

To illustrate this conclusion, we present in Figs. 3.9 and 3.10, the evaluation of the SNIR for the five geometries of Fig. 2.3a with varying elevation and constant azimuth $\theta = 90^o$ (Fig. 3.9), and varying azimuth for constant elevation $\phi = 50^o$ (Fig. 3.10). Please note that the angular separation between the sources was $\Delta\theta = 5^o$ and $\Delta\phi = 6^o$ and the input SNR was chosen to be 20dB with $P_1 = P_2 = 1$. Across all geometries, as shown in Figs. 3.9 and 3.10, the square antenna array exhibits the best performance with a maximum SNIR_{out} of 11.5 dB achieved at $\tilde{\theta} = 50^o$ and $\tilde{\phi} = 90^o$. The square, circular and X-shaped antenna arrays surprisingly outperform the "filled"-grid array which possesses the highest number of antenna elements. This is in-

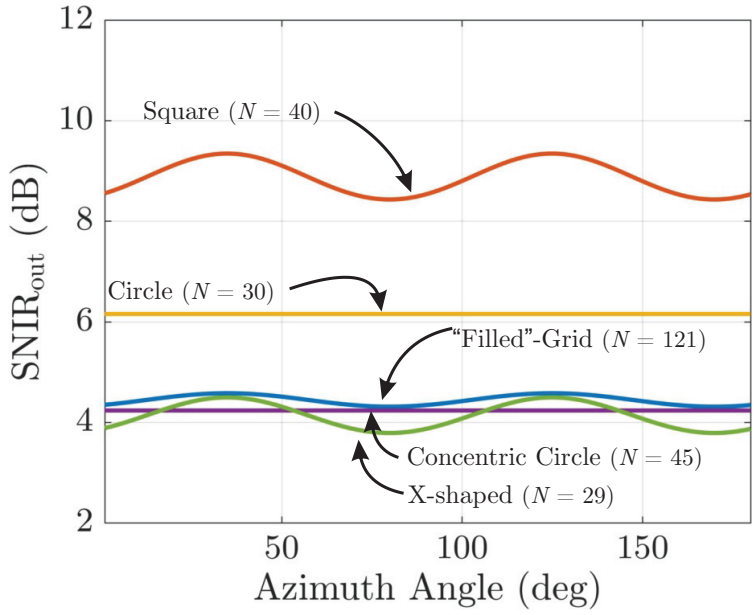


Figure 3.10: Steering vector beamformer performance for the array geometries shown in Fig. 2.3.a. The SNIR_{out} (dB) versus elevation angle for the array geometries under evaluation ($\theta_0 = 90^o$. In both cases, the angular separation between the sources was $\Delta\theta = 5^{\text{o}}\Delta\phi = 6^{\text{o}}$) and the input SNR was chosen to be 20dB with $P_1 = P_2 = 1$ is presented.

line with the result that the "filled"-grid array has a poor ratio of $\underline{\mathcal{R}}^H \text{expm}\{-\Delta s\mathbb{C}\}\underline{\mathcal{R}}/N$ while the square array yields the highest ratio closely followed by the circular array. A higher ratio of this key term implies higher capacity according to Eq. 3.6.

3.3.2 Null Beamformer

In this subsection, the performance of the array geometries when the beamformer employed is a subspace beamformer are assessed. This beamformer algorithm projects the received signal on the subspace that is perpendicular to array manifold vector of the second user $\underline{\text{a}}_2$ and hence cancels the interferer completely,

$$\underline{w}_{\text{sub}} = \mathbb{P}^{\perp}_{\underline{\text{a}}_2}\underline{\text{a}}_1. \tag{3.7}$$

For more details about this beamformer, please refer to Section 5.3. The performance of this receiver in terms of $\mathrm{SNIR}_{\mathrm{out,sub}}$, is

$$\begin{aligned}\mathrm{SNIR}_{\mathrm{out,sub}} &= \frac{\underline{w}_{\mathrm{sub}}^H \underline{\mathrm{a}}_1 \underline{\mathrm{a}}_1^H \underline{w}_{\mathrm{sub}}}{\underline{w}_{\mathrm{sub}}^H \left(\underline{\mathrm{a}}_2 \underline{\mathrm{a}}_2^H + \sigma_{\mathrm{n}}^2 \mathbb{I}_N\right) \underline{w}_{\mathrm{sub}}} \\ &= \frac{\underline{w}_{\mathrm{sub}}^H \underline{\mathrm{a}}_1 \underline{\mathrm{a}}_1^H \underline{w}_{\mathrm{sub}}}{\sigma_{\mathrm{n}}^2 \underline{w}_{\mathrm{sub}}^H \underline{w}_{\mathrm{sub}}},\end{aligned} \tag{3.8}$$

because the signal received from interfering user is cancelled completely. With the beamforming design of Eq. 3.7, the $\mathrm{SNIR}_{\mathrm{out,sub}}$ can be derived as

$$\mathrm{SNIR}_{\mathrm{out,sub}} = N\mathrm{SNR}\left(1 - \left(\frac{\underline{\mathrm{a}}_1^H \underline{\mathrm{a}}_2}{N}\right)^2\right)^2 \tag{3.9}$$

and, with Theorem 5, we have

$$\boxed{\mathrm{SNIR}_{\mathrm{out,sub}} = N\mathrm{SNR}\left(1 - \left(\frac{\underline{\mathcal{R}}^H \mathrm{expm}\{-\Delta s \mathbb{C}\}\underline{\mathcal{R}}}{N}\right)^2\right)^2}. \tag{3.10}$$

Equation 3.10 reveals an interplay between the term $\mathrm{SNR} \times L$ and the contribution from the geometry $\underline{\mathcal{R}}^H \mathrm{expm}\{-\Delta s \mathbb{C}\}\underline{\mathcal{R}}/N$. When the angular separation between the two sources is large enough, the contribution of the geometry is negligible and the number of antenna determine the performance. To illustrate this, Figure 3.11 presents the evaluation of the performance of the geometries from Fig. 2.3.a. Indeed, the geometry with the largest number of antenna elements is performing the best. Please note that, compared with the steering vector beamformer, with the subspace beamformer the contribution of the geometry decreases sharply because of the presence of the square terms in Eq. 3.10.

Figure 3.12 presents a comparison of the $\mathrm{SNIR}_{\mathrm{out,sub}}$ achieved by the two beamformers, for varying separation between the users. This

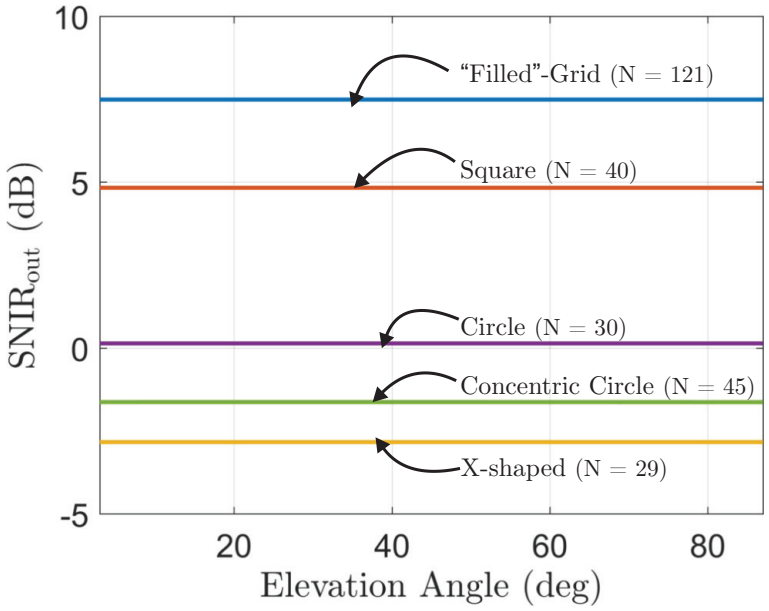


Figure 3.11: Subspace vector beamformer performance for the array geometries shown in Fig. 2.3.a. The SNIR_{out} (dB) versus elevation angle for the array geometries under evaluation ($\theta_0 = 90^o$. The angular separation between the sources was $\Delta\theta = 0.1^{\text{o}}$ and $\Delta\phi = 0.1^{\text{o}}$) and the input SNR was chosen to be 20dB.

is a simple evaluation of Eqs. 3.10 and 3.6. Understandably, the beamsteering achieves maximum interference mitigation only when the manifold vectors of the users are orthogonal, which is rarely the case. At this exact separation angle, the beamsteering weight vector belongs to the subspace spanned by the projection operator of the subspace beamformer. For more information about this, please consider reading more about characteristic points in [46]. On the other hand, the subspace beamformer achieves maximum $\text{SNIR}_{\text{out,sub}}$ quickly while the interferer is moved away from the desired user. When the interferer is close, the $\text{SNIR}_{\text{out,sub}}$ is reduced because the projection operator reduces the power of the desired user (SNR). As displayed with Eq. 3.10, this phenomenon is induced by the term $\left(\underline{\mathcal{R}}^H \text{expm}\{-\Delta s\mathbb{C}\}\underline{\mathcal{R}}/N\right)^2$, that decreases with a magnitude squared, this is the zone that is between 0 and 5° in Fig. 3.12. We can observe

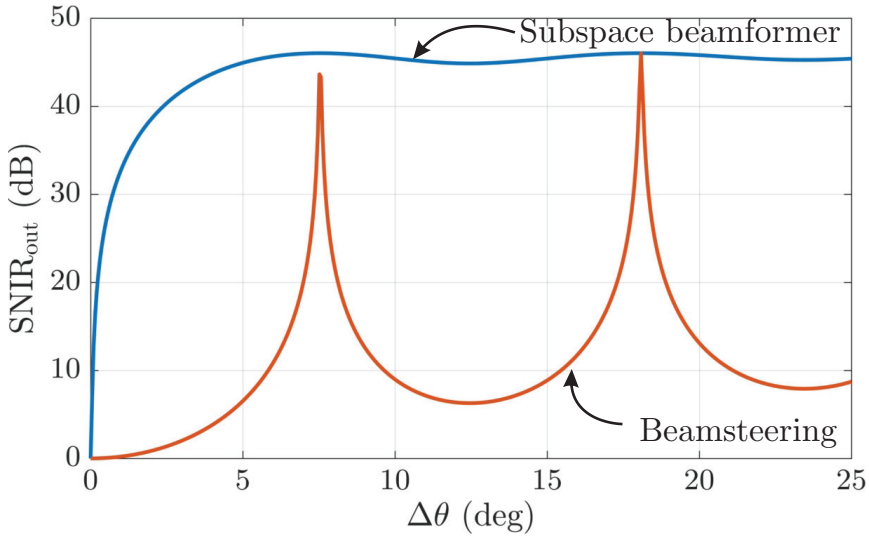


Figure 3.12: Comparison between the steering vector beamformer and the subspace-based beamformer for the Square array geometry of Fig. 2.3.a. The SNR was set to 20 dB and both users were equipowered.

that, past this separation, that is 5° here, the $\text{SNIR}_{\text{out,sub}}$ of Eq. 3.10 is NSNR and hence the geometry doesn't impact the performance anymore.

3.4 Summary

This chapter was concerned with illustrating the importance of antenna array geometry for a variety of wireless communication tasks. This was achieved by employing relevant performance criteria as figures-of-merit. It was deduced that the detection and resolution thresholds have strong dependencies with the number of antennas because it conditions the number of dimensions. On the reception part, new simulation studies, supported by theoretical results, demonstrated that the SNIR_{out} does not depend solely on the number of antennas, but also strongly on the array geometry. Thus, the square array of 40 antennas, for instance, has higher SNIR_{out} and better energy efficiency than a "filled"-grid array with more ($N = 121$) antennas.

Chapter 4

Channel Capacity Loss

In this chapter the "channel capacity loss" metric is introduced to fully characterise the presence of co-channel interference in a general multi-user multipath MIMO channel[1]. The newly introduced metric is linked with the shape of the array manifold introduced in the previous chapter, and the impact of the antenna array geometry onto the system performance is investigated[2].

4.1 Introduction

An important amount of research has been done to investigate the impact of various factors on the channel capacity. For example, [63] and [64], based on non-parametric models, studied the impact of interference, indoor line-of-sight (LOS) and high antenna correlation. In [65], the impact of non-ideal hardware was considered and modelled. In [66], the transmitted signalling was optimised to maximise the capacity. In [67], using a non-parametric channel model for an in-

[1] This research was presented at IEEE International Conference on Communications 2017 [1].

[2] Please note that the present chapter focuses on the influence of the antenna array geometry on the conditioning of the signal received, whereas chapter 3 was concerned with the impact of the antenna array geometry on the subsequent communication tasks.

door environment, the effect of multipath propagation on the channel capacity is studied. In [68], the impact of four uniform array geometries on the ergodic capacity in a microcellular urban environment was studied, albeit in the single-user case. In [69, 70], an analysis of the achievable capacity for two different sets of array geometries was pursued assuming the users are located uniformly within a sphere of known radius. These references are representative of the research found in the literature that considers "ideal" cases where either

- the sources are uniformly distributed onto the angular domain
- the channel capacity is an average capacity where the sources follow a statistical uniform distribution among the angular domain.

These scenarios are ideal in the sense that the level of interference is minimised and the contribution of the antenna array geometry is ignored.

In Chapter 2, the framework of the array manifold was presented and the most important parameters describing its shape were introduced. Notably, the inner product between two array manifold vectors was expressed in terms of the array manifold's differential geometry parameters. The present chapter, based on these new theoretical results, is organised as follows. In Section 4.2, the *capacity loss*, that is the loss of channel capacity induced by the presence of interferers, is formally introduced. This new theoretical derivation is then exploited to get insights into how an antenna array is able to deal with interferers. Finally, in Section 4.3, the capacity loss is evaluated for different array geometries and also the new concept of *capacity loss threshold*, that is the necessary distance between the

desired user and interferers to achieve a particular capacity loss, is presented. Finally, the Chapter is summarised in Section 4.4.

4.2 Channel Capacity Loss

Let us consider the vector $\underline{x}(t)$ received by an antenna array of N antennas operating in the presence of M signals incident to the array from different directions (directions of arrival). Using Eq. 2.9, the received signal can be modelled as follows

$$\underline{x}(t) = \sum_{i=1}^{M} \beta_i \underline{\mathrm{a}}_i \overline{\underline{\mathrm{a}}}_i^H \overline{\underline{m}}_i(t) + \underline{\mathrm{n}}(t) \tag{4.1}$$

where $\underline{\mathrm{a}}_i^H \overline{\underline{m}}_i(t)$ is the received message of the i-th signal with

$$\overline{\underline{m}}_i(t) = \overline{\underline{w}}_i(t) \odot \underline{m}_i(t), \tag{4.2}$$

and with $\overline{\underline{w}}_i(t)$ the transmit weights of the i-th user. Now, let us define $\mathbb{B}$ the matrix whose columns are the $M-1$ array manifold vectors of the interfering signals,

$$\mathbb{B} \triangleq [\underline{\mathrm{a}}_2, \underline{\mathrm{a}}_3, \ldots, \underline{\mathrm{a}}_M] \in \mathcal{C}^{N \times M-1}. \tag{4.3}$$

4.2.1 Second Order Statistics

The second order statistics of the signal $\underline{x}(t)$ are

$$\begin{aligned} \mathbb{R}_{xx} =& \mathcal{E}\left\{\underline{x}(t)\underline{x}(t)^H\right\} \\ =& \sum_{i=1}^{M}\sum_{k=1}^{M} \underline{\mathrm{a}}_i \overline{\underline{\mathrm{a}}}_i^H \mathcal{E}\left\{\beta_i \beta_k \overline{\underline{m}}_i(t) \overline{\underline{m}}_k(t)^H\right\} \overline{\underline{\mathrm{a}}}_k \underline{\mathrm{a}}_k^H + \sigma_{\mathrm{n}}^2 \mathbb{I}_N. \end{aligned} \tag{4.4}$$

With no loss of generality, it is considered that the transmitted messages are i.i.d Gaussian signals with powers P_i, leading to the follow-

ing properties

$$\mathcal{E}\{\overline{\underline{m}}_i(t)\overline{\underline{m}}_j^H(t)\} = \mathbb{O}_{\overline{N}\times\overline{N}},\ \forall i \neq j \tag{4.5}$$

$$\mathcal{E}\{\overline{\underline{m}}_i(t)\overline{\underline{m}}_i^H(t)\} = P_i\mathbb{I}_{\overline{N}}. \tag{4.6}$$

Also, for simplicity but without any loss of generality, it is considered that the complex path fading coefficients have unity magnitude and are included in P_j. A consequence of Eqs. 4.5 and 4.6 on the covariance matrices of Eq. 4.4 is that the cross products between multipath are suppressed. With this, and the array manifold property that $\overline{\underline{\mathrm{a}}}_i^H\overline{\underline{\mathrm{a}}}_i = \overline{N}$, the second order statistics are

$$\begin{aligned}\mathbb{R}_{xx} &= \sum_{i=1}^{M} P_i\underline{\mathrm{a}}_i\overline{\underline{\mathrm{a}}}_i^H\overline{\underline{\mathrm{a}}}_i\underline{\mathrm{a}}_i^H + \sigma_{\mathrm{n}}^2\mathbb{I}_N \\ &= \overline{N}\sum_{i=1}^{M} P_i\underline{\mathrm{a}}_i\underline{\mathrm{a}}_i^H + \sigma_{\mathrm{n}}^2\mathbb{I}_N \\ &= \overline{N}[\underline{\mathrm{a}}_1, \mathbb{B}]\mathbb{P}[\underline{\mathrm{a}}_1, \mathbb{B}]^H + \sigma_{\mathrm{n}}^2\mathbb{I}_N. \end{aligned} \tag{4.7}$$

For notational convenience, we denote $\mathbb{P}$ and $\mathbb{P}_{\mathrm{int}}$ as the diagonal matrices comprising of the users' powers and the interfering users' powers respectively, i.e.

$$\mathbb{P} = \mathrm{diag}\{P_1, P_2, \ldots P_M\} \tag{4.8}$$

$$\mathbb{P}_{\mathrm{int}} = \mathrm{diag}\{P_2, P_3, \ldots, P_M\}. \tag{4.9}$$

4.2.2 Mutual Information and MIMO Channel

Let us assume that we want to communicate with user 1, and that the parameters associated with its propagation channel are perfectly known. The amount of information that the base-station is able to receive from user 1, is given by the mutual information

$$\mathcal{I}\left(\overline{\underline{m}}_1; \underline{x}|\underline{\mathrm{a}}_1\right) = \mathcal{H}\left(\underline{x}|\underline{\mathrm{a}}_1\right) - \mathcal{H}\left(\left(\underline{x}|\underline{\mathrm{a}}_1\right)|\overline{\underline{m}}_1\right). \tag{4.10}$$

This is the mutual information between the MIMO channel input and output. In the case where the channel is deterministic, its entropy is null ($\mathcal{H}(\underline{\mathrm{a}}_1) = 0$), and the mutual information is

$$\mathcal{I}\left(\overline{\underline{m}}_1; \underline{x}\right) = \mathcal{H}\left(\underline{x}\right) - \mathcal{H}\left(\left(\underline{x}\right)|\overline{\underline{m}}_1\right). \tag{4.11}$$

The array output vector $\underline{x}$ is a multivariable Gaussian process, as the sum of Gaussian processes. Its entropy is simply

$$\mathcal{H}\left(\underline{x}\right) = \log_2 \det\left(\pi e \mathbb{R}_{xx}\right), \tag{4.12}$$

and equivalently the entropy $\mathcal{H}\left(\underline{x}|\overline{\underline{m}}_1\right)$ is the entropy $\mathcal{H}\left(\underline{x}\right)$ where the message $\overline{\underline{m}}_1$ is known, therefore

$$\mathcal{H}\left(\underline{x}|\overline{\underline{m}}_1\right) = \log_2 \det\left(\pi e \left(\mathbb{R}_{xx} - P_1 \overline{N} \underline{\mathrm{a}}_1 \underline{\mathrm{a}}_1^H\right)\right). \tag{4.13}$$

Hence, the mutual information described in Eq. 4.11 is simply

$$\mathcal{I}\left(\overline{\underline{m}}_1; \underline{x}\right) = \log_2 \left(\frac{\det \mathbb{R}_{xx}}{\det\left(\mathbb{R}_{xx} - P_1 \overline{N} \underline{\mathrm{a}}_1 \underline{\mathrm{a}}_1^H\right)}\right). \tag{4.14}$$

The channel capacity to transmit information in the presence of interfering users is the maximum mutual information between $\overline{\underline{m}}_1$ and $\underline{x}$, i.e.

$$C = \sup_{\overline{\underline{m}}_1} \mathcal{I}\left(\overline{\underline{m}}_1; \underline{x}\right). \tag{4.15}$$

This quantity is maximized when the transmitted signals are Gaussian

$$C = B \log_2 \left(\frac{\det\left(\mathbb{R}_{xx}\right)}{\det\left(\mathbb{R}_{xx} - P_1 \overline{N} \underline{\mathrm{a}}_1 \underline{\mathrm{a}}_1^H\right)}\right). \tag{4.16}$$

This is the maximum quantity of information, in bits/sec, that can be conveyed by the channel.

4.2.3 The Loss of Channel Capacity

The channel capacity presented in Eq. 4.16 has a meaningful structure that can be exploited, as described in Appendix 4.A. With this structure, the single-user channel capacity C_{SU} can be derived as

$$C_{\mathrm{SU}} = B \log_2 \left(1 + N\overline{N} \frac{P_1}{\sigma_{\mathrm{n}}^2} \right), \tag{4.17}$$

and the channel capacity with multiple access interference (MAI) is

$$C = B \log_2 \left(\overbrace{1 + N\overline{N} \frac{P_1}{\sigma_{\mathrm{n}}^2}}^{\text{Eq. 4.17}} \overbrace{- \overline{N} \frac{P_1}{\sigma_{\mathrm{n}}^2} \underline{\mathrm{a}}_1^H \mathbb{B} \sqrt{\mathbb{P}_{\mathrm{int}}} \left(\sqrt{\mathbb{P}_{\mathrm{int}}}^H \mathbb{B}^H \mathbb{B} \sqrt{\mathbb{P}_{\mathrm{int}}} + \frac{\sigma_{\mathrm{n}}^2}{\overline{N}} \mathbb{I}_{M-1} \right)^{-1} \sqrt{\mathbb{P}_{\mathrm{int}}}^H \mathbb{B}^H \underline{\mathrm{a}}_1}^{\text{MAI}} \right). \tag{4.18}$$

This novel expression is the channel capacity of a desired user in a multiuser MIMO system, where the contribution of the desired user and the degradation induced by the interferers to the capacity can be distinguished.

The same channel capacity can be expressed as

$$C = C_{\mathrm{SU}} - BC_{\mathrm{loss}}, \tag{4.19}$$

where the first term is the single user channel capacity C_{SU}, and the second component constitutes the loss of capacity due to the presence of the interferers. This is the degradation induced by the interferers termed as *capacity loss*.

Theorem 6 (Capacity Loss)**.** *The channel capacity loss induced by the interferers is expressed as,*

$$C_{\text{loss}} = -\log_2\left(1 - \frac{P_1\overline{N}}{N\overline{N}P_1 + \sigma_{\text{n}}^2} \times \underline{\text{a}}_1^H\mathbb{B}\sqrt{\mathbb{P}_{\text{int}}}\left(\sqrt{\mathbb{P}_{\text{int}}}^H\mathbb{B}^H\mathbb{B}\sqrt{\mathbb{P}_{\text{int}}} + \frac{\sigma_{\text{n}}^2}{\overline{N}}\mathbb{I}_{M-1}\right)^{-1}\sqrt{\mathbb{P}_{\text{int}}}^H\mathbb{B}^H\underline{\text{a}}_1\right). \quad (4.20)$$

For a given number of antennas N (and hence number of dimension of the complex space $\mathcal{C}^N$) and propagation environment, the geometrical quality of a given antenna array yields a distance between the interference subspace spanned by the columns of $\mathbb{B}$ ($\mathcal{L}\{\mathbb{B}\}$) and $\underline{\text{a}}_1$ and results in a particular loss of capacity.

4.3 Evaluation of Capacity Loss on Curves

Let us now consider a case when all the users are equipowered, with powers equal to one, and elevation is zero. The capacity loss presented in Theorem 6 can be expressed as a function of the differential geometry parameters of the array manifold as displayed by Eq. 4.21. To evaluate this, let us consider the case where the capacity loss is induced by a cluster of interferers. An illustration of this environment is made with Fig. 4.1. The desired source and interferers are located onto the θ-curve corresponding to zero elevation and it is assumed that the angular separation between the desired user and the interferer cluster is small enough to result in a capacity loss. The small spatial angular separation between the desired user and the first interferer is translated into a small arc length separation Δs, as shown in Fig. 4.1. Also, we consider that the interferers are uniformly distributed onto an arc-length $\Delta\tilde{s}$.

$$
\begin{aligned}
C_{\text{loss}}(s_1, s_2, \ldots, s_N) = -\log_2 \Bigg(1 - \frac{\overline{N}}{N\overline{N} + \sigma_{\text{n}}^2} \frac{\left(\left[\underline{\mathcal{R}}^H(s_1) \mathbb{M}_{s_1,s_2} \underline{\mathcal{R}}(s_2), \underline{\mathcal{R}}^H(s_2) \mathbb{M}_{s_2,s_3} \underline{\mathcal{R}}(s_3), \ldots, \underline{\mathcal{R}}^H(s_{N-1}) \mathbb{M}_{s_{N-1},s_N} \underline{\mathcal{R}}(s_N) \right]^H \right)}{N + \sigma_{\text{n}}^2} \\
\times \left[\begin{matrix} N, & \underline{\mathcal{R}}^H(s_3) \mathbb{M}_{s_3,s_2} \underline{\mathcal{R}}(s_2), & \underline{\mathcal{R}}^H(s_4) \mathbb{M}_{s_4,s_2} \underline{\mathcal{R}}(s_2), & \ldots, & \underline{\mathcal{R}}^H(s_N) \mathbb{M}_{s_N,s_2} \underline{\mathcal{R}}(s_2) \\ \underline{\mathcal{R}}^H(s_2) \mathbb{M}_{s_2,s_3} \underline{\mathcal{R}}(s_3), & N, & \underline{\mathcal{R}}^H(s_4) \mathbb{M}_{s_4,s_3} \underline{\mathcal{R}}(s_3), & \ldots, & \underline{\mathcal{R}}^H(s_N) \mathbb{M}_{s_N,s_3} \underline{\mathcal{R}}(s_3) \\ \underline{\mathcal{R}}^H(s_2) \mathbb{M}_{s_2,s_4} \underline{\mathcal{R}}(s_4), & \underline{\mathcal{R}}^H(s_3) \mathbb{M}_{s_3,s_4} \underline{\mathcal{R}}(s_4), & N, & \ldots, & \underline{\mathcal{R}}^H(s_N) \mathbb{M}_{s_N,s_4} \underline{\mathcal{R}}(s_4) \\ \vdots, & \vdots, & \vdots, & \ddots, & \vdots \\ \underline{\mathcal{R}}^H(s_2) \mathbb{M}_{s_2,s_N} \underline{\mathcal{R}}(s_N), & \underline{\mathcal{R}}^H(s_3) \mathbb{M}_{s_3,s_N} \underline{\mathcal{R}}(s_N), & \underline{\mathcal{R}}^H(s_4) \mathbb{M}_{s_4,s_N} \underline{\mathcal{R}}(s_N), & \ldots, & N \end{matrix} \right]^{-1} \\
\times \left(\left[\underline{\mathcal{R}}^H(s_1) \mathbb{M}_{s_1,s_2} \underline{\mathcal{R}}(s_2), \underline{\mathcal{R}}^H(s_2) \mathbb{M}_{s_2,s_3} \underline{\mathcal{R}}(s_3), \ldots, \underline{\mathcal{R}}^H(s_{N-1}) \mathbb{M}_{s_{N-1},s_N} \underline{\mathcal{R}}(s_N) \right] \right) \Bigg)
\end{aligned} \tag{4.21}
$$

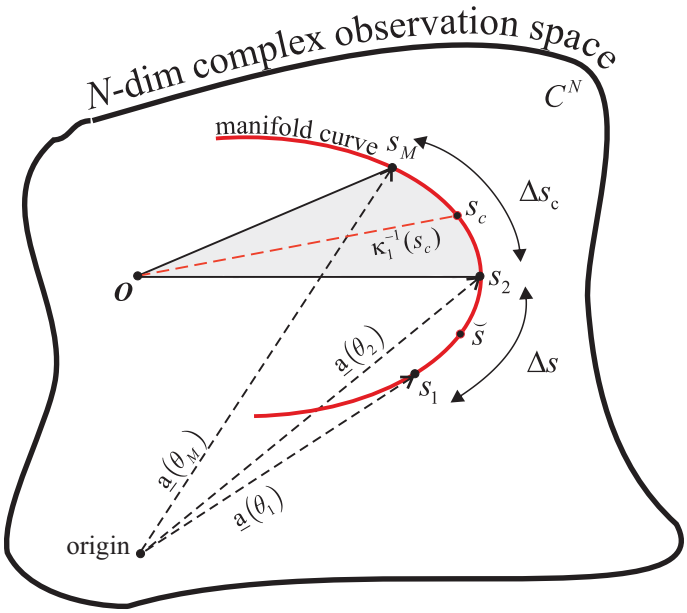


Figure 4.1: Representation of the array manifold vectors of the desired user $\underline{a}_1$ and interferers $\underline{a}_2, \ldots, \underline{a}_M$ on the array manifold curve $\mathcal{A}$. The arc length between the closest interferer and the desired user is to be Δs while the cluster size is Δs_c. The point O denotes the centre of curvature of the arc on which the interferer cluster lies with radius equal to $\kappa_1^{-1}(s_c)$.

In order to study the impact of the array manifold parameters on the capacity loss, two sets of five array geometries were employed. In the first set, all five geometries have the same number of antennas N but different aperture. In the second set, all five geometries have approximately the same aperture but a different number of antenna elements. A half-wavelength inter-antenna spacing was maintained across both sets of geometries. Also, all the geometries belong to the class of "2D grid arrays" [46] which satisfy the following conditions:

$$\underline{r}_x^T \underline{r}_y = 0 \text{ and } \|\underline{r}_x\| = \|\underline{r}_y\|. \tag{4.22}$$

In a first simulation study, the propagation environment was assumed to be composed of one desired user and three interferers, all equipowered. The arc length Δs_c was set such as the cluster of interfering users was 3^o wide, $\Delta\theta_c = 3^o$. In addition, the angular

separation $\Delta\theta_{1,2}$ was varied between 0° and 7°. For this environment, the resulting capacity loss for the five geometries is illustrated in Fig. 4.2 with varying $\Delta\theta_{1,2}$ and varying θ_1.

As mentioned in Section 2.2, the arc length and principal curvature are two crucial array manifold parameters and Eq. 4.21 indicates that there exists a trade-off between the array aperture, curvature and number of antennas. For the case of grid arrays [46], the length of the arc Δs is given by

$$\Delta s = \pi \left\| \underline{r}_x \right\| \Delta\theta_{1,2}, \tag{4.23}$$

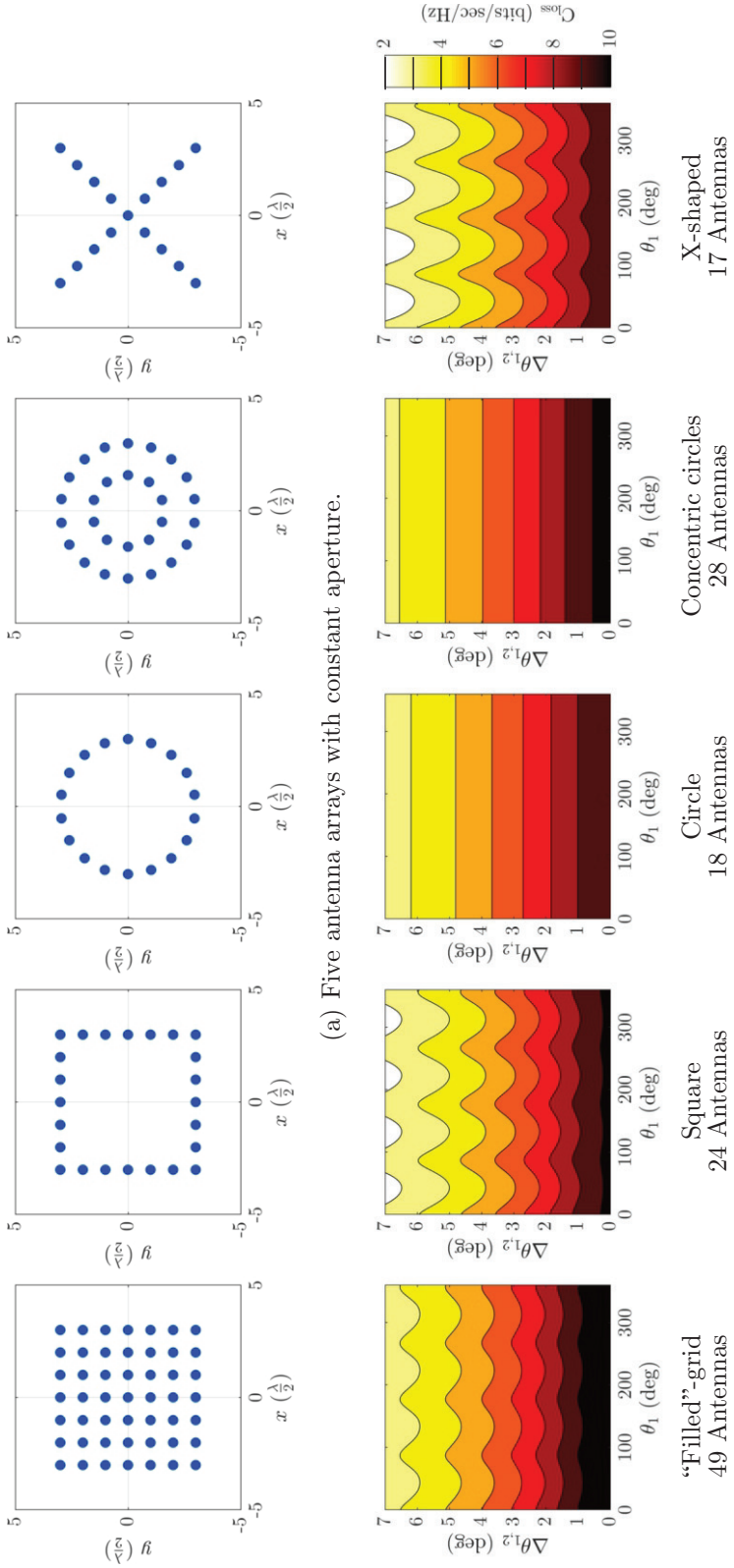
and, hence, is constant over the θ-curve for a fixed value of $\Delta\theta_{1,2}$ while increasing linearly with $\|\underline{r}_x\|$. In Fig. 4.2, this, in conjunction with Eq. 4.21, explains the decrease of C_{loss} with increasing $\Delta\theta_{1,2}$.

On the antenna array geometries of Fig. 4.2, where the aperture varies, the influence of Δs (Eq. 4.23) is high. This explains the ranking of geometries in Table 4.1 where the Circular array yields the lowest capacity loss, since it possesses the highest value of $\|\underline{r}_x\|$, and the "Filled"-grid has the highest capacity loss, since it possesses the lowest value of $\|\underline{r}_x\|$. The ranking with respect to total length of the manifold l_m also supports this statement. In Fig. 4.2, the best geometry is the Circular geometry because it yields the smallest C_{loss} for a given $\Delta\theta_{1,2}$. The same ranking also results by observing the capacity loss graphs shown in Fig. 4.2. Note that, in this case where is number of antenna is rather large, the norm $\|\underline{r}_x\|$ $\left(= \left\|\underline{r}_y\right\|\right)$ of the array geometry has more significance than the array aperture. Furthermore, when the value of $\|\underline{r}_x\|$ increases, the impact of the principal curvature κ_1 is magnified and this results in an increase in the capacity loss.

Figure 4.2: Five antenna arrays with equal number of antenna.

Table 4.1: Comparison (ranking) of the two sets of five array geometries based on the capacity loss.

	Fixed Number of Antennas ($N = 24$)			Equal Aperture		
Array geometry	$\|\underline{r}_x\| = \|\underline{r}_y\|$	Manifold length ℓ_m	Ranking	$\|\underline{r}_x\|$	Manifold length ℓ_m	Ranking
"Filled"-grid	7.07	139.58	last (5th)	14	276.35	4th
Square	12.08	238.51	3rd	12.08	238.51	2nd
Circle	13.23	261.19	best (1st)	9	177.65	3rd
Concentric circles	7.64	150.80	4th	9.68	191.04	last (5th)
X-shaped	12.59	248.45	2nd	8.22	162.17	best (1st)



(a) Five antenna arrays with constant aperture.

(b) Capacity loss C_{loss} for varying azimuth θ_1 and separation $\Delta\theta_{1,2}$ between the interfering cluster and desired user.

Figure 4.3: Five antenna arrays with similar apertures.

Let us now consider a second simulation study, where the capacity loss of another set of 2D grid arrays with similar apertures, displayed in Fig. 4.3a, is evaluated. Similar to the first study, the cluster angular width is $\Delta\theta_{\mathrm{c}} = 3^{\mathrm{o}}$ and the angular separation $\Delta\theta_{1,2}$ was varied between 0^{o} and 7^{o}. Figure 4.3b illustrates the capacity losses for this environment and Table 4.1 gives the corresponding performance ranking. An interesting result is that the "Square" array and X-shaped array yield a result very similar to that of the "Filled"-grid array even though the "Filled"-grid has a higher number of antennas. This can be explained by applying the result obtained in Eq. 4.21 for this set of geometries. Unlike the geometries in Fig. 4.2, the geometries in Fig. 4.3 have different number of antennas. This implies that there is now an interplay between three different parameters namely $\|\underline{r}_x\|$, κ_1 and N that results in the ranking given in Table 4.1. The relationship between these parameters dictates the performance ranking. The distance between the desired user and the cluster of interferer can be dramatically reduced by a poor design of the antenna array geometry if its corresponding array manifold curve is too curved (large curvature). Figure 4.2 illustrates that the performance of an array geometry with the largest number of antenna elements can be superseded by smaller arrays if its geometry is not designed carefully.

Figure 4.4 illustrates the variation in capacity loss for the arrays shown in Fig. 4.3 but with a varying number of interferers in the cluster M. Similar to with the previous studies, the interferer cluster is 3° wide and, the DOA of the desired user is fixed at $\theta_1 = 20^{\circ}$.

The separation $\Delta s = s_2 - s_1$ between the desired user and the

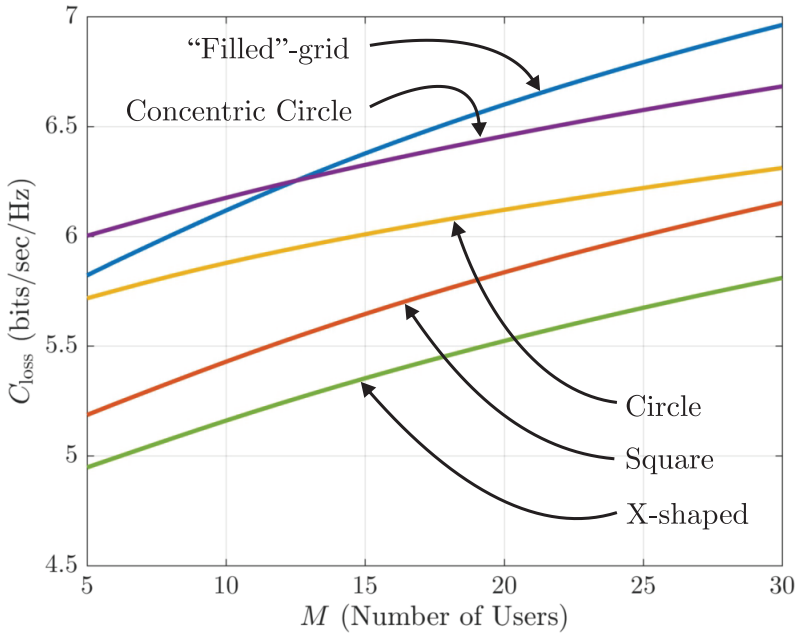


Figure 4.4: Capacity loss with a varying number of users M for the geometries in Fig. 4.3. The parameters utilised are $\theta_1 = 20^{\text{o}}$ and $\Delta\theta_{1,2} = 6^{\text{o}}$ with the $M-1$ interferers distributed within a Δs_{c}, which corresponds to $\Delta\theta_{\text{c}} = 3^{\text{o}}$.

second user (closest interference) is set such as $\Delta\theta_{1,2} = 6°$. Let us now consider the scenario where the desired user is located at the center of a cluster of 4 interferers (i.e. $M = 5$) with $\Delta\theta_{\text{c}} = 3°$. The DOA of the desired user θ_1 is varied and Fig. 4.5 illustrates the capacity loss for the geometries shown in Fig. 4.3a. It can be observed that the capacity loss is approximately the same for all geometries although the small difference in capacity loss is dictated by the number of antennas N. Overall, the results of these studies highlight the importance of this new metric of "capacity loss" derived in Eq. 4.20, and the interplay of the number of antennas N, the arc length Δs and the curvatures κ. This expression can be utilised as a cost function for future array design, especially for RF environments where high user density needs to be tackled.

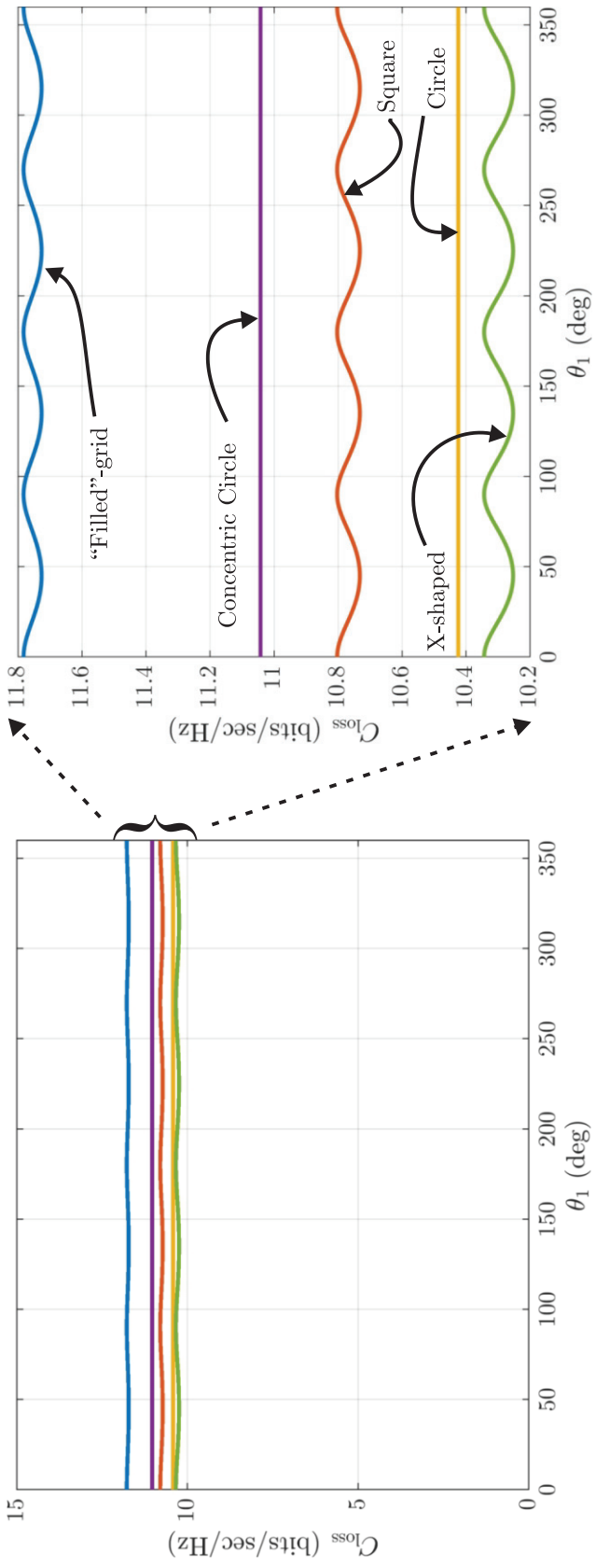


Figure 4.5: Capacity loss for the case that the desired user is located in the centre of the interferer cluster, i.e. $(s = s_c)$, plotted for $\forall s_1$ (i.e. $\forall \theta_1$. Cluster Δs_c is set such as to fix $\Delta\theta_c = 3°$.

4.3.1 Capacity Loss on Hyperhelical Curves

A particular class of curves, worthy of interest and described in Section 2.2.3, presents manifold curves having a hyperhelical shape. Particularly, the inner product between two array manifold vectors belonging to the same hyperhelical curve was characterised and displayed in Eq. 2.47. Utilizing this new result along with the capacity loss of 4.20, we can derive the capacity loss on hyperhelical curves, that is

Theorem 7 (Capacity Loss on Hyperhelical Curves)**.** *Considering the case when the M sources are on an hyperhelical curve, the loss of channel capacity induced by the interferers is*

$$C_{\text{loss}} = -\log_2\left(1 - \frac{\overline{N}}{N\overline{N}+\sigma_{\text{n}}^2} \times \left((N - \Delta s\underline{\mathcal{R}}^H\mathbb{C}\underline{\mathcal{R}})\underline{1}_{M-1} - \underline{\Delta s}\underline{\mathcal{R}}^H\mathbb{C}\underline{\mathcal{R}}\right)^H \left(\mathbb{B}^H\mathbb{B} + \frac{\sigma_{\text{n}}^2}{\overline{N}}\mathbb{I}_{M-1}\right)^{-1} \times \left((N - \Delta s\underline{\mathcal{R}}^H\mathbb{C}\underline{\mathcal{R}})\underline{1}_{M-1} - \underline{\Delta s}\underline{\mathcal{R}}^H\mathbb{C}\underline{\mathcal{R}}\right)\right). \quad (4.24)$$

Where we defined

$$\underline{\Delta s} = \left[0, \Delta s_2, \ldots, \sum_{i=2}^{M}\Delta s_i\right]^T, \quad (4.25)$$

for simplicity.

4.3.2 Capacity Loss Threshold

Now, to go one step further into this analysis, we define the *capacity loss threshold*. The Capacity loss threshold occurs when the separation between the desired source of interest and the interferers is small

enough to yield a capacity loss of 1 bits/sec/Hz. The required arc length between the desired user and the interferers to achieve this threshold is given by

$$\Delta s_{\text{thr}} = \frac{-N}{\underline{\mathcal{R}}^H \mathbb{C} \underline{\mathcal{R}}} - \frac{\text{Re}\left\{\underline{1}_{M-1}^H \left(\mathbb{B}^H\mathbb{B} + \frac{\sigma_{\text{n}}^2}{\overline{N}}\mathbb{I}_{M-1}\right)^{-1} \underline{\Delta s}\right\}}{\underline{1}_{M-1}^H \left(\mathbb{B}^H\mathbb{B} + \frac{\sigma_{\text{n}}^2}{\overline{N}}\mathbb{I}_{M-1}\right)^{-1} \underline{1}_{M-1}} + \frac{1}{2}\sqrt{\begin{array}{c} 4 - \frac{1}{(\underline{\mathcal{R}}^H \mathbb{C} \underline{\mathcal{R}})^2 \underline{1}_{M-1}^H \left(\mathbb{B}^H\mathbb{B} + \frac{\sigma_{\text{n}}^2}{\overline{N}}\mathbb{I}_{M-1}\right)^{-1} \underline{1}_{M-1}} \\ \times \left(\frac{N\overline{N} + \sigma_{\text{n}}^2}{\overline{N}} + \underline{\Delta s}^H \left(\mathbb{B}^H\mathbb{B} + \frac{\sigma_{\text{n}}^2}{\overline{N}}\mathbb{I}_{M-1}\right)^{-1} \underline{\Delta s}\right) \end{array}}. \quad (4.26)$$

The proof of 4.26 is detailed in Appendix 4.B. In the simplified case when there is one interferer only ($M = 2$), the interfering subspace is the array manifold vector of the interferer, the capacity loss is

$$C_{\text{loss}} = -\log_2\left(1 - \frac{\overline{N}}{N\overline{N} + \sigma_{\text{n}}^2} \frac{\left(N - \Delta s \underline{\mathcal{R}}^H \mathbb{C} \underline{\mathcal{R}}\right)^2}{\left(N + \frac{\sigma_{\text{n}}^2}{\overline{N}}\right)}\right) \quad (4.27)$$

and the minimum arc length to achieve the capacity loss threshold is

$$\Delta s_{\text{thr}} = \frac{N}{\underline{\mathcal{R}}^H \mathbb{C} \underline{\mathcal{R}}} + \sqrt{\frac{N\overline{N} + \sigma_{\text{n}}^2}{2N} \frac{1}{N + \frac{\sigma_{\text{n}}^2}{\overline{N}}}}. \quad (4.28)$$

An illustration of this concept is given by Fig. 4.6. The source and interferer are part of the x-y plan. The DOA of the source and its separation with the interferer was varied to yield the surface. The dark curve represents the DOA and angular separation at which the capacity loss threshold is achieved. The surface displayed in Fig 4.6 can be separated into two parts,

1. Above threshold, i.e. when $\Delta\theta \geq \Delta\theta_{\text{thr}}$. When the DOA separation is large enough, i.e. $\Delta\theta \geq \Delta\theta_{\text{thr}}$, the presence of interference has a small impact on the reception of the desired source,

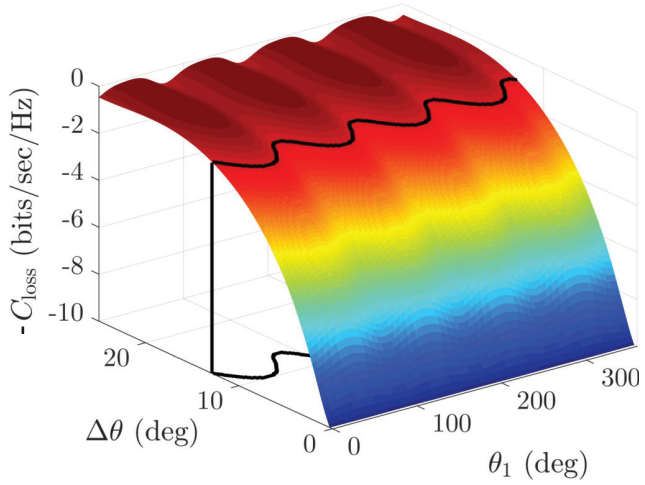


Figure 4.6: Capacity loss and capacity loss threshold for the square (b) antenna array geometry presented in Fig 2.3.a.

the capacity loss is negligible. In this zone, the channel capacity is only function of the noise level and the number of antennas.

2. Below threshold, i.e. when $\Delta\theta \leq \Delta\theta_{\text{thr}}$. As soon as the DOA separation $\Delta\theta$ becomes small, i.e. $\Delta\theta \leq \Delta\theta_{\text{thr}}$, the array manifold vectors of the sources come closer and closer in the N-dimensional complex space and the shape of the array manifold plays an important role.

As illustrated by Eq. 4.27, for a particular angular separation between the user and interferer $\Delta\theta$, the capacity loss will be dictated by the rate of growth of the arc length $\dot{s}(\theta)$ and the curvature $\underline{\mathcal{R}}^H \mathbb{C} \underline{\mathcal{R}}$ of the array manifold curve. For a particular number of antennas, a well-designed antenna array should deliver good performance in the range $0 < \Delta\theta \leq \Delta\theta_{\text{thr}}$, by reducing the capacity loss.

4.4 Summary

In this chapter, a novel theoretical framework is presented where the concept of capacity loss due to the presence of co-channel interferences is introduced, and linked to the antenna array geometry. By combining array processing, differential geometry and wireless communication, it was demonstrated that the presence of interferers has a negative impact on the ability of the antenna array to receive the source of interest when their angular separation is below a threshold and this is given by the capacity loss expression. The analytical results were supported by simulations studies, where it was demonstrated that in highly dense signal environments, array manifold parameters, such as the arc length and principal curvature, play a significant role in the mitigation of interferences. The analytical expressions for capacity loss can be crucial for the design of array geometries for specific propagation environments.

Appendix 4.A Structure of Eq. 4.16

Let us recall the covariance matrix of the received signal $\underline{x}$,

$$\begin{aligned}\mathbb{R}_{xx} &= \sum_{i=1}^{M} P_i \underline{\mathrm{a}}_i \overline{\underline{\mathrm{a}}}_i^H \overline{\underline{\mathrm{a}}}_i \underline{\mathrm{a}}_i^H + \sigma_{\mathrm{n}}^2 \mathbb{I}_N \\ &= \overline{N} \sum_{i=1}^{M} P_i \underline{\mathrm{a}}_i \underline{\mathrm{a}}_i^H + \sigma_{\mathrm{n}}^2 \mathbb{I}_N \\ &= \overline{N} [\underline{\mathrm{a}}_1, \mathbb{B}] \mathbb{P} [\underline{\mathrm{a}}_1, \mathbb{B}]^H + \sigma_{\mathrm{n}}^2 \mathbb{I}_N \end{aligned} \tag{4.29}$$

and the corresponding channel capacity (Eq. 4.16)

$$C = B \log_2 \left(\frac{\det \left(\sigma_{\mathrm{n}}^2 \mathbb{I}_N + \overline{N} \left[\underline{\mathrm{a}}_1, \mathbb{B} \right] \mathbb{P} \left[\underline{\mathrm{a}}_1, \mathbb{B} \right]^H \right)}{\det \left(\sigma_{\mathrm{n}}^2 \mathbb{I}_N + \overline{N} \mathbb{B} \mathbb{P}_{\mathrm{int}} \mathbb{B}^H \right)} \right). \tag{4.30}$$

The expression can be simplified using the matrix determinant lemma, as follows

$$C = B \log_2 \left(\frac{\det \left(\sigma_{\mathrm{n}}^2 \mathbb{I}_M + \overline{N} \sqrt{\mathbb{P}}^H \left[\underline{\mathrm{a}}_1, \mathbb{B} \right]^H \left[\underline{\mathrm{a}}_1, \mathbb{B} \right] \sqrt{\mathbb{P}} \right)}{\det \left(\sigma_{\mathrm{n}}^2 \mathbb{I}_{M-1} + \overline{N} \sqrt{\mathbb{P}_{\mathrm{int}}}^H \mathbb{B}^H \mathbb{B} \sqrt{\mathbb{P}_{\mathrm{int}}} \right) \sigma_{\mathrm{n}}^2} \right). \tag{4.31}$$

The term $\sigma_{\mathrm{n}}^2 \mathbb{I}_M + \overline{N} \sqrt{\mathbb{P}}^H \left[\underline{\mathrm{a}}_1, \mathbb{B} \right]^H \left[\underline{\mathrm{a}}_1, \mathbb{B} \right] \sqrt{\mathbb{P}}$ contains a structure that be can exploited to express 4.31 as blocks of matrices,

$$C = B \log_2 \left(\frac{\det \left(\begin{bmatrix} \sigma_{\mathrm{n}}^2 + P_1 \overline{N} N & \sqrt{P_1 N} \underline{\mathrm{a}}_1^H \mathbb{B} \sqrt{\mathbb{P}_{\mathrm{int}}} \\ \sqrt{P_1 N} \sqrt{\mathbb{P}_{\mathrm{int}}}^H \mathbb{B}^H \underline{\mathrm{a}}_1 & \overline{N} \sqrt{\mathbb{P}_{\mathrm{int}}}^H \mathbb{B}^H \mathbb{B} \sqrt{\mathbb{P}_{\mathrm{int}}} + \sigma_{\mathrm{n}}^2 \mathbb{I}_{M-1} \end{bmatrix} \right)}{\sigma_{\mathrm{n}}^2 \det \left(\overline{N} \sqrt{\mathbb{P}_{\mathrm{int}}}^H \mathbb{B}^H \mathbb{B} \sqrt{\mathbb{P}_{\mathrm{int}}} + \sigma_{\mathrm{n}}^2 \mathbb{I}_{M-1} \right)} \right), \tag{4.32}$$

and with the equality,

$$\det \left(\begin{bmatrix} \mathbb{E} & \mathbb{F} \\ \mathbb{G} & \mathbb{H} \end{bmatrix} \right) = \det \mathbb{H} \det \left(\mathbb{E} - \mathbb{F} \mathbb{H}^{-1} \mathbb{G} \right), \tag{4.33}$$

Eq. 4.32 resumes to

$$C = B\log_2\left(1 + \frac{P_1\overline{N}N}{\sigma_{\mathrm{n}}^2} - \frac{P_1\overline{N}}{\sigma_{\mathrm{n}}^2}\underline{\mathrm{a}}_1^H\mathbb{B}\sqrt{\mathbb{P}_{\mathrm{int}}}\left(\sqrt{\mathbb{P}_{\mathrm{int}}}^H\mathbb{B}^H\mathbb{B}\sqrt{\mathbb{P}_{\mathrm{int}}} + \frac{\sigma_{\mathrm{n}}^2}{\overline{N}}\mathbb{I}_{M-1}\right)^{-1}\sqrt{\mathbb{P}_{\mathrm{int}}}^H\mathbb{B}^H\underline{\mathrm{a}}_1\right). \tag{4.34}$$

This result is the proof of Eq. 4.18.

Appendix 4.B Proof of the Capacity Loss Threshold

The capacity loss threshold can be obtained by solving

$$\begin{aligned}&\left(N-\Delta s\underline{\mathcal{R}}^H\mathbb{C}\underline{\mathcal{R}}\right)^2\underline{1}_{M-1}^H\left(\mathbb{B}^H\mathbb{B}+\frac{\sigma_{\mathrm{n}}^2}{\overline{N}}\mathbb{I}_{M-1}\right)^{-1}\underline{1}_{M-1}\\&-2\left(N-\Delta s\underline{\mathcal{R}}^H\mathbb{C}\underline{\mathcal{R}}\right)\underline{\mathcal{R}}^H\mathbb{C}\underline{\mathcal{R}}\mathrm{Re}\left\{\underline{1}_{M-1}^H\left(\mathbb{B}^H\mathbb{B}+\frac{\sigma_{\mathrm{n}}^2}{\overline{N}}\mathbb{I}_{M-1}\right)^{-1}\underline{\Delta s}\right\}\\&+\left(\underline{\mathcal{R}}^H\mathbb{C}\underline{\mathcal{R}}\right)^2\underline{\Delta s}^H\left(\mathbb{B}^H\mathbb{B}+\frac{\sigma_{\mathrm{n}}^2}{\overline{N}}\mathbb{I}_{M-1}\right)^{-1}\underline{\Delta s}=\frac{N\overline{N}+\sigma_{\mathrm{n}}^2}{2\overline{N}}.\end{aligned}\quad(4.35)$$

Please note that the solution was chosen as the smallest value of Δs_{thr}.

Chapter 5

Spatiotemporal Channel Estimator and Beamformer for 5G

The SpatioTemporal ARray (STAR) manifold beamformer proposed in this chapter integrates space and time[1] in a single manifold vector, called the spatiotemporal manifold vector[2]. This considerably empowers the receiver to provide narrow spatiotemporal multi-beams and combat the path loss by focusing the antenna array gain towards a specific path's direction of interest at the right time (delay). Figure 5.1 provides a basic representation of the proposed system. Unlike earlier systems, the proposed beamformer explicitly compensates MAI and estimates DOA, delay, radial velocity (Doppler frequency) and complex path gains of all paths of the desired user. Also, the channel estimation algorithm employed is blind, unlike systems with pilots such as in [71]. Note that this is different from the spatiotemporal approaches discussed in [72] and [73], where due to a non-

[1]Please note that the concept of "space-time" here is not related/connected to space-time coding.

[2]This research was published in IEEE Transactions on Wireless Communications [2].

parametric approach, that ignores the array geometry and DOAs, an original estimate of the interference subspace is assumed known. An iterative channel identification approach has been utilised leading to high complexity that increases with the number of interferers and antennas, making it unsuitable for the large antenna arrays of future 5G systems.

5.1 Introduction

5.1.1 mmWave Beamformers and 5G

The unutilised millimetre wave (mm-wave) frequency band is seen as a promising candidate to augment the already saturated lower frequency bands for wireless communications. However, a major limitation at these frequencies is the increased propagation losses [74]. In addition, the mm-wave channel is known to be frequency selective [75, 76, 77], while foliage losses and rain attenuation for the mm-wave are significant and can limit the coverage severely. Furthermore, attenuation factors due to obstacles in non-line-of-sight (NLOS) communications are much higher as compared to their counterparts in the 1-3 GHz communications band. Another critical problem would be the interference management arising from high user density in small cell deployments. In such environments, typical power control mechanisms will be much harder to operate. Some of these interfering users may be closer ("near") to the receiver than the desired user ("far"), transmitting with relatively higher power than that of the desired user which may be far away, resulting in extremely high interference levels. The performance of the subspace technique proposed

in this chapter is independent of the interference to signal power ratio, also known as the near-far ratio (NFR), making it more suitable to handle the well known near-far problem *without* the need of power control. Lastly, at these frequencies, the size of the antenna elements shrinks. This enables designers to integrate many more antenna elements onto the user-end devices as compared to the conventional radio frequency communication bands.

Some research to demonstrate the practicability of mm-wave beamformer systems has been done in [78, 79] and particularly the mitigation of interference cancellation using beamspace multiple-input-multiple-output (MIMO) has been discussed in [80]. Outdoor propagation measurements carried out in the 28 GHz band illustrate that simple beam combining in itself can improve gain, counteract pathloss and shadow fading [81]. For the special case of a weak line-of-sight (LOS) path, a diversity eigenbeamformer has been proposed [82] which utilises the eigendecomposition of the channel covariance matrix. In [83], a precoding scheme (i.e. Tx beamforming) has been proposed assuming a known channel and no multiple access interference (MAI). Furthermore, in [84], using a uniform linear array, a pilot-based direction of arrival (DOA) estimator for the paths of a single user (no MAI) has been proposed.

5.1.2 Extension of Degrees of Freedom and Interference Cancellation

Additional degrees of freedom can be introduced by taking the polarisation of the antennas into account. In [85] an extension of the STAR manifold has been made to include the three polarisation pa-

rameters. This model was exploited in [86], for joint DOA–TOA estimation, and in [61] in the joint estimation of the polarisation–angle–delay of a crossed-dipole array. Finally, in [87], a RAKE and decorrelating receivers have been employed with this model. In [88], an investigation on the geometrical properties of a 3–parameters extended manifold has been achieved.

The degrees of freedom can be further increased by using the concept of virtual arrays. This is carried out by mapping the MIMO system to a virtual SIMO system with enhanced degrees of freedom. In [89] the virtual array concept has been extended to an arbitrary order of array processing. In [90] a novel transformation mapping an arbitrary planar array to a virtual uniform linear array (ULA) with a larger number of sensors is proposed. This transformation enables us to apply MIMO techniques devoted to ULA to planar arrays. In [91], an equivalent virtual SIMO radar representation of the MIMO radar system is established which enables the analysis of the full MIMO system geometry. Analytical expressions are derived to describe the key geometrical properties of the virtual array's manifold, which fully characterises the entire transmit-receive system geometry.

However, the absence of MAI (or failure to isolate interference from noise) and ignoring other channel parameters render the solutions of [83] and [84] incomplete. In a number of proposed beamformer solutions for mm-wave, the strategy of hybrid beamforming, i.e. combining analogue and digital beamforming, has been employed. This is with the objective of reducing design complexity and power burden arising from the numerous analogue front-end chains to support the increased number of antennas. In [52], a hybrid beam-

former consisting of analogue subarrays and a digital beamformer has been proposed. However, it exploits the spatial dimension alone and employs an expensive iterative DOA estimation procedure requiring more iterations at a lower signal-to-noise ratio (SNR). A hybrid beamformer maximising the receiver output SNR has been proposed in [53].

The majority of the proposed mm-wave beamformers uses criteria such as maximising SNR, signal-to-noise-plus-interference ratio (SNIR) or minimising the bit error rate (BER). However, these beamformers are built around a traditional "non-parametric" model while the proposed channel model in this paper belongs to the family of "parametric". Traditional MIMO channel models, although very popular, are "debatable" in the sense that they ignore the array geometry, which is one of the most important known parameter of interest of any antenna array systems. In this case, the channel is modelled by the "channel state information" (CSI) matrix whose elements are the overall path gains from each Tx antenna to each Rx antenna (rather than from Tx array to Rx array), devouring in this way the array geometry. Consequently, the estimation of the CSI is complex and in many cases impractical for a large antenna array system. On the other hand, parametric models are based on wave propagation characteristics/properties from the Tx antenna array to the Rx antenna array and model the channel in terms of its parameters such as operational frequency, Tx array geometry, Rx array geometry, number of multipaths and their associated directions, relative path delays, Doppler frequency shifts and complex path fading coefficients. Thus, the clear advantage of the proposed parametric

channel model is that powerful channel estimation is possible and practical which is not the case with the traditional (non-parametric) MIMO channel model.

5.1.3 Parametric Channel Estimation

The channel parameters, such as DOA, DOD, delays and polarisation parameters have to be estimated in order to receive the transmitted signal properly. The very powerful MUSIC algorithm proposed by Schmidt in [92] is frequently employed, the received data are compared with manifolds built with different parameters to form a cost function. Usually, no more than two parameters are jointly estimated for the sake of the computational complexity.

In [93] a preprocessor has been proposed to overcome the "coherence problem"and make the estimation of the TOA and DOA possible. To deal with a fast-changing channel, a H^{∞} type approach has been employed to track the TOA and DOA parameters of a multipath channel in [94], and a temporal smoothing procedure for severe frequency-selective channels in [95]. The accuracy of the joint TOA-DOA estimation has been improved by taking the 2D polarisation of the antenna elements into account in [85, 87], and with a circular linear array in [86]. A polar-STAR manifold and joint polarisation–angle–delay computationally efficient solution has been proposed in [61].

In [96, 97] an algorithm based on the STAR manifold concept has been proposed to improve the DOA-TOA estimation in a scattering multipath context by estimating the spread of the DOA. In [98] and in [99], a MIMO CP-free MC-CDMA model and a MUSIC-cost

function have been employed to estimate the TOA, DOA and diffusivity of a multipath frequency-selective diffused channel. To handle mobility, the Doppler shift has to be estimated. In [100], a joint DOA–Doppler estimation has been proposed.

Mainly, two approaches to estimate the DOD have been presented. A beam rotation approach has been proposed in [35] and in [101] and the strategy of jointly optimising the DOA and DOD has been followed in [102, 103, 104].

In the approach presented in [105], a channel identification technique was proposed to process both space and time at the same time in a single user case, with multipath. Particularly, the array responses of the frequency selective system, combined with the complex path fading coefficients were assumed known and different techniques were proposed to estimate the delays. The remainder of the chapter is organised as follows. In Section 5.2 the channel is modelled in terms of the array manifold vectors of both Tx and Rx arrays for a frequency selective MIMO channel. In Section 5.3, the design of the proposed spatiotemporal beamformer and its associated multiparameter channel estimator are presented. In Section 5.4, computer simulation studies are employed to evaluate the performance of the proposed approach under various scenarios. Finally, in Section 5.5, the chapter is summarised.

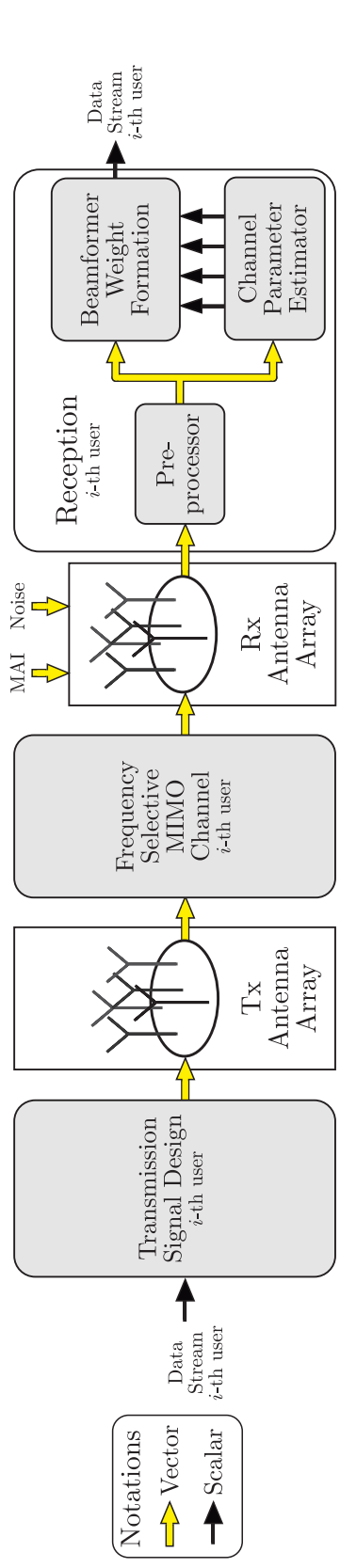


Figure 5.1: Basic representation of the proposed system consisting of signal design, MIMO channel model and receiver for the i-th user. The Rx antenna array operates as a physical vector adder adding the received signals from the i-th user, its MAI and noise effects.

5.2 MIMO Communications System Model

Consider an M user MIMO system where the transmitter and receiver utilise antenna arrays consisting of $\overline{N}$ and N antenna elements respectively, with all users operating simultaneously on the same frequency band. For the i-th user, the MIMO system model is split into the transmitter, channel and receiver entities/blocks which are described and mathematically modelled below[3].

5.2.1 Transmitter Model

Each of the M co-channel users employs a unique PN-code of period $\mathcal{N}_c$ and a set of $\mathcal{N}_{sc}$ orthogonal subcarriers. With reference to Fig. 5.2, consider at point A the input data symbol stream of the i-th user. This stream is demultiplexed into $\mathcal{N}_{sc}$ streams represented by the vector sequence $\{\underline{\mathrm{a}}_i[n]\}$,$\forall n$ (see point B). Each element of the transmitted symbol vector $\underline{\mathrm{a}}_i[n] \in C^{\mathcal{N}_{sc}\times 1}$ is assumed to be of unity magnitude (without any loss of generality). Then, the data stream vector $\{\underline{\mathrm{a}}_i[n]\}$, with a symbol period[4] T_{cs}, is spread by a PN-code sequence[5] of chip period T_c and sampling period T_s assigned to the i-th user. Let us define the vector $\underline{c}_i$ such that

$$\underline{c}_i = \underbrace{[\alpha_i[1], \alpha_i[2], \ldots, \alpha_i[\mathcal{N}_c]]}_{\text{one PN-code period}}^T \in \{+1, -1\}. \tag{5.1}$$

[3]Please note that, in this Chapter, $\underline{S}$ denotes the manifold vector while in the previous Chapter we used $\underline{\mathrm{a}}$.

[4]Note that the symbol period at point B is T_{cs} and symbol period at point A is $\frac{T_{cs}}{\mathcal{N}_{sc}}$.

[5]The use of PN-code is just a representative example of how we can integrate a modulation scheme with antenna array geometry. Note that instead of a PN-code we can use a Hadamard/Walsh sequence, or a chirp-pulse signal.

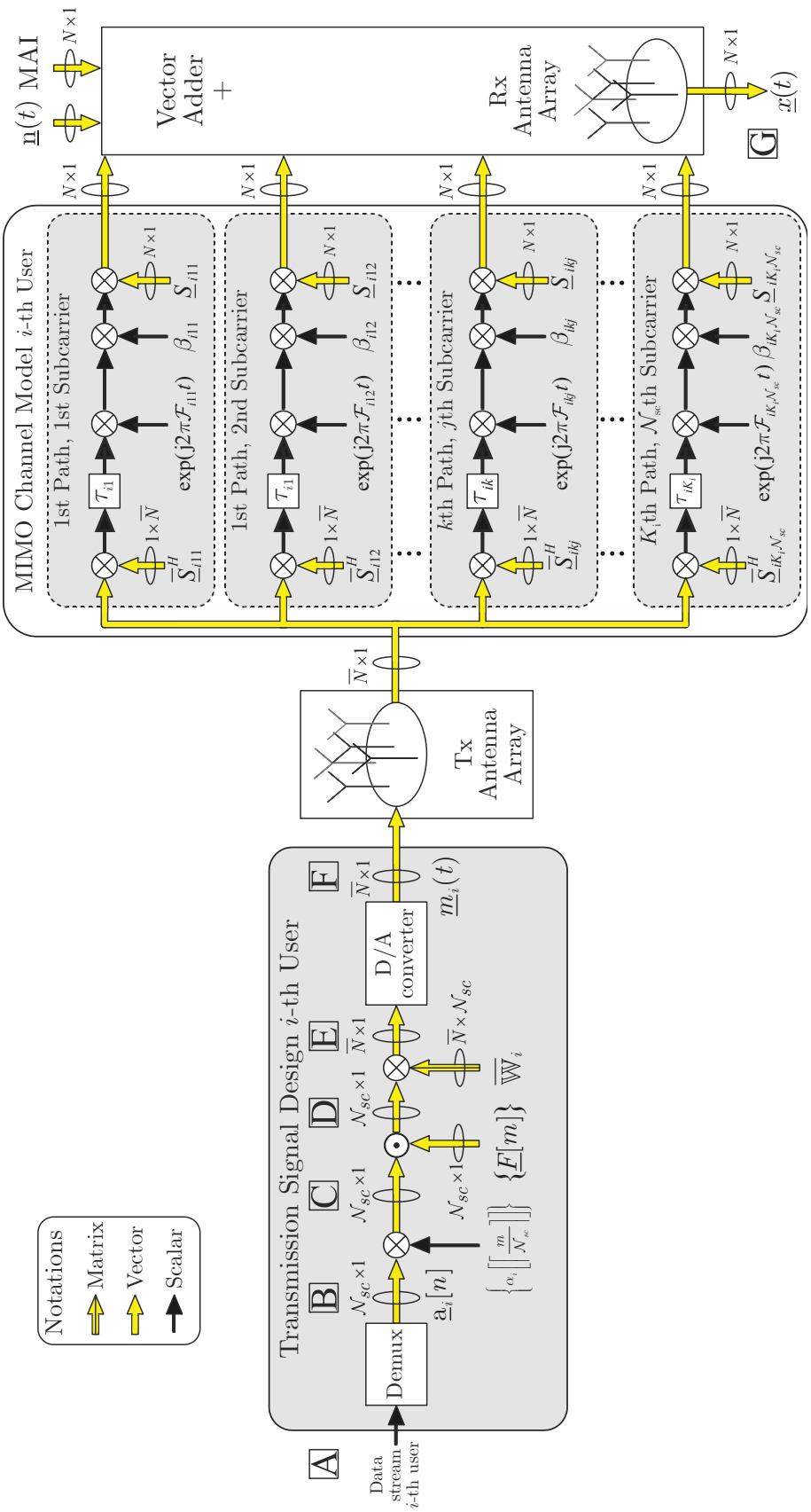


Figure 5.2: Baseband representation of the transmitter and the MIMO channel for the i-th user of the proposed system. Each subcarrier per path is modelled in terms of the Tx and Rx array geometries, path delay, Doppler frequency, complex path fading coefficient, DOA and DOD.

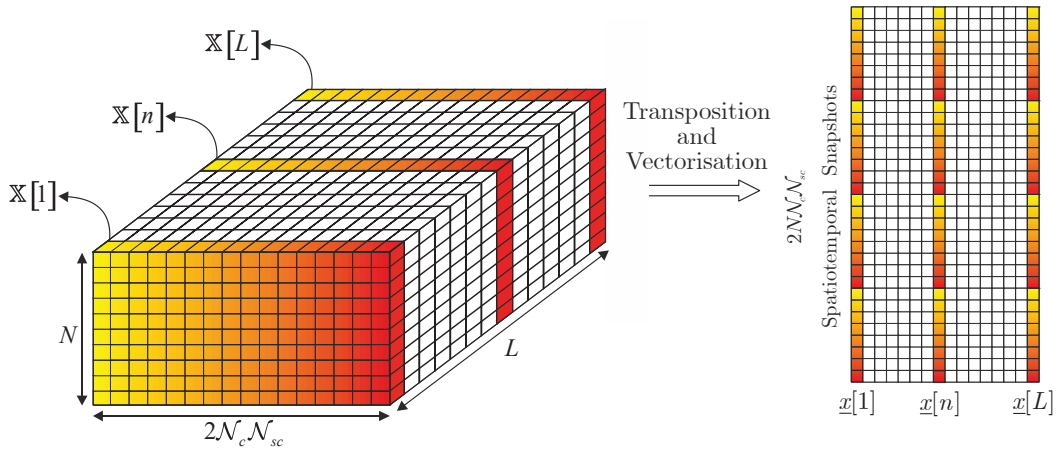
With $T_{cs} = \mathcal{N}_c T_c = \mathcal{N}_c \mathcal{N}_{sc} T_s$ at point C, for the $(\mathcal{N}_c \mathcal{N}_{sc} n + m)$-th interval, the transmitted vector at point C is given by $\underline{\mathrm{a}}_i [n] \, \alpha_i \left[\left[\frac{m}{\mathcal{N}_{sc}} \right] \right]$, $\forall m \in \{1, 2, \ldots, \mathcal{N}_c \mathcal{N}_{sc}\}$. This is then modulated onto the set of $\mathcal{N}_{sc}$ subcarriers denoted by the vector $\underline{F}[m]$ given as

$$\underline{F}[m] = \exp\left(\mathrm{j}2\pi \begin{bmatrix} F_1 \\ \vdots \\ F_j \\ \vdots \\ F_{\mathcal{N}_{sc}} \end{bmatrix} m \frac{T_c}{\mathcal{N}_{sc}} \right) \tag{5.2}$$

where $\mathrm{j} = \sqrt{-1}$ and the parameter $F_j = (j-1)\Delta F$ is the frequency offset of the j-th subcarrier from the main carrier frequency F_c and $\Delta F = \frac{1}{T_c}$ is the subcarrier spacing. Note that the proposed model is also applicable to a single carrier system as well as for a signal copy scheme instead of demultiplexing. Thus, at point D and for the $(\mathcal{N}_c \mathcal{N}_{sc} n + m)$-th interval, the transmitted vector is $\underline{\mathrm{a}}_i [n] \, \alpha_i \left[\left[\frac{m}{\mathcal{N}_{sc}} \right] \right] \odot \underline{F}[m]$. Following this, the transmitter weight matrix of the i-th user $\overline{\mathbb{W}}_i \in C^{\overline{N} \times \mathcal{N}_{sc}}$, i.e.

$$\overline{\mathbb{W}}_i = \left[\underline{\overline{w}}_{i1}, \underline{\overline{w}}_{i2}, \ldots, \underline{\overline{w}}_{i\mathcal{N}_{sc}} \right], \tag{5.3}$$

is applied on the modulated and spread data stream vector, at point D of Fig. 5.2, to steer all the subcarriers of the transmitter main lobe towards a desired DOA during the instant $(\mathcal{N}_c \mathcal{N}_{sc} n + m)$, yielding $\overline{\mathbb{W}}_i \left(\underline{\mathrm{a}}_i [n] \, \alpha_i \left[\left[\frac{m}{\mathcal{N}_{sc}} \right] \right] \odot \underline{F}[m] \right)$ (see point E). Note that, the transmitter weights $\underline{\overline{w}}_{ij}$ may be designed based on the feedback from the receiver. The design of these transmitter weights is out of the scope of this paper. The sequence of samples of the n-th symbol of the i-th user, obtained at point D, can be written in the form of a matrix $\mathbb{M}_i[n]$



(a) 3D data cube matrix at the output of the TDLs

(b) Vectorisation of the 3D data cube matrix

Figure 5.3: The 3D data cube and its vectorisation to form the spatiotemporal snapshot x.

given by

$$\mathbb{M}_i[n] = \left(\underline{a}_i[n] \otimes (\underline{c}_i \otimes \underline{1}_{\mathcal{N}_{sc}})^T\right) \odot \mathbb{F}[n] \in \mathcal{C}^{\mathcal{N}_{sc} \times \mathcal{N}_c \mathcal{N}_{sc}}, \tag{5.4}$$

where the matrix $\mathbb{F}[n] \in C^{\mathcal{N}_{sc} \times \mathcal{N}_c \mathcal{N}_{sc}}$ represents the discretised points of the subcarrier vector, namely $\exp\left(\mathrm{j}2\pi[F_1, \ldots, F_{\mathcal{N}_{sc}}]^T t\right)$, at the time instants $t = \left\{(n\mathcal{N}_c\mathcal{N}_{sc} + 1)\frac{T_c}{\mathcal{N}_{sc}}, \ldots, (n+1)\mathcal{N}_c\mathcal{N}_{sc}\frac{T_c}{\mathcal{N}_{sc}}\right\}$, and is given by

$$\mathbb{F}[n] = [\underline{F}[n\mathcal{N}_c\mathcal{N}_{sc} + 1], \ldots, \underline{F}[(n+1)\mathcal{N}_c\mathcal{N}_{sc}]. \tag{5.5}$$

Finally, the $\left(\overline{N} \times 1\right)$ message signal vector obtained at the output of the digital to analog (D/A) convertor (see point F) is transmitted onto the Tx antenna array of $\overline{N}$ antennas.

5.2.2 Simplification to Single-Carrier System:

In the case of a single-carrier simplification of the proposed spatiotemporal multicarrier system, $\mathcal{N}_{sc}$ becomes equal to one and therefore, the subscript j, corresponding to the j-th subcarrier,

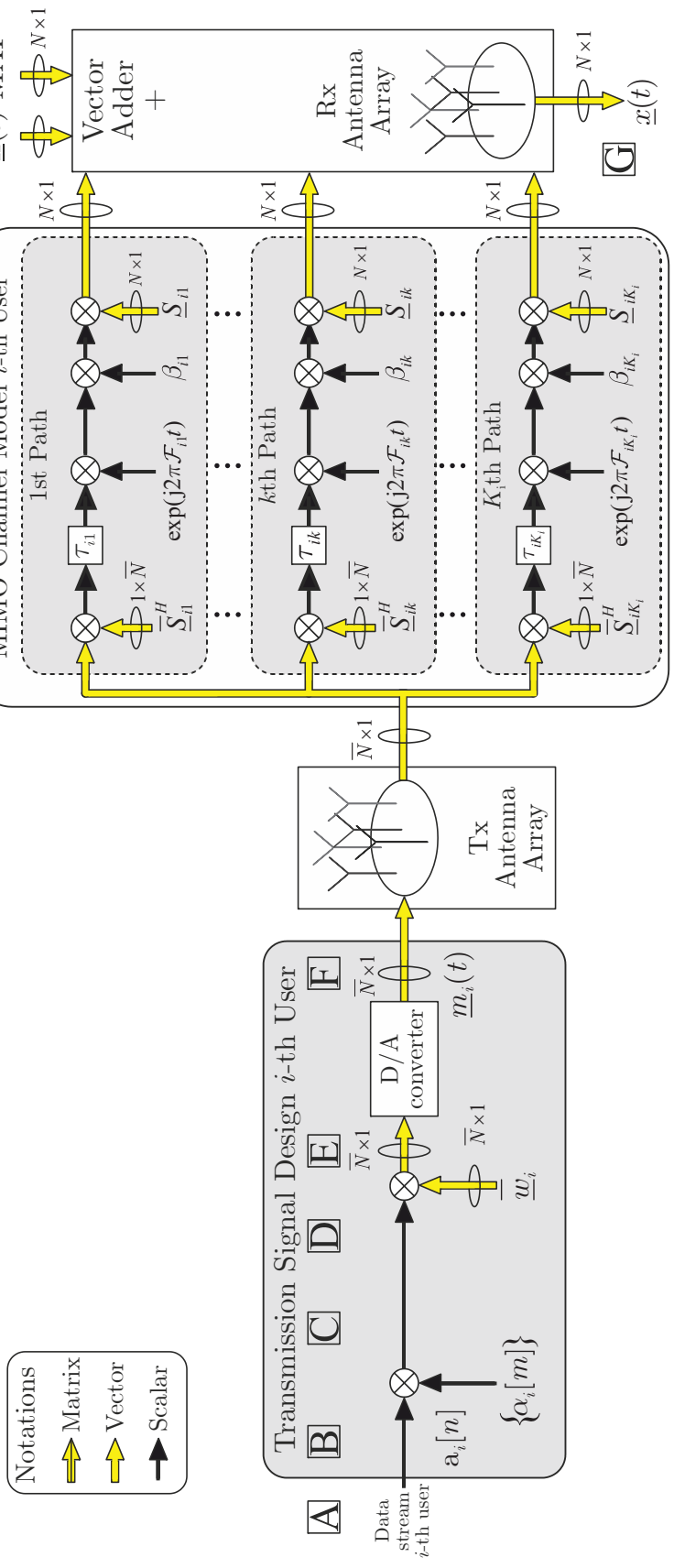


Figure 5.4: Baseband representation of the transmitter and the MIMO channel for the i-th user of the SC-DS-CDMA system.

may now be dropped in all the expressions and in Fig. 5.2. Thus, in this case, Fig. 5.2 simplifies to Fig. 5.4.

5.2.3 Channel Model Based on the Manifold Vectors

The channel, which is illustrated in Fig. 5.2 (from point F to G), is assumed to be a frequency selective arrayed MIMO channel, as suited to mm-wave, and stationary over a small interval of L spatiotemporal snapshots. The subscripts i, k and j are used to represent the user, multipath and subcarrier respectively (i-th user, k-th multipath and j-th subcarrier).

Suppose that the transmitted signal from the i-th user arrives at the receiver via K_i paths. As illustrated in Fig. 5.2, the branch of the channel which represents the k-th path, j-th subcarrier of the i-th user, is modelled with the Tx and Rx antenna array manifold vectors $\overline{\underline{S}}_{ikj} \in \mathcal{C}^{\overline{N}\times 3}$ and $\underline{S}_{ikj} \in \mathcal{C}^{N\times 3}$ respectively, a Doppler frequency shift $\mathcal{F}_{ikj}$ and path fading coefficient β_{ikj}. The parameter τ_{ik} denotes the time delay from the reference points of the Tx array to the Rx array.

The Rx antenna array manifold vector also known as spatial array manifold vector for the k-th path of the i-th user on the j-th subcarrier is defined as [46]:

$$\begin{aligned}\underline{S}_{ikj} &= \underline{S}(\theta_{ik}, \phi_{ik}, F_j) \\ &= \exp\left(-\mathrm{j}2\pi \frac{F_c + F_j}{c} [\underline{r}_x, \underline{r}_y, \underline{r}_z] \underline{u}(\theta_{ik}, \phi_{ik})\right), \end{aligned} \tag{5.6}$$

where $[\underline{r}_x, \underline{r}_y, \underline{r}_z] \in \mathcal{R}^{N\times 3}$ are the Cartesian coordinates of the receiver antenna array in metres, c is the speed of light and $\underline{u}(\theta_{ik}, \phi_{ik})$ points towards the direction of propagation

$$\underline{u}(\theta_{ik}, \phi_{ik}) \triangleq [\cos\theta_{ik}\cos\phi_{ik}, \sin\theta_{ik}\cos\phi_{ik}, \sin\phi_{ik}]^T, \tag{5.7}$$

with (θ_{ik}, ϕ_{ik}) denoting (azimuth, elevation) representing the DOA of the k-th path. Similarly, using $\overline{(\cdot)}$, i.e. a "bar" at the top of a symbol, to denote all equivalent parameters associated with the transmit array $[\overline{r}_x, \overline{r}_y, \overline{r}_z] \in \mathcal{R}^{\overline{N}\times 3}$, the transmit array manifold vector is denoted by

$$\overline{\underline{S}}_{ikj} \triangleq \overline{\underline{S}}(\overline{\theta}_{ik}, \overline{\phi}_{ik}, F_j) \tag{5.8}$$

with $\left(\overline{\theta}_{ik}, \overline{\phi}_{ik}\right)$ representing the direction of departure (DOD) of the k-th path of the i-th user. With reference to point G in Fig. 5.2, the $N \times 1$ baseband signal at the Rx antenna array can be modelled as follows

$$\underline{x}(t) = \sum_{i=1}^{M} \sum_{k=1}^{K_i} \sum_{j=1}^{\mathcal{N}_{sc}} \beta_{ikj} \exp\left(\mathrm{j}2\pi\mathcal{F}_{ikj}t\right) \underline{S}_{ikj} \times \overline{\underline{S}}_{ikj}^{H} \overline{\underline{w}}_{ij} m_{ij}\left(t - \tau_{ik}\right) + \underline{\mathrm{n}}\left(t\right), \tag{5.9}$$

where for the i-th user, j-th subcarrier and k-th path, the parameters β_{ikj}, $\mathcal{F}_{ikj}$ and τ_{ik} represent the complex path fading coefficient, the Doppler frequency and relative multipath delay respectively where

$$\mathcal{F}_{ikj} = -\frac{\left(F_c + F_j\right) v_{ik}}{c}, \tag{5.10}$$

with v_{ik} being the radial velocity of the i-th user's k-th path. The radial velocity is measured with respect to the Rx array reference point (i.e. $[0, 0, 0]$ Cartesian coordinate system). Note that the positive value of the radial velocity represents the same direction as $\underline{u}$. This is true for any relative motion in the wave propagation's path between Tx and Rx that changes the path's direction (i.e. radial velocity). In Eq. 5.9, $m_{ij}\left(t\right)$ is the transmitted baseband message by the i-th user on the j-th subcarrier at time t. Furthermore, $\underline{\mathrm{n}}(t)$ is additive circular white Gaussian noise of zero mean and covariance

matrix $\sigma_{\mathrm{n}}^2\mathbb{I}_N$, where σ_{n}^2 denotes the unknown noise power. In this paper, with no loss of generality, the users are assumed to be located in the (x, y) plane that is, zero elevation angles, i.e. $\phi_{ik} = \overline{\phi}_{ik} = 0\ \forall i, k$. The parametric model described helps in expressing the received antenna array signal vector $\underline{x}(t)$ (and its associated 2nd order statistics) as a function of the channel parameters (as shown in Eq. 5.9) and consequently enables the design of very powerful channel estimators and receiver/beamformers.

5.2.4 Receiver Model

The received signal $\underline{x}(t)$, which is shown at point G in Fig. 5.2 and Fig. 5.5, is fed to a preprocessor consisting of a discretiser of a sampling period $T_s = \frac{T_c}{\mathcal{N}_{sc}}$ and a bank of N tapped delay lines (TDLs) of length $2\mathcal{N}_c\mathcal{N}_{sc}$. Since, the generic case of asynchronous systems is considered, the transmitted data symbols do not arrive at the antennas at the beginning of their interval but with a relative delay. Thus, during the nT_{cs} period, the TDLs contain the contribution of the n-th Tx symbol plus some information of the previous $(n-1)$ and next $(n+1)$ symbols. In this paper, we use the term inter symbol interference (ISI) to represent this contribution arising from this preprocessor.

Figure 5.3a shows the 3D data cube which represents the received discretised signal, where the n-th slice of the data cube matrix is of size $N \times 2\mathcal{N}_c\mathcal{N}_{sc}$ corresponding to the data stored in the bank of TDLs at the nT_{cs} period. The vectorisation of the transposed n-th data slice provides the n-th spatiotemporal snapshot $\underline{x}[n] \in C^{2N\mathcal{N}_c\mathcal{N}_{sc}\times 1}$ as shown in Fig. 5.3b. Hence, the output $\underline{x}[n]$ at point H in Fig. 5.5

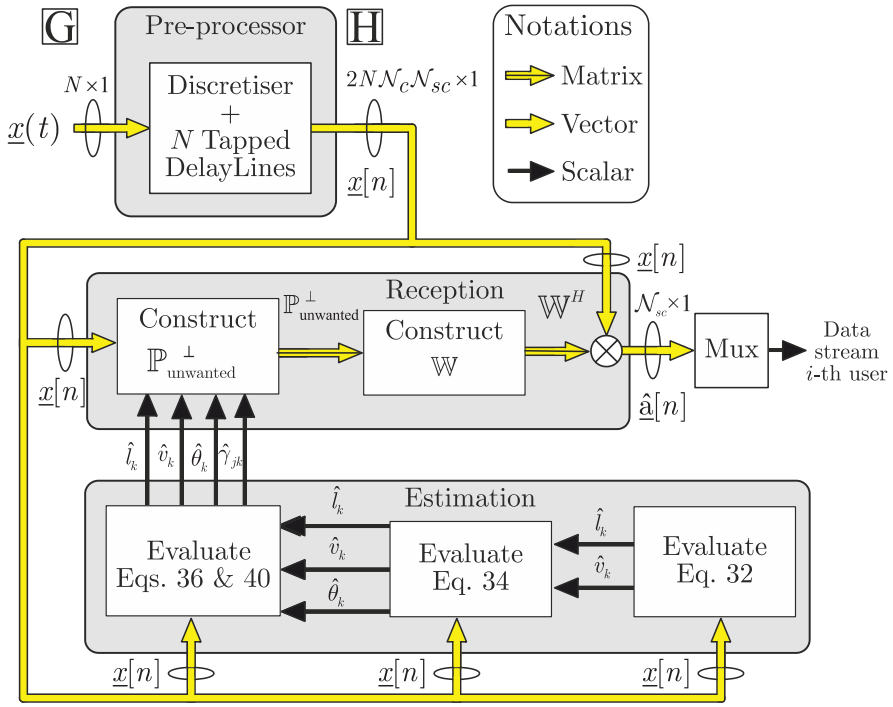


Figure 5.5: Block diagram of the preprocessor consisting of the discretiser and TDLs, followed by the channel estimator and the STAR-subspace receiver. Please note that the subscript i has been set to one and hence has been ignored.

can be written as

$$\underline{x}[n] = \text{vec}\left(\mathbb{X}^T[n]\right), \tag{5.11}$$

and this section presents the mathematical model of the same. Thus, the vector $\underline{x}[n]$ contains the n-th symbol of the desired user along with ISI, MAI and noise effects. In order to model these contributions, for the i-th user, j-th subcarrier and k-th path, the concept of the array manifold vector is extended to the Doppler-spatiotemporal array (Doppler-STAR) manifold vector $\underline{\mathfrak{h}}_{ikj} \in \mathcal{C}^{2N\mathcal{N}_c\mathcal{N}_{sc}\times 1}$ [106] given as follows

$$\underline{\mathfrak{h}}_{ikj} = \underline{S}_{ikj} \otimes \left(\mathbb{J}^{l_{ik}}\underline{\mathfrak{a}}_j[l_{ik}] \odot \underline{\mathcal{F}}_{ikj}\right) = \mathbb{A}_{ikj}\underline{S}_{ikj}, \tag{5.12}$$

where $\mathbb{A}_{ikj} \in C^{2N\mathcal{N}_c\mathcal{N}_{sc}\times N}$ is the linear mapping between the space-only manifold vector $\underline{S}_{ikj}$ and the Doppler-STAR manifold vector

$\underline{\mathfrak{h}}_{ikj}$ defined as

$$\mathbb{A}_{ikj} = \mathbb{I}_N \otimes \left(\mathbb{J}^{l_{ik}} \underline{\mathfrak{a}}_j \left[l_{ik} \right] \odot \underline{\mathcal{F}}_{ikj} \right). \tag{5.13}$$

The matrix $\mathbb{J}$ (or $\mathbb{J}^T$) is a $2\mathcal{N}_c\mathcal{N}_{sc} \times 2\mathcal{N}_c\mathcal{N}_{sc}$ matrix and the power l of $\mathbb{J}$ (or $\mathbb{J}^T$) when applied to a vector $\underline{x}$, i.e. $\mathbb{J}^l\underline{x}$ (or $\left(\mathbb{J}^T\right)^l\underline{x}$), downshifts (or upshifts) the vector $\underline{x}$ by l elements and is given as follows

$$\mathbb{J} = \begin{bmatrix} \underline{0}^T_{2\mathcal{N}_c\mathcal{N}_{sc}-1} & 0 \\ \mathbb{I}_{2\mathcal{N}_c\mathcal{N}_{sc}-1} & \underline{0}_{2\mathcal{N}_c\mathcal{N}_{sc}-1} \end{bmatrix}. \tag{5.14}$$

In Eq. 5.12, the parameter $l_{ik} = \left\lfloor \frac{\tau_{ik}}{T_s} \right\rfloor \mathrm{mod} \mathcal{N}_c\mathcal{N}_{sc}$ stands for the discrete relative path delay. Also, the vector $\underline{\mathfrak{a}}_j[l_{ik}] \in \mathcal{C}^{2\mathcal{N}_c\mathcal{N}_{sc}\times 1}$ that incorporates the temporal variation is defined as follows

$$\underline{\mathfrak{a}}_{ikj} \triangleq \underline{\mathfrak{a}}_j[l_{ik}] = (\underline{c}_i \underline{0}_{\mathcal{N}_c} \otimes \underline{1}_{\mathcal{N}_{sc}}) \odot \begin{bmatrix} \exp(\mathrm{j}2\pi F_j \left(0 - l_{ik}\right) T_s) \\ \exp(\mathrm{j}2\pi F_j \left(1 - l_{ik}\right) T_s) \\ \vdots \\ \exp(\mathrm{j}2\pi F_j \left(\mathcal{N}_c\mathcal{N}_{sc} - 1 - l_{ik}\right) T_s) \\ \underline{0}_{\mathcal{N}_c\mathcal{N}_{sc}}. \end{bmatrix} \tag{5.15}$$

The temporal variation within a symbol arising from the Doppler frequency shift is modelled as the vector $\underline{\mathcal{F}}_{ikj} \in \mathcal{C}^{2\mathcal{N}_c\mathcal{N}_{sc}\times 1}$ written as

$$\underline{\mathcal{F}}_{ikj} = \exp\left(\mathrm{j} \left[0, 1, \ldots, 2\mathcal{N}_c\mathcal{N}_{sc} - 1\right]^T 2\pi \mathcal{F}_{ikj} T_s \right). \tag{5.16}$$

Using the Doppler-STAR manifold vector defined in Eq. 5.12, we can model the n-th spatiotemporal snapshot $\underline{x}[n]$ as follows

$$\underline{x}[n] = \sum_{i=1}^{M} \sum_{j=1}^{\mathcal{N}_{sc}} \left[\mathbb{H}_{ij}, \mathbb{H}^{\mathrm{comb}}_{ij} \right] \begin{bmatrix} \left(\underline{\gamma}_{ij} \odot \underline{f}_{ij}[n] \right) \mathrm{a}_{ij}[n] \\ \left(\underline{\gamma}_{ij} \odot \underline{f}_{ij}[n-1] \right) \mathrm{a}_{ij}[n-1] \\ \left(\underline{\gamma}_{ij} \odot \underline{f}_{ij}[n+1] \right) \mathrm{a}_{ij}[n+1] \end{bmatrix} + \underline{\mathrm{n}}[n], \tag{5.17}$$

where $\mathrm{a}_{ij}[n]$ represents the symbol transmitted by the i-th user on the j-th subcarrier and $\underline{\mathrm{n}}[n]$ represents the sampled noise. Although subcarriers are employed, strictly speaking, we do not use the "frequency domain" as all the subcarriers are expressed in the time domain. Thus, the proposed approach belongs to the family of spatiotemporal techniques. Note that the above equations are simplified to the single carrier system by applying $\mathcal{N}_{sc} = 1$ and dropping the subscript j representing the subcarrier index. The matrix $\mathbb{H}_{ij}$ contains the Doppler-STAR manifold vectors of all the multipaths of the j-th subcarrier of the i-th user, constructed as follows

$$\mathbb{H}_{ij} = [\underline{\mathfrak{h}}_{i1j}, \underline{\mathfrak{h}}_{i2j}, ..., \underline{\mathfrak{h}}_{iK_ij}] \in \mathcal{C}^{2N\mathcal{N}_c\mathcal{N}_{sc}\times K_i}. \tag{5.18}$$

In Eq. 5.17, the matrix $\mathbb{H}_{ij}^{\text{comb}} \in \mathcal{C}^{2N\mathcal{N}_c\mathcal{N}_{sc}\times 2K_i}$ contains delayed versions of the matrix $\mathbb{H}_{ij}$ (ISI) and is defined as

$$\mathbb{H}_{ij}^{\text{comb}} = \left[(\mathbb{I}_N \otimes (\mathbb{J}^T)^{\mathcal{N}_c\mathcal{N}_{sc}})\mathbb{H}_{ij}, (\mathbb{I}_N \otimes (\mathbb{J})^{\mathcal{N}_c\mathcal{N}_{sc}})\mathbb{H}_{ij}\right]. \tag{5.19}$$

In addition, the vector $\underline{\gamma}_{ij}$ contains the path fading coefficients and the gain provided by transmit beamforming for all the multipaths of the j-th subcarrier of the i-th user. That is,

$$\underline{\gamma}_{ij} = \underline{\beta}_{ij} \odot \left[\overline{\underline{S}}_{j1}^H \overline{\underline{w}}_{ij}, \ldots, \overline{\underline{S}}_{jK_i}^H \overline{\underline{w}}_{ij}\right]^T, \tag{5.20}$$

where the vector $\underline{\beta}_{ij} \in \mathcal{C}^{K_i\times 1}$

$$\underline{\beta}_{ij} = [\beta_{i1j}, \beta_{i2j}, ..., \beta_{iK_ij}]^T, \tag{5.21}$$

contains the K_i multipath fading coefficients of the j-th subcarrier of the i-th user. Finally, the vector $\underline{f}_{ij}[n] \in \mathcal{C}^{K_i\times 1}$ incorporates the temporal variation of the subcarriers and Doppler shift from one symbol to the other, defined as

$$\underline{f}_{ij}[n] = \exp(\mathrm{j}2n\pi F_j T_{cs}) \exp\left(\mathrm{j}2n\pi \left[\mathcal{F}_{i1j}, \ldots, \mathcal{F}_{iK_ij}\right]^T T_{cs}\right). \tag{5.22}$$

Without any loss of generality, the first user is assumed to be the desired user, i.e. $i = 1$, and thus $\underline{x}[n]$ can be rewritten as follows to distinguish the desired signal, ISI, MAI and noise component

$$\begin{aligned}\underline{x}[n] = &\overbrace{\sum_{j=1}^{\mathcal{N}_{sc}} \mathbb{H}_{1j} \left(\underline{\gamma}_{1j} \odot \underline{f}_{1j}[n]\right) \mathrm{a}_{1j}[n]}^{\text{Desired term}} \\ &+ \overbrace{\sum_{j=1}^{\mathcal{N}_{sc}} \mathbb{H}_{1j}^{\text{comb}} \begin{bmatrix} \left(\underline{\gamma}_{1j} \odot \underline{f}_{1j}[n-1]\right) \mathrm{a}_{1j}[n-1] \\ \left(\underline{\gamma}_{1j} \odot \underline{f}_{1j}[n+1]\right) \mathrm{a}_{1j}[n+1] \end{bmatrix}}^{\text{ISI term}} \\ &+ \overbrace{\sum_{i=2}^{M} \sum_{j=1}^{\mathcal{N}_{sc}} \left[\mathbb{H}_{ij}^{\text{comb}}, \mathbb{H}_{ij}\right] \begin{bmatrix} \left(\underline{\gamma}_{ij} \odot \underline{f}_{ij}[n-1]\right) \mathrm{a}_{ij}[n-1] \\ \left(\underline{\gamma}_{ij} \odot \underline{f}_{ij}[n+1]\right) \mathrm{a}_{ij}[n+1] \\ \left(\underline{\gamma}_{ij} \odot \underline{f}_{ij}[n]\right) \mathrm{a}_{ij}[n] \end{bmatrix}}^{\text{MAI term}} \\ &+ \overbrace{\underline{\mathrm{n}}[n]}^{\text{noise}}. \end{aligned} \tag{5.23}$$

Based on Eq. 5.23, the theoretical covariance matrix of the received signal $\mathbb{R}_{xx} \in \mathcal{C}^{2N\mathcal{N}_c\mathcal{N}_{sc} \times 2N\mathcal{N}_c\mathcal{N}_{sc}}$ can be written as

$$\begin{aligned}\mathbb{R}_{xx} &= \mathcal{E}\{\underline{x}[n]\underline{x}^H[n]\} \\ &= \overbrace{\sum_{j=1}^{\mathcal{N}_{sc}} \mathbb{H}_{1j}\mathbb{G}_{1j}\mathbb{H}_{1j}^H}^{\text{Desired term}} + \overbrace{\sum_{j=1}^{\mathcal{N}_{sc}} \mathbb{H}_{1j}^{\text{comb}} \left(\mathbb{I}_2 \otimes \mathbb{G}_{1j}\right) \left(\mathbb{H}_{1j}^{\text{comb}}\right)^H}^{\triangleq \mathbb{R}_{\text{ISI}}} \\ &\quad + \overbrace{\sum_{i=2}^{M} \sum_{j=1}^{\mathcal{N}_{sc}} \left[\mathbb{H}_{ij}^{\text{comb}}, \mathbb{H}_{ij}\right] \left(\mathbb{I}_3 \otimes \mathbb{G}_{ij}\right) \left[\mathbb{H}_{ij}^{\text{comb}}, \mathbb{H}_{ij}\right]^H}^{\triangleq \mathbb{R}_{\text{MAI}}} \\ &\quad + \overbrace{\sigma_{\mathrm{n}}^2 \mathbb{I}_{2N\mathcal{N}_c\mathcal{N}_{sc}}}^{\triangleq \mathbb{R}_{\text{nn}}}, \end{aligned} \tag{5.24}$$

where $\mathbb{G}_{ij} \in \mathcal{C}^{K_i \times K_i}$ represents the multipath power gain matrix given

by

$$\begin{aligned}\mathbb{G}_{ij} &= \mathcal{E}\left\{\left(\underline{\gamma}_{ij} \odot \underline{f}_{ij}[n]\right) \mathrm{a}_{ij}[n]\mathrm{a}_{ij}^{*}[n] \left(\underline{\gamma}_{ij} \odot \underline{f}_{ij}[n]\right)^{H}\right\} \\ &= \mathrm{diag}\left\{\underline{\gamma}_{ij} \odot \underline{\gamma}_{ij}^{*}\right\} \odot \mathcal{E}\left\{\underline{f}_{ij}[n]\underline{f}_{ij}^{H}[n]\right\} \\ &= \mathrm{diag}\left\{\underline{\gamma}_{ij} \odot \underline{\gamma}_{ij}^{*}\right\}, \end{aligned} \tag{5.25}$$

since $\mathcal{E}\left\{\mathrm{a}_{ij}[n]\mathrm{a}_{ij}^{*}[n]\right\} = 1$ and $\mathcal{E}\left\{\underline{f}_{ij}[n]\underline{f}_{ij}^{H}[n]\right\} = \mathbb{I}_{K_i}$. Note that, with the L spatiotemporal snapshots shown in Fig. 5.3, the practical covariance matrix corresponding to the theoretical one given by Eq. 5.24, can be obtained as follows

$$\mathbb{R}_{xx} = \frac{1}{L}\Big[\underline{x}\,[1], \ldots, \underline{x}\,[L]\Big]\Big[\underline{x}\,[1], \ldots, \underline{x}\,[L]\Big]^{H}. \tag{5.26}$$

5.2.5 Fundamental Performance Bounds

As stated in [46], the estimation performance of an arrayed system depends on the radius of the uncertainty sphere centred at the true value on the manifold. This uncertainty sphere arises due to the finite sampling effect characterised by the number of snapshots L and the SNR.

In the case of the Cramer-Rao bound (CRB), which gives a theoretical lower bound on the variance of the estimation error of the azimuth (θ) for a source, for space-only systems, it has been shown in [46] that

$$\mathrm{CRB}_{\text{space-only}}\,[\theta] = \frac{1}{2\,(\mathrm{SNR} \times L)\,\dot{s}^{2}\,(\theta)}. \tag{5.27}$$

Here $\dot{s}\,(\theta) = \frac{\partial s}{\partial \theta}$ denotes the rate of change of the arc length s of the array manifold and it is a function of the array geometry. For instance for linear arrays of N sensors, $\dot{s}\,(\theta) = \pi \left\|\underline{r}_{x}\right\| \sin\theta$.

However, to evaluate the CRB for the spatiotemporal system employed in this paper, Eq. 5.27 needs to be extended to incorporate the Doppler-STAR manifold vector. The rate of change of the arc length of the extended manifold $\dot{s}_{\mathcal{H}}(\theta)$ has been derived in [106] as

$$\dot{s}_{\mathcal{H}}(\theta) = \sqrt{\sigma_{\mathbb{A}}^2 \dot{s}^2(\theta) + \sigma_{\dot{\mathbb{A}}}^2 N}, \tag{5.28}$$

where $\sigma_{\mathbb{A}}^2$ and $\sigma_{\dot{\mathbb{A}}}^2$ are defined as follows

$$\sigma_{\mathbb{A}}^2 = \frac{\mathrm{Tr}\left\{\mathbb{A}^H \mathbb{A}\right\}}{N} \text{ and } \sigma_{\dot{\mathbb{A}}}^2 = \frac{\mathrm{Tr}\left\{\dot{\mathbb{A}}^H \dot{\mathbb{A}}\right\}}{N}. \tag{5.29}$$

Using Eq. 5.13 in conjunction with Eq. 5.29, the following can be obtained

$$\sigma_{\mathbb{A}}^2 = \mathcal{N}_c \mathcal{N}_{sc} \text{ and } \sigma_{\dot{\mathbb{A}}}^2 = 0 \overset{\text{Eq. 5.28}}{\Longrightarrow} \dot{s}_{\mathcal{H}}(\theta) = \sqrt{\mathcal{N}_c \mathcal{N}_{sc}}\dot{s}(\theta). \tag{5.30}$$

Using this in conjunction with Eq. 5.27, we can derive the CRB of the proposed spatiotemporal system as follows

$$\boxed{\mathrm{CRB}_{\text{Doppler-STAR}}[\theta] = \tfrac{1}{\mathcal{N}_c \mathcal{N}_{sc}} \mathrm{CRB}_{\text{space-only}}[\theta].} \tag{5.31}$$

This illustrates that, for the same number of antennas, the proposed spatiotemporal system outperforms the corresponding space-only system in terms of the estimation error. Remember that θ is now one of the unknown wireless channel parameters which should be estimated and this will be presented in the following section.

5.3 Proposed Spatiotemporal Beamformer Design

Based on the 3D data cube shown in Fig. 5.3 and the spatiotemporal snapshot $\underline{x}[n]$ modelled by Eq. 5.23, in this section, a novel

spatiotemporal beamformer is proposed for the millimetre wave communication system described previously. As shown in Fig. 5.5, this beamformer consists of a Doppler-spatiotemporal array (STAR) subspace receiver utilising the estimated parameters, denoted by $\hat{(\cdot)}$, from a novel channel estimator. The design of these blocks is discussed in the next few sections. Without any loss of generality, the first user is considered to be the desired user and for notational convenience the subscript i is dropped.

Based on Eqs. 5.23 and 5.26, the following parameters of interest of all the paths of the desired user across all subcarriers should be estimated: relative multipath delay, channel fading coefficients, Doppler frequency and DOA. Note that the estimation of Doppler frequency corresponding to a path and subcarrier is equivalent to the estimation of radial velocity for the same. As shown in the estimation block of Fig. 5.5, this complex estimation problem is broken down into smaller units of lower complexity. The search procedures are carried out in the baseband. Firstly, the delay and radial velocity are jointly estimated, followed by the estimation of DOA. Then, the combined contribution of the channel fading coefficients and transmit beamforming weights is estimated. These estimation procedures are blind and based on the assumptions of plane-wave propagation, known array geometry and fully calibrated arrays. The proposed framework utilises

(i) the extended array manifold which is a mathematical object embedded in a multidimensional complex space that entirely characterises an antenna array (of a given geometry) for the whole set of values in the parameter space,

(ii) the preprocessed received array data and in particular its second order statistics, which can provide a linear space spanned by the signals (signal subspace),

where the solution of the estimation problem is the intersection of the non-linear subspace-(i) and the linear subspace-(ii). This intersection can be found by the 2D and 1D search procedures to yield the K paths of the desired user as described in the Sections 5.3.1 and 5.3.2 below.

5.3.1 Joint Delay-Velocity Estimation

In this first stage of joint estimation of delay and velocity, since the DOA is unknown, the spatial dimension provided by the N antennas cannot be exploited. Hence, the subspace is reduced from $2N\mathcal{N}_c\mathcal{N}_{sc}$ to $2\mathcal{N}_c\mathcal{N}_{sc}$ dimensions by a simple rearrangement of the slices $\mathbb{X}[n]$ of the 3D data cube discussed in Section 5.2.4. Using the eigendecomposition of the covariance of the rearranged matrix $\left[\mathbb{X}^T[1],\ldots,\mathbb{X}^T[n],...,\mathbb{X}^T[L]\right] \in \mathcal{C}^{2\mathcal{N}_c\mathcal{N}_{sc}\times NL}$, the projection on the noise subspace $\mathbb{P}_{\mathrm{n}}$ is obtained. Note that, although the number of dimensions is reduced, increased number of snapshots are obtained due to the format of the rearrangement. The parameters corresponding to the desired user will lie in the signal subspace spanned by the temporal part of the manifold vector in Eq. 5.12, given by $\mathbb{J}^{l_k}\underline{\mathfrak{a}}_{kj} \odot \underline{\mathcal{F}}_{kj}$, containing the PN code of the desired user and a Doppler component. Using the fact that this subspace is orthogonal to the estimated noise subspace $\mathbb{P}_n$, the cost function $\xi(l_k, v_k)$ estimates the delay-velocity

jointly for the k-th multipath and can be defined as follows

$$\xi\left(l_k, v_k\right) = \frac{1}{\mathcal{N}_{sc}} \sum_{j=1}^{\mathcal{N}_{sc}} \frac{\left(\mathbb{J}^{l_k} \underline{\mathfrak{a}}_{kj} \odot \underline{\mathcal{F}}_{kj}\right)^H \left(\mathbb{J}^{l_k} \underline{\mathfrak{a}}_{kj} \odot \underline{\mathcal{F}}_{kj}\right)}{\left(\mathbb{J}^{l_k} \underline{\mathfrak{a}}_{kj} \odot \underline{\mathcal{F}}_{kj}\right)^H \mathbb{P}_{\mathrm{n}} \left(\mathbb{J}^{l_k} \underline{\mathfrak{a}}_{kj} \odot \underline{\mathcal{F}}_{kj}\right)}, \tag{5.32}$$

where

$$\begin{aligned} \underline{\mathcal{F}}_{kj} &\triangleq \underline{\mathcal{F}}_{kj}\left(v_k\right) \\ &= \exp\left(\mathrm{j}\left[0, 1, \ldots, 2\mathcal{N}_c\mathcal{N}_{sc} - 1\right]^T \frac{2\pi\left(F_c + F_j\right) v_k T_s}{c}\right). \end{aligned} \tag{5.33}$$

The peaks obtained from the 2-dimensional search using this cost function over a 2D grid (spanning the range of possible values of delay and velocity) yield the delay and velocity values corresponding to the multipaths of the desired user. The number of evaluations is not a function of the number of antennas but depends purely on the chosen 2D grid. Furthermore, the evaluations are independent from each other and can be done in parallel. Note that, for the multicarrier system, a combined estimate of all subcarriers is evaluated which can help combat frequency selective fades in the mm-wave channel.

5.3.2 DOA Estimation

The design of this cost function follows the logic stated previously that the intersection of the noise subspace spanned by $\mathbb{P}_{\mathrm{n}}$ and the extended Doppler-STAR manifold object will yield the set of all Doppler-STAR manifold vectors $\underline{\mathfrak{h}}_j$ (see Eq. 5.12) of the desired user's paths. Hence, for $k = 1, ..., K$ pairs of estimated $\left(\widehat{l}_k, \widehat{v}_k\right)$, a 1D search is carried out over the space-time cost function given by

$$\xi\left(\theta_{\widehat{l}_k, \widehat{v}_k}\right) = \frac{1}{\mathcal{N}_{sc}} \sum_{j=1}^{\mathcal{N}_{sc}} \frac{\underline{\mathfrak{h}}_j^H\left(\theta_{\widehat{l}_k, \widehat{v}_k}\right) \underline{\mathfrak{h}}_j\left(\theta_{\widehat{l}_k, \widehat{v}_k}\right)}{\underline{\mathfrak{h}}_j^H\left(\theta_{\widehat{l}_k, \widehat{v}_k}\right) \mathbb{P}_{\mathrm{n}} \underline{\mathfrak{h}}_j\left(\theta_{\widehat{l}_k, \widehat{v}_k}\right)}, \tag{5.34}$$

where $\mathbb{P}_{\mathrm{n}}$ represents the projection on the noise subspace obtained from the eigendecomposition of the covariance matrix $\mathbb{R}_{xx}$.

5.3.3 Combined Fading Coefficient Estimation

Post estimating the delay, radial velocity and DOA, the residual combined parameter γ_{kj} to be estimated consists of the complex path fading coefficient and the transmit beamforming gain for the j-th subcarrier and k-th path. In this section, a near-far algorithm to estimate the amplitude and phase of γ_{kj} is described. The steps in the algorithm are as follows:

1. The subspace $\mathbb{R}_{kj,\mathrm{un}}$ consisting of MAI, noise and the other $K-1$ paths of the desired user is constructed by subtracting the effects of $\hat{\underline{\mathfrak{h}}}_{kj}$ (estimated in Sections 5.3.1 and 5.3.2) from the data covariance matrix

$$\mathbb{R}_{kj,\mathrm{un}} = \mathbb{R}_{xx} - \|\hat{\gamma}_{kj}\|^2 \hat{\underline{\mathfrak{h}}}_{kj} \hat{\underline{\mathfrak{h}}}_{kj}^H, \tag{5.35}$$

where $\|\hat{\gamma}_{kj}\|$ can be estimated using the following cost function inspired from [107]

$$\|\hat{\gamma}_{kj}\| = \arg\min_{\|\gamma\|} \xi_{kj}\left(\|\gamma\|\right), \tag{5.36}$$

where

$$\xi_{kj}\left(\|\gamma\|\right) = \sum_{\substack{m=1 \\ \mathrm{eig}_m>0}}^{2N\mathcal{N}_c\mathcal{N}_{sc}} \left(1 + \mathrm{eig}_m\left(\mathbb{R}_{kj}\left(\|\gamma\|\right)\right)\right) + 10\log_{10}\left(\sum_{\substack{m=1 \\ \mathrm{eig}_m<0}}^{2N\mathcal{N}_c\mathcal{N}_{sc}} \left|\mathrm{eig}_m\left(\mathbb{R}_{kj}\left(\|\gamma\|\right)\right)\right|\right), \tag{5.37}$$

with

$$\mathbb{R}_{kj}\left(\|\gamma\|\right) = \mathbb{R}_{xx} - \mathrm{eig}_{\min}\left(\mathbb{R}_{xx}\right) - \|\gamma\|_{kj}^2 \hat{\underline{\mathfrak{h}}}_{kj} \hat{\underline{\mathfrak{h}}}_{kj}^H. \tag{5.38}$$

(Note that the aforementioned 1D cost function of Eq. 5.37 is searched for the amplitude $\|\gamma\|$ that reduces the rank of the received signal covariance matrix $\mathbb{R}_{xx}$ by one.) By partitioning the space spanned by the columns of $\mathbb{R}_{kj,\text{un}}$ into "unwanted" signal subspace and "noise" subspace, the projection operator $\mathbb{P}_{kj,\text{un}}$ is formed using the eigenvectors corresponding to the "unwanted signal". This, in turn, can be utilised to construct $\mathbb{P}^{\perp}_{kj,\text{un}}$ to isolate the j-th subcarrier and k-th path of the desired user and remove the unwanted signals, that is

$$\mathbb{P}^{\perp}_{kj,\text{un}} = \mathbb{I}_{2N\mathcal{N}_c\mathcal{N}_{sc}} - \mathbb{P}_{kj,\text{un}}. \tag{5.39}$$

2. By exploiting the noise tolerance of the modulation and utilising all the available symbols in the observation interval of L snapshots, the phase of $\hat{\gamma}_{kj}$ can be estimated as follows

$$\angle\hat{\gamma}_{kj} = \left\{ \frac{1}{L} \sum_{n=1}^{L} \left\{ \angle \left(f^{*}_{kj}[n] \hat{\underline{\mathfrak{h}}}^{H}_{kj} \mathbb{P}^{\perp}_{kj,\text{un}} \underline{x}[n] \right) - \hat{\gamma}_{kj,\text{gu}} \right\} \text{mod}\psi - \psi_0 \right\} + \angle\hat{\gamma}_{kj,\text{gu}}, \tag{5.40}$$

where $\angle\hat{\gamma}_{kj,\text{gu}}$ is an initial guess of $\angle\hat{\gamma}_{kj}$ obtained with the help of $\mathbb{P}^{\perp}_{kj,\text{un}}$ as below

$$\angle\hat{\gamma}_{kj,\text{gu}} = \angle \text{a}^{*}_{j}[1] \hat{\underline{\mathfrak{h}}}^{H}_{kj} \left(\mathbb{P}^{\perp}_{kj,\text{un}} \underline{x}[1] \right). \tag{5.41}$$

Here $\text{a}_j[1]$ is the first symbol on the j-th subcarrier of every observation interval which is assumed to be the header (i.e. known). There are two important points to be noted here. Firstly, the role of $\mathbb{P}^{\perp}_{kj,\text{un}}$ is to make the procedure near-far resistant. Secondly, after suppressing the interference, two levels of noise suppression are utilised. First level of obtaining $\angle\hat{\gamma}_{kj,\text{gu}}$

relies on the inherent noise tolerance of the modulation while the second level uses a maximum likelihood (ML) averaging approach to obtain an improved estimate of the phase. Note that this is under the assumption that the phase deviation introduced by the noise is within $\pm\psi$ where ψ is the minimum phase difference between two constellation points and ψ_0 is the initial modulation angle in the chosen modulation scheme.

Please note that the above proposed near-far resistant estimation procedure for the phase of the desired parameter γ is one of the novelties of this paper.

5.3.4 Design of the Rx Spatiotemporal Beamformer Weights

In this subsection, the estimated channel parameters are employed to construct spatiotemporal beamforming weights to steer very high gain towards the directions of interest. We present a novel single-user Doppler-STAR-subspace receiver that explicitly cancels ISI and MAI and utilises the multipath effects in a frequency selective channel constructively. The steps to build these weights for the j-th subcarrier are as follows:

1. As a first step, the unwanted subspace (or the subspace perpendicular to the j-th subcarrier) $\widehat{\mathbb{R}}_{\text{unwanted}}$ is required to be estimated. Towards this, the contribution of the desired user to the received signal covariance matrix, namely $\widehat{\mathbb{R}}_{\text{des}}$, has to be removed from the received signal covariance matrix $\mathbb{R}_{xx}$. However, in order to receive the data on the j-th subcarrier, the contribution of the other subcarriers is required to be suppressed from

$\widehat{\mathbb{R}}_{\text{des}}$ and made a part of the estimated interference subspace given by

$$\widehat{\mathbb{R}}_{\text{unwanted}} = \mathbb{R}_{xx} - \widehat{\mathbb{H}}_j \widehat{\mathbb{G}}_j \widehat{\mathbb{H}}_j^H. \tag{5.42}$$

2. By performing the eigendecomposition of the estimated $\widehat{\mathbb{R}}_{\text{unwanted}}$, the matrix $\mathbb{E}_{\text{s}}$ whose columns contain the eigenvectors spanning the corresponding unwanted signal subspace can be obtained. Using this matrix $\mathbb{E}_{\text{s}}$, a projection operator orthogonal to the MAI, ISI and other subcarriers may be built as follows

$$\mathbb{P}_{j,\text{unwanted}}^{\perp} = \mathbb{I}_{2N\mathcal{N}_c\mathcal{N}_{sc}} - \mathbb{E}_{\text{s}} \left(\mathbb{E}_{\text{s}}^H \mathbb{E}_{\text{s}}\right)^{-1} \mathbb{E}_{\text{s}}^H. \tag{5.43}$$

3. The projection operator from step 2 is used to form the Doppler-STAR-subspace weights as

$$\underline{w}_{j,\text{sub}} = \mathbb{P}_{j,\text{unwanted}}^{\perp} \widehat{\mathbb{H}}_j \left(\widehat{\mathbb{H}}_j^H \mathbb{P}_{j,\text{unwanted}}^{\perp} \widehat{\mathbb{H}}_j\right)^{-1} \underline{\hat{\gamma}}_j. \tag{5.44}$$

An estimate of the transmitted symbol vector $\underline{\hat{\text{a}}}\,[n]$ (point B in Fig. 5.2) is formed as

$$\underline{\hat{\text{a}}}\,[n] = \mathbb{W}^H \underline{x}\,[n]\,, \tag{5.45}$$

with $\mathbb{W}$ being the concatenation of the Doppler-STAR-subspace weights designed for all the subcarriers that is

$$\mathbb{W} = [\underline{w}_1, \ldots, \underline{w}_{\mathcal{N}_{sc}}] \in \mathcal{C}^{2N\mathcal{N}_c\mathcal{N}_{sc} \times \mathcal{N}_{sc}}. \tag{5.46}$$

For the sake of completeness, the performance of this receiver is compared to two other extensively used receivers: (a) single-user Doppler-STAR-RAKE receiver and (b) multiuser Doppler-STAR-decorrelating receiver. The weights for the Doppler-STAR-RAKE receiver are given as

$$\underline{w}_{j,\text{RAKE}} = \widehat{\mathbb{H}}_j \underline{\hat{\gamma}}_j. \tag{5.47}$$

The multiuser Doppler-STAR-decorrelating receiver (zero-forcing receiver) exploits the knowledge of the entire channel (i.e. all users) given by

$$\mathbb{H} = \left[\mathbb{H}_{11}^{\text{comb}}, \mathbb{H}_{11}, \ldots, \mathbb{H}_{M\mathcal{N}_{sc}}^{\text{comb}}, \mathbb{H}_{M\mathcal{N}_{sc}}\right], \tag{5.48}$$

where $\mathbb{H}_{ij}$ represents the contribution of the j-th subcarrier of the i-th user. The version of this receiver introduced in [93] as been employed here, expressed as

$$\underline{w}_{j,\text{dec}} = \text{col}_{3jK_1-K_1+1:3jK_1}\left\{\left[\mathbb{H}\left(\mathbb{H}^H\mathbb{H}\right)^{-1}\right]\right\}\widehat{\underline{\gamma}}_j, \tag{5.49}$$

where the notation $\text{col}_{3jK_1-K_1+1:3jK_1}$ has been used to indicate that the $(3jK_1 - K_1 + 1)$-th to $(3jK_1)$-th columns are extracted.

5.4 Computer Simulation Studies

To evaluate the performance of the proposed spatiotemporal beamformer and the associated parameter estimator, computer simulation studies have been performed. Without any loss of generality, both the Tx and Rx antenna arrays are considered to be uniform circular arrays (UCA) of 16 and 9 elements respectively lying in the (x, y) plane. The Cartesian coordinates of the elements of these two arrays are indicated in $\left(\frac{\lambda}{2}\text{ units}\right)$.

The simulation parameters have been chosen to match the environment of the future 5G system. Empirical studies indicate that at millimetre wave frequencies, due to high path loss and scattering, only a few significant multipaths may be present with the LOS path being the dominant one. Hence, only 2 or 3 multipaths per user are considered in the simulation. Table 5.1 shows the system employed for Monte-Carlo simulations. The parameters follow a uni-

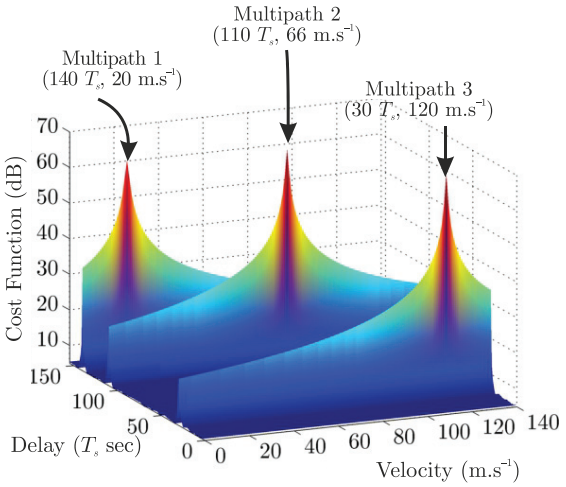
Table 5.1: Simulation Parameters

Parameter	Value	Parameter	Value
F_c	20 GHz	T_s	0.1μs
$\bar{N}$	16	N	9
$\mathcal{N}_c$	15 chips	$\mathcal{N}_{sc}$	5 subcarriers
M	4 users	K	2 paths per user

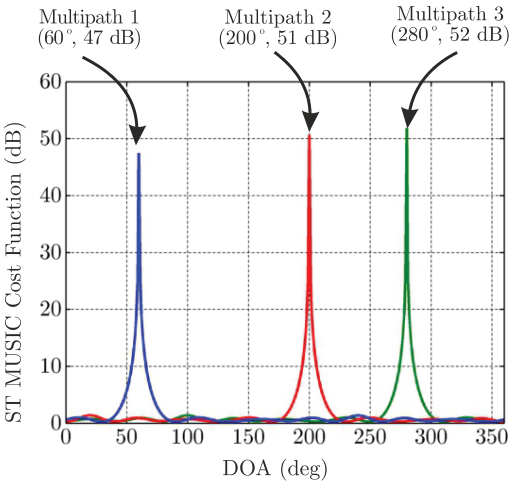
form distribution in their respective intervals i.e., the DOD and DOA between 0 and 360 degrees, the delays between 0 to $\mathcal{N}_c\mathcal{N}_{sc}T_s - 1$, the Doppler between 0 and 10 kHz and the complex path coefficients follow a uniform phase distribution between 0 and 360 degrees and the gain follows a Rayleigh distribution. Also, for the sake of simplicity, a steering vector towards the dominant multipath is utilised as the transmit weight vector per user.

5.4.1 Channel Estimation Studies

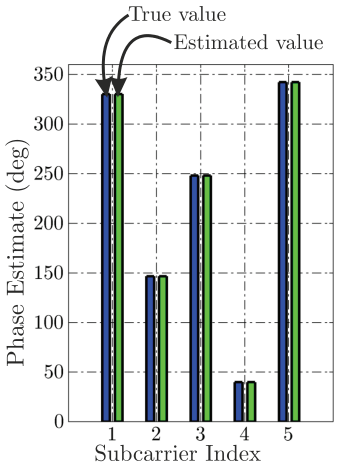
In this section, the channel estimator block, illustrated in Fig. 5.5, is evaluated in terms of its performance in the presence of interference and noise. Consider one desired user operating in the presence of 4 co-channel interfering users in a frequency selective channel with 3 paths per user. Let us assume an observation interval of 200 channel symbols ($L = 200$) during which the channel parameters of the desired user to be estimated are ($140\ T_s, 20\ \text{m.s}^{-1}, 60°$), ($110\ T_s, 66\ \text{m.s}^{-1}, 200°$) and ($30\ T_s, 120\ \text{m.s}^{-1}, 280°$). All users are assumed equipowered with an input SNR of 20dB and SNR is defined as the power of the transmitted signal over the power of the noise. Received signal data generated using random transmitted signal data for the above environment corresponding to $L = 200$ was utilised to obtain the results of the proposed approach as shown in Fig. 5.6.



(a) Estimation of the delay-velocity for the three multipaths of the desired user.



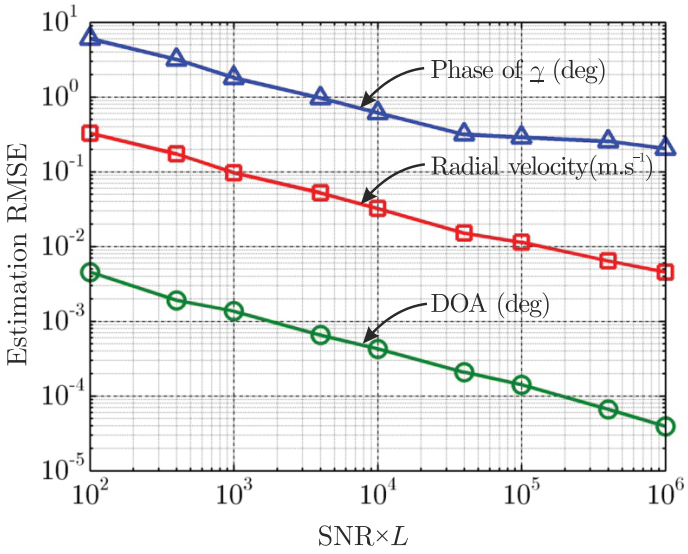
(b) Estimation of the DOA for the three multipaths of the desired user.



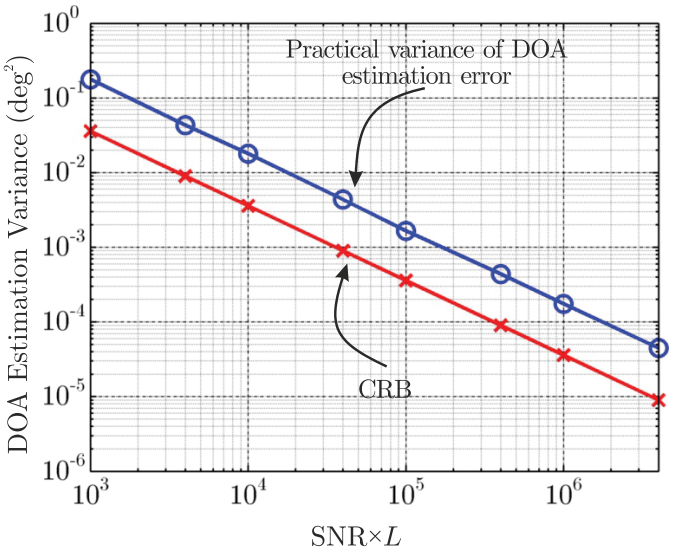
(c) Phase estimate of the elements of the parameter vector $\underline{\gamma}$ for one multipath over all subcarriers.

Figure 5.6: Desired user's channel parameter estimation using a circular array of 9 elements operating in the presence of 4 equipowered users with $\text{SNR}_{\text{in}} = 20$ dB with $\mathcal{N}_c = 31$ and $\mathcal{N}_{sc} = 5$ (a) Joint delay-velocity estimation (b) DOA estimation (c) Phase estimation of $\underline{\gamma}$.

An important parameter in subspace based approaches is the number of snapshots L used in the estimation procedure. As the value of L increases, the practical covariance matrix provides a better approximation of the theoretical covariance matrix. Figure 5.7a shows the root mean square error (RMSE) as a function of SNR$\times L$ averaged over 100 trials for all the subspace-based approaches in the



(a) RMSE estimation error of the radial velocity, DOA and phase of $\underline{\gamma}$.



(b) CRB and practical variance of DOA estimation error of the proposed algorithm.

Figure 5.7: Evaluation of the proposed spatiotemporal estimator algorithm.

estimator for a fixed value of L at 200 and equal powers for all users. The SNR was varied from 5 to 30 dB for the simulation[6].

The error in the estimation of the delay is not shown since it is zero through the whole range of SNR×L. The results indicating a

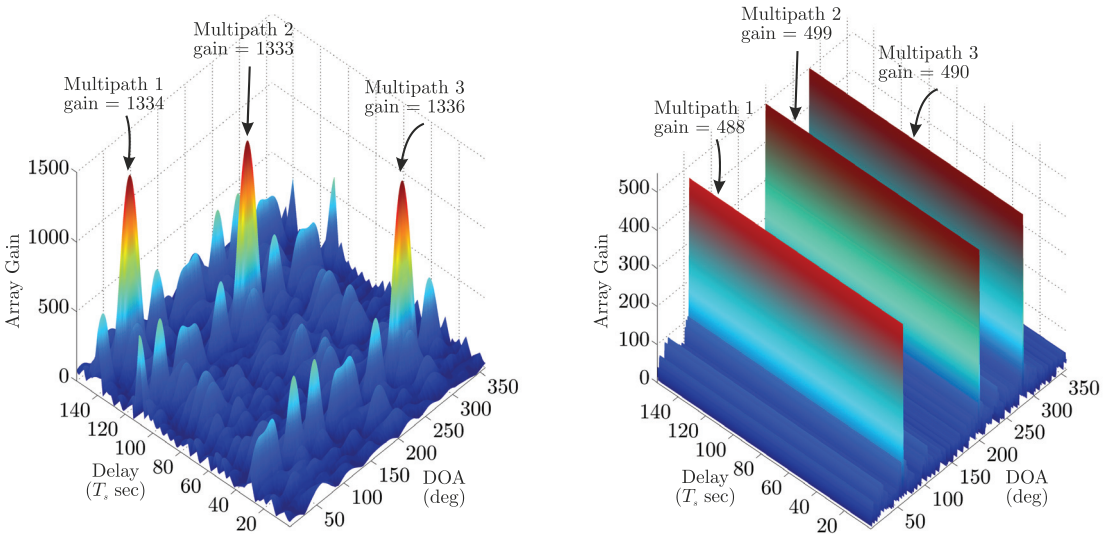
[6]Please note that the delay estimation RMSE was not displayed because the estimation error was non-existent for this range of SNR x L.

decrease in RMSE with increasing values of SNR$\times L$ is in-line with the performance bounds presented in Section 5.2.5. A higher value of L may yield better means to combat lower SNR at the cost of the assumption that the channel remains constant over this longer interval of time. The CRB for the DOA parameter for the proposed spatiotemporal system was presented in Section 5.2.5. Figure 5.7b presents an evaluation of the proposed algorithm against this theoretical result in terms of the variance of the DOA estimation error. It can be observed that the performance of the proposed system approaches the theoretical bound closely.

5.4.2 Reception Studies

Performance and results obtained at the reception stage, illustrated in Fig. 5.5, are presented in this subsection. Due to the utilisation of space and time dimensions, the antenna array sets high gains towards the three paths of the desired user and combines them to exploit multipath diversity. For a system operating with $\mathcal{N}_c = 31$ chips and $\mathcal{N}_{sc} = 5$ subcarriers, Fig. 5.8a illustrates the beampattern[7] of the proposed Doppler-STAR-subspace receiver. It can be observed that the proposed spatiotemporal beamformer provides a maximum gain of 1395 ($N\mathcal{N}_c\mathcal{N}_{sc}$) as compared to a space-only beamformer that would yield a maximum array gain of 9 (N). Figure 5.8b shows the performance of a massive MIMO beamformer (space-only) consisting of 500 antennas. It is clear from Figs. 5.8a and 5.8b that, although the spatiotemporal beamformer utilises a smaller number of antennas (only 9) than the massive MIMO beamformer, it achieves a much

[7]Here, for the sake of the simplicity, the Doppler frequency of the multipaths of the first user are equal.



(a) Beampattern of a Doppler-STAR-subspace receiver consisting of 9 antenna elements

(b) Beampattern of a massive MIMO subspace receiver consisting of 500 antenna elements

Figure 5.8: Comparison of the beampatterns of the proposed Doppler-STAR approach and a spatial-only massive MIMO system.

higher gain making it suitable to address the issues of high path loss in 5G mm-wave communications.

Note also that the spatiotemporal approach can be used with any array geometry containing any number of sensors. Thus, if it is employed in conjunction with a massive Rx antenna array of 500 antennas, the gains would be massive as this is shown in Fig. 5.9.

Consider again the simulation environment of Fig. 5.8, but this time let us assume that two out of the three paths of the desired user are co-directional (DOA = 280°). Consider also that the DOA of one of the "unwanted" is 280°. Figure 5.10 shows the array gain pattern of the proposed beamformer of 9 antennas and a traditional massive MIMO of 500 antennas. Figure 5.10a shows that the proposed Doppler-STAR-subspace receiver has 3 mainlobes with very high gains even for the two co-directional paths (2nd and 3rd) and suppresses the co-directional interference too. However, Fig. 5.10b

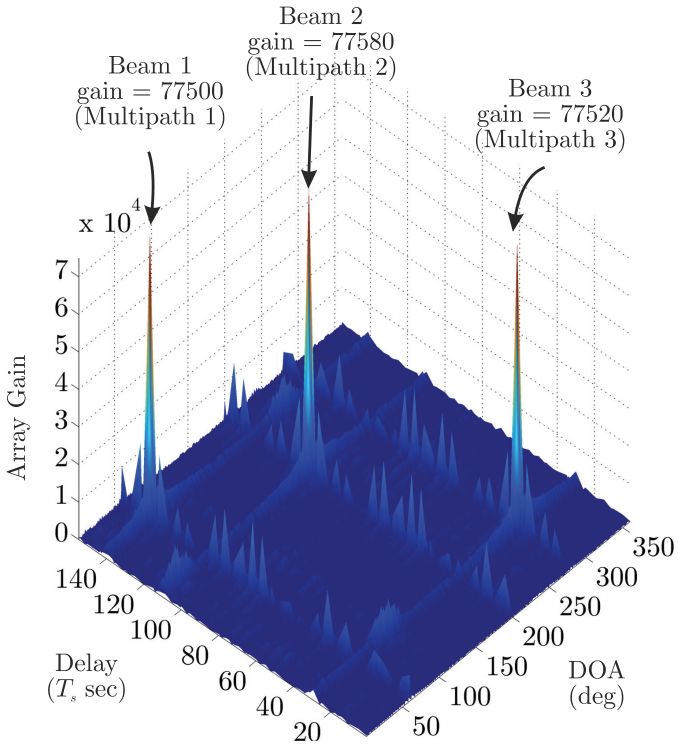
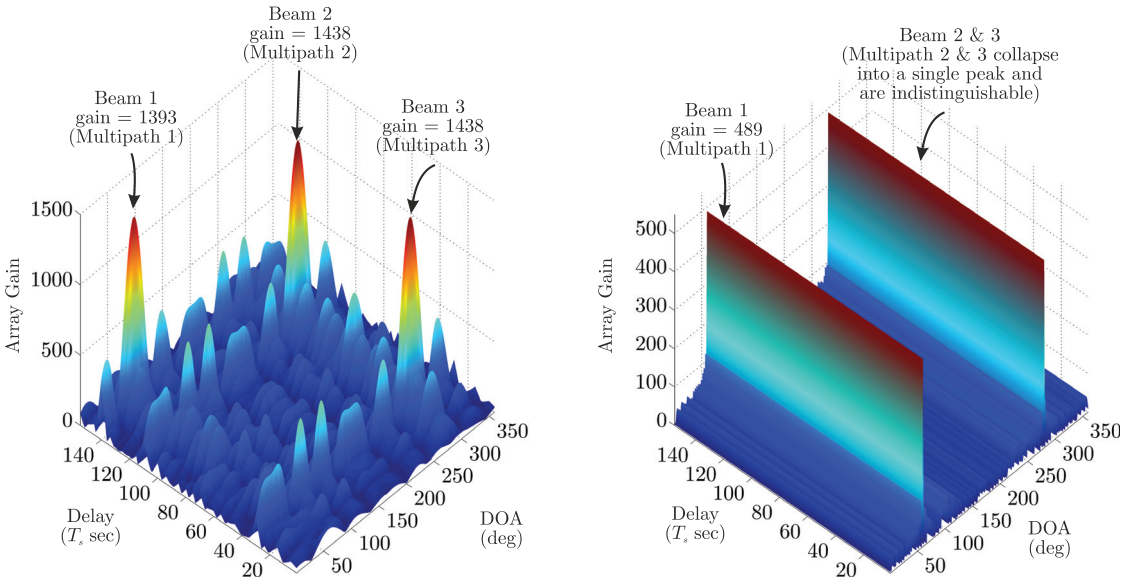


Figure 5.9: Beampattern of a spatiotemporal massive MIMO system with 500 antennas.

shows that a traditional massive MIMO beamformer cannot distinguish the 2nd and 3rd paths of the desired user (hence cannot exploit the multipath diversity) while also receives the 280° signal of the "unwanted" user with very high gain.

Figure 5.11 shows the performance of the proposed Doppler-STAR-subspace receiver (whose weights are given by Eq. 5.44) against other spatiotemporal receivers such as the Doppler-STAR-RAKE (Eq. 5.47), Doppler-STAR-decorrelating (Eq. 5.49) and traditional spatial-only massive MIMO (500 antennas) beamformer (enhanced with subspace set of weights and RAKE weights) in the presence of high interference and noise in terms of the output SNIR (SNIR_{out}). Note that, in these comparative studies, identical transmitter structures and transmitted data (from point-A to point-F in Fig. 5.2) are



(a) Beampattern of a Doppler-STAR-subspace receiver consisting of 9 antenna elements

(b) Beampattern of a massive MIMO subspace receiver consisting of 500 antenna elements

Figure 5.10: Comparison of the beampatterns of the proposed Doppler-STAR approach and a spatial-only massive MIMO system in a scenario where two multipaths arrive with the same DOA albeit different path delays

utilised for all receivers, generating signals of the same bandwidth. The $\mathrm{SNIR}_{j,\mathrm{out}}$ parameter is the level of interference in the beamformed signal of the j-th subcarrier and evaluates the performance of the reception system to mitigate interferences. The estimation of this parameter is based on $\mathbb{R}_{\mathrm{ISI}} + \mathbb{R}_{\mathrm{MAI}} + \mathbb{R}_{\mathrm{nn}}$, the covariance matrix of the undesired components of the received signal, and $\mathbb{R}_{\mathrm{des}}$, the covariance matrix of the desired signal

$$\mathrm{SNIR}_{j,\mathrm{out}} = \frac{\underline{w}_j^H \mathbb{R}_{\mathrm{des}} \underline{w}_j}{\underline{w}_j^H \left(\mathbb{R}_{\mathrm{ISI}} + \mathbb{R}_{\mathrm{MAI}} + \mathbb{R}_{\mathrm{nn}}\right) \underline{w}_j}. \tag{52}$$

By employing a Doppler-STAR-RAKE receiver that does not perform interference cancellation, the expression simplifies to

$$\mathrm{SNIR}_{j,\mathrm{out}} = N\mathcal{N}_c\mathcal{N}_{sc}\frac{P_s}{\sigma_{\mathrm{n}}^2 + P_{\mathrm{int}}}, \tag{53}$$

where P_{int} is the residual power contribution from MAI and ISI. By appropriately designing the Doppler-STAR-subspace weights, this

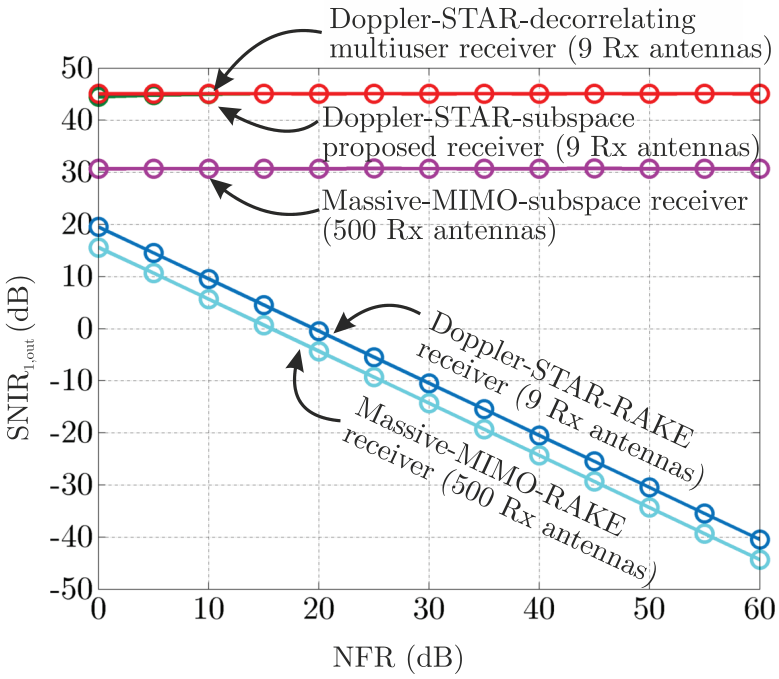


Figure 5.11: Comparative study of the performance of the proposed Doppler-STAR subspace receiver with other spatiotemporal and spatial-only receivers in terms of the NFR. (200 trials).

expression simplifies to

$$\mathrm{SNIR}_{j,\mathrm{out}} = N\mathcal{N}_c\mathcal{N}_{sc}\mathrm{SNR}_{\mathrm{in}}, \tag{54}$$

there is complete interference cancellation ($P_{\mathrm{int}} \to 0$). As expected, the $\mathrm{SNIR}_{1,\mathrm{out}}$ of the Doppler-STAR-RAKE receiver decreases dramatically. This illustrates that the Doppler-STAR-RAKE receiver is unable to provide appropriate levels of performance in the presence of interference. On the other hand, the Doppler-STAR-subspace receiver provides steady performance over a huge range of NFR from 0 to 60 dB by incorporating terms to explicitly suppress interference. Tolerance to the near-far problem is critical in cells with high user density. Also, the proposed Doppler-STAR-subspace receiver of 9 antennas outperforms the traditional massive MIMO

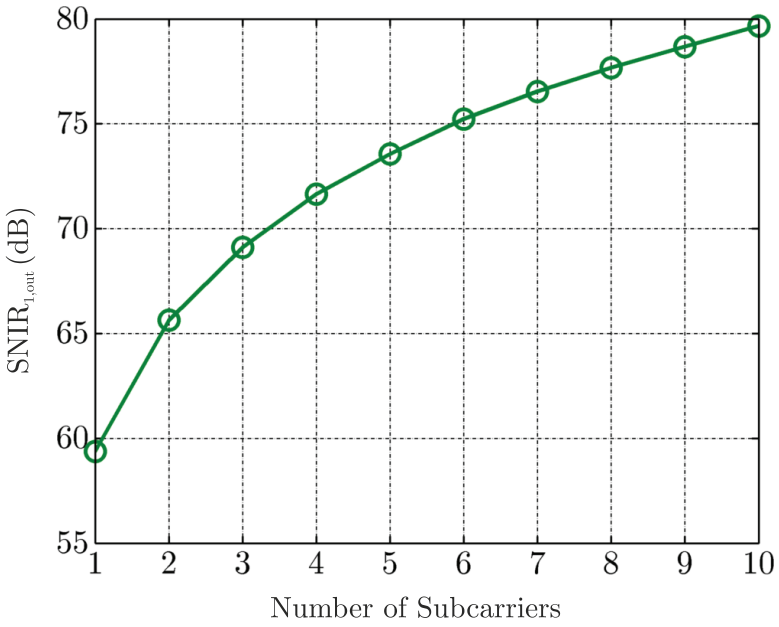


Figure 5.12: Performance of the Doppler-STAR-subspace receiver with varying number of subcarriers and data copy over subcarriers (50 trials).

beamformer of 500 antennas by 15 dB. Note that in the traditional massive MIMO beamformer, "subspace" and "RAKE" weights have been utilised which are in fact superior to the conventional massive MIMO beamformers such as "steering vector", "Weiner-Hopf" or "Capon" beamformers. As illustrated in Fig. 5.11, a performance very close to a multi-user receiver (Doppler-STAR-decorrelating receiver) is obtained without the channel knowledge of the interferers. The performance is also an indicator that at varying NFR levels, the channel estimation errors, if any, lie within the input error tolerance boundary of the receiver.

Figure 5.12 presents the performance of the proposed receiver with increasing number of subcarriers. Simulations show that the Doppler-STAR-subspace receiver exploits the frequency diversity to provide a higher SNIR_{out}. Also, degrees of freedom may be added by using a spatiotemporal approach at the transmitter side too. In this

paper, we do not exploit the overall Tx-Rx geometry by employing the concept of virtual MIMO. This may be a further extension of the current work.

5.5 Summary

In this chapter, a novel parametric channel model for mm-wave environments was proposed. Based on this model, a spatiotemporal beamformer performing channel estimation and reception has been designed. This beamformer was evaluated with varying levels of noise and interference. Simulation results indicate that the estimation and reception processes are highly tolerant to the near-far problem and yield a performance 15dB better than the traditional MIMO system of 500 antennas, exhibiting very high array gain and selectivity in space and time. This would enable the system to function without power control management algorithms. It is important to point out that the proposed receiver belongs to the family of spatiotemporal (space-time) receivers that exploit the spatiotemporal degrees of freedom and employs a beamformer that automatically combines multipath and suppresses co-channel interferences from other users to obtain an array gain similar to that of a massive MIMO system with a much smaller number of antennas. Finally, although the proposed approach is designed for the mm-wave frequency band, it is applicable to any radio frequency band. These characteristics of the presented system make it an attractive option for the next generation of mobile systems.

Chapter 6

Conclusions and Further Work

In this thesis antenna arrays and their use in modern wireless systems were investigated for combating co-channel interference.

The powerful model of the array manifold and the most important array geometry parameters were introduced first. The inner product between two array manifold vectors as a function of the manifold radii, the Cartan matrix and the arc length was derived. This new result is exact and does not rely on any approximation. These results laid the theoretical basis of the later chapters.

Subsequently, the importance of antenna array geometry for a variety of wireless communication tasks, such as detection, resolution and beamforming was characterised, by employing relevant performance criteria as figures-of-merit. It was concluded that the detection and resolution thresholds have strong dependencies with the number of antennas because it conditions the number of dimensions. On the reception part, new simulation studies, supported by theoretical results demonstrated that the $\mathrm{SNIR}_{\mathrm{out}}$ does not depend solely on the number of antennas, but also strongly on the array geometry. Thus, the square array of 40 antennas, for instance, has higher

SNIR_{out} and better energy efficiency than a "filled"-grid array with more (N =121) antennas.

A novel theoretical framework aimed at analysing the loss of capacity induced by interference was presented, and linked to the antenna array geometry. By combining array processing, differential geometry and wireless communication theories, it was demonstrated that the presence of interferers has a negative impact on the ability of the antenna array to receive the source of interest when their angular separation is below a threshold, and this is given by the capacity loss expression. Simulations studies illustrated that in highly dense systems, array manifold parameters, such as the arc length and principal curvature, play a significant role in the mitigation of interferences.

Finally, a novel parametric channel model for mm-wave environments was proposed. Based on this model, a spatiotemporal beamformer performing channel estimation and reception was designed. This beamformer was evaluated with varying levels of noise and interference. Simulation results indicated that the estimation and reception processes were highly tolerant to the near-far problem and yield a performance 15dB better than the traditional MIMO system of 500 antennas, exhibiting very high array gain and selectivity in space and time. This would enable the system to function without power control management algorithms. It is important to point out that the proposed receiver belongs to the family of spatiotemporal (space-time) receivers that exploit the spatiotemporal degrees of freedom and employs a beamformer that automatically combines multipath and suppresses co-channel interferences from other users

to obtain an array gain similar to that of a massive MIMO system with a much smaller number of antennas. These characteristics of the presented method make it an attractive option for the next generation of mobile networks.

6.1 List of Contributions

The following is the list of the novel contributions presented in this thesis.

1. Investigate the impact of array geometry on the performance of an antenna array systems (Chapter 3 and [3]). It is demonstrated that antenna arrays with the larger number of antennas do not necessarily deliver better performance, but the array geometry has to be considered instead.

2. Propose the concept of capacity loss as a new metric for characterising the loss of channel capacity induced by the presence of interferers (Chapter 4 and [1]). This new metric is expressed as a function of the array manifold parameters.

3. Define the capacity loss threshold, that is the angular separation required to achieve a particular capacity loss for a given antenna array geometry (Chapter 4).

4. Propose a novel spatiotemporal multiparameter channel estimator that is blind and estimates DOA, delay, radial velocity (Doppler frequency) and complex path gains of all paths of the desired user (Chapter 5 and [2]).

5. Propose a novel Rx spatiotemporal beamformer with extended degrees of freedom that cancel the MAI completely. The beamformer is a single-user receiver and does not require the knowledge of the interferers channels (Chapter 5 and [2]).

6.2 Suggestions for Further Work

The following list presents ideas and suggestions for future work, based on the research presented in this thesis:

- Chapter 3 illustrated the importance of array geometry for different tasks. These new results can be used with new array design algorithms that would design geometries optimised for a particular, or several performance criteria.
- It was demonstrated in Chapter 3 that the beamwidth and interference cancellation capabilities of an antenna array system depend on its geometry. The expression for inner products derived in Chapter 2, could be utilised to derive a beampattern function. Furthermore, this would unlock the design of antenna arrays that create beams with beamwidth following criteria of uniformity over the field of view/constraints of width towards particular directions of interest.
- Chapter 4 introduced the concept of capacity loss, which has to be studied further. The influence of the number of users and the multipath on the performance can be given more attention.
- It was illustrated that the capacity loss is a function of the antenna array geometry; hence one could look for an antenna array geometry that optimises this criterion.

- A novel spatiotemporal beamformer could improve the beamforming performance of Chapter 5 further by utilising transmit weights jointly with the receiving STAR weights, and hence introducing even more degrees of freedom.
- The degrees of freedom, and hence the number of users, could be extended further by including the polarisation parameters in the modelling of the array manifold.

References

[1] T. Gabillard, V. Sridhar, and A. Manikas, "Capacity loss and antenna array geometry," in *IEEE International Confenrence on Communications (ICC)*, May 2017.

[2] V. Sridhar, T. Gabillard, and A. Manikas, "Spatiotemporal-MIMO channel estimator and beamformer for 5G," *IEEE Transactions on Wireless Communications*, vol. 15, pp. 8025–8038, Sept. 2016.

[3] T. Gabillard, V. Sridhar, A. Akindoyin, and A. Manikas, "Comparative study of 2D grid antenna array geometries for massive array systems," in *IEEE Global Confenrence on Communication (GlobeCom)*, Dec. 2015.

[4] N. Bhushan, D. Malladi, R. Gilmore, D. Brenner, A. Damnjanovic, R. Sukhavasi, C. Patel, and S. Geirhofer, "Network densification: the dominant theme for wireless evolution into 5G," *IEEE Communications Magazine*, vol. 52, pp. 82–89, Feb. 2014.

[5] D. Tse, *Fundamentals of Wireless Communication*. Cambridge Press, 2005.

[6] T. L. Marzetta, "Massive MIMO: An introduction," *Bell Labs Technical Journal*, vol. 20, pp. 11–22, Mar. 2015.

[7] P.-D. Arapoglou, K. Liolis, M. Bertinelli, A. Panagopoulos, P. Cottis, and De Gaudenzi, "MIMO over satellite: A review," *IEEE Communications Surveys & Tutorials*, vol. 13, no. 1, pp. 27–51, 2011.

[8] H. Fenech, S. Amos, and T. Waterfield, "The role of array antennas in commercial telecommunication satellites," in *10th European Conference on Antennas and Propagation 2016*, pp. 1–4, Apr. 2016.

[9] S. Rougerie, G. Carrie, F. Vincent, L. Ries, and M. Monnerat, "A new multipath mitigation method for GNSS receivers based on an antenna array," *International Journal of Navigation and Observation*, vol. 2012, 2012.

[10] Y. B. Jung, S. Y. Eom, and S. I. Jeon, "Novel antenna system design for satellite mobile multimedia service," *IEEE Transactions on Vehicular Technology*, vol. 59, no. 9, pp. 4237–4247, 2010.

[11] J. Wu, Y. J. Cheng, and Y. Fan, "A wideband high-gain high-efficiency hybrid integrated plate array antenna for V-band inter-satellite links," *IEEE Transactions on Antennas and Propagation*, vol. 63, no. 4, pp. 1225–1233, 2015.

[12] K. Mak and A. Manikas, "A Superresolution Wide Null Beamformer for Undersampled Signal Reconstruction in SIMO

SAR," *IEEE Journal of Selected Topics in Signal Processing*, vol. 9, pp. 1548–1559, Dec. 2015.

[13] A. Van Ardenne, J. D. Bregman, W. A. Van Cappellen, G. W. Kant, and J. G. Bij De Vaate, "Extending the field of view with phased array techniques: Results of European SKA research," *Proceedings of the IEEE*, vol. 97, no. 8, pp. 1531–1542, 2009.

[14] G. Cortes-Medellin, G. Rajagopalan, P. Perillat, A. Vishwas, K. F. Warnick, B. D. Jeffs, M. Elmer, D. Carter, V. Asthana, and T. Webb, "Field of view characterization of Arecibo radio telescope with a phased array feed," in *IEEE International Symposium on Antennas and Propagation*, pp. 847–850, 2011.

[15] P. Felisberto and S. M. Jesus, "Towed-array beamforming during ship's manoeuvring," *IEE Proceedings-Radar, Sonar and Navigation*, vol. 143, no. 3, pp. 210–215, 1996.

[16] G. J. Foschini and M. J. Gans, "On limits of wireless communications in a fading environment when using multiple antennas," *Wireless Personal Communications*, vol. 6, pp. 311–335, 1998.

[17] G. Foschini, M. Gans, and J. Kahn, "Fading correlation and its effect on the capacity of multielement antenna systems," *IEEE Transactions on Communications*, vol. 48, pp. 502–513, Mar. 2000.

[18] R. Couillet and M. Debbah, *Random Matrix Methods for Wireless Communications*. Cambridge University Press, 2011.

[19] F. Rusek, D. Persson, B. K. Lau, E. G. Larsson, T. L. Marzetta, O. Edfors, and F. Tufvesson, "Scaling up MIMO : Opportuni-

ties and challenges with very large arrays," *IEEE Signal Processing Magazine*, vol. 30, pp. 40–60, Jan. 2013.

[20] T. L. Marzetta, "Noncooperative cellular wireless with unlimited numbers of base station antennas," *IEEE Transactions on Wireless Communications*, vol. 9, pp. 3590 – 3600, Nov. 2010.

[21] X. Gao, F. Tufvesson, and O. Edfors, "Massive MIMO channels - measurements and models," in *Asilomar Conference on Signals, Systems and Computers*, pp. 280–284, Nov. 2013.

[22] X. Gao, F. Tufvesson, and O. Edfors, "Massive MIMO channels - measurements and models," in *Asilomar Conference on Signals, Systems and Computers*, pp. 280–284, Nov. 2013.

[23] J. Flordelis, X. Gao, G. Dahman, F. Rusek, O. Edfors, and F. Tufvesson, "Spatial separation of closely-spaced users in measured massive multi-user MIMO channels," in *IEEE International Conference on Communications (ICC)*, pp. 1441–1446, June 2015.

[24] X. Gao, O. Edfors, F. Rusek, and F. Tufvesson, "Massive MIMO performance evaluation based on measured propagation data," *IEEE Transactions on Wireless Communications*, vol. 14, pp. 3899–3911, July 2015.

[25] X. Gao, O. Edfors, F. Tufvesson, and E. G. Larsson, "Massive MIMO in real propagation environments: Do all antennas contribute equally?," *IEEE Transactions on Communications*, vol. 63, pp. 3917–3928, Nov. 2015.

[26] A. Forenza, D. Love, and R. Heath, "Simplified spatial correlation models for clustered MIMO channels with different array configurations," *IEEE Transactions on Vehicular Technology*, vol. 56, pp. 1924–1934, July 2007.

[27] J. S. Kwak, J. G. Andrews, and A. Lozano, "MIMO capacity in correlated interference-limited channels," in *IEEE International Symposium on Information Theory*, pp. 106–110, IEEE, June 2007.

[28] D. Gore, R. Heath, and A. Paulraj, "Statistical antenna selection for spatial multiplexing systems," in *IEEE International Conference on Communications (ICC)*, vol. 1, May 2002.

[29] K. Pedersen, P. Mogensen, and B. Fleury, "A stochastic model of the temporal and azimuthal dispersion seen at the base station in outdoor propagation environments," *IEEE Transactions on Vehicular Technology*, vol. 49, pp. 437–447, Mar. 2000.

[30] Q. Spencer, B. Jeffs, M. Jensen, and A. Swindlehurst, "Modeling the statistical time and angle of arrival characteristics of an indoor multipath channel," *IEEE Journal on Selected Areas in Communications*, vol. 18, pp. 347–360, Mar. 2000.

[31] Q.-U.-A. Nadeem, A. Kammoun, M. Debbah, and M. Alouini, "A Generalized Spatial Correlation Model for 3D MIMO Channels based on the Fourier Coefficients of Power Spectrums," *IEEE Transactions on Signal Processing*, vol. 63, pp. 3671–3686, July 2015.

[32] J. Kermoal, L. Schumacher, K. Pedersen, P. Mogensen, and F. Frederiksen, "A stochastic MIMO radio channel model with experimental validation," *IEEE Journal on Selected Areas in Communications*, vol. 20, pp. 1211–1226, Aug. 2002.

[33] M. Ivrlac, W. Utschick, and J. Nossek, "Fading correlations in wireless MIMO communication systems," *IEEE Journal on Selected Areas in Communications*, vol. 21, pp. 819–828, June 2003.

[34] H. Özcelik, M. Herdin, W. Weichselberger, J. W. Wallace, and E. Bonek, "Deficiencies of 'Kronecker' MIMO radio channel model," *Electronics Letters*, vol. 39, no. 16, pp. 1209–1210, 2003.

[35] X. L. Wang, *Signal Processing in Arrayed MIMO Systems*. PhD thesis, Imperial College London, 2009.

[36] X. Mestre, J. Fonollosa, and A. Pages-Zamora, "Capacity of MIMO channels: asymptotic evaluation under correlated fading," *IEEE Journal on Selected Areas in Communications*, vol. 21, pp. 829–838, June 2003.

[37] H. Kim, G. Kim, W. Choi, and H. Park, "Asymptotic sum rate in spatially correlated two-cell channel with user scheduling," *IEEE Transactions on Vehicular Technology*, vol. 64, pp. 1235–1243, Mar. 2015.

[38] A. Burr, "Capacity bounds and estimates for the finite scatterers MIMO wireless channel," *IEEE Journal on Selected Areas in Communications*, vol. 21, pp. 812–818, June 2003.

[39] L. Hanlen and A. Grant, "Capacity analysis of correlated MIMO channels," *IEEE Transactions on Information Theory*, vol. 58, pp. 6773–6787, Nov. 2012.

[40] X. Wang and A. Manikas, "Joint linear precoder-decoder optimization over MIMO-CDMA multipath channels," in *International Symposium on Personal, Indoor and Mobile Radio Communications*, pp. 1–5, IEEE, Sept. 2007.

[41] V. Cadambe and S. Jafar, "Interference alignment and degrees of freedom of the k-user interference channel," *IEEE Transactions on Information Theory*, vol. 54, pp. 3425–3441, Aug. 2008.

[42] R. Muller, "A random matrix model of communication via antenna arrays," *IEEE Transactions on Information Theory*, vol. 48, no. 9, pp. 2495–2506, 2002.

[43] H. Xu, D. Chizhik, H. Huang, and R. Valenzuela, "A generalized space-time multiple-input multiple-output (MIMO) channel model," *IEEE Transactions on Wireless Communications*, vol. 3, pp. 966–975, May 2004.

[44] B. Fleury, "First- and second-order characterization of direction dispersion and space selectivity in the radio channel," *IEEE Transactions on Information Theory*, vol. 46, pp. 2027–2044, Sept. 2000.

[45] R. Ertel, P. Cardieri, K. Sowerby, T. Rappaport, and J. Reed, "Overview of spatial channel models for antenna array com-

munication systems," *IEEE Personal Communications*, vol. 5, no. 1, pp. 10–22, 1998.

[46] A. Manikas, *Differential Geometry in Array Processing*. Imperial College Press, 2004.

[47] W. C. Jakes, *Microwave Mobile Communications*. Piscataway, NJ: IEEE Press, 1974.

[48] G. Efstathopoulos and A. Manikas, "Existence and uniqueness of hyperhelical array manifold curves," *IEEE Journal of Selected Topics in Signal Processing*, vol. 7, pp. 625–633, Aug. 2013.

[49] H. Commin, *Spatiotemporal Arrayed MIMO Radar*. PhD thesis, Imperial College London, 2013.

[50] A. Sleiman and A. Manikas, "The impact of sensor positioning on the array manifold," *IEEE Transactions on Antennas and Propagation*, vol. 51, pp. 2227–2237, Sept. 2003.

[51] E. Björnson, E. G. Larsson, and M. Debbah, "Massive MIMO for maximal spectral efficiency: How many users and pilots should be allocated?," *IEEE Transactions on Wireless Communications*, vol. 15, no. 2, 2016.

[52] X. Huang, Y. J. Guo, and J. D. Bunton, "A hybrid adaptive antenna array," *IEEE Transactions on Wireless Communications*, vol. 9, pp. 1770–1779, May 2010.

[53] J. Nsenga, A. Bourdoux, and F. Horlin, "Mixed analog/digital beamforming for 60 GHz MIMO frequency selective channels,"

in *IEEE International Conference on Communications*, pp. 1–6, May 2010.

[54] U. Baysal and R. Moses, "On the geometry of isotropic arrays," *IEEE Transactions on Signal Processing*, vol. 51, pp. 1469–1478, June 2003.

[55] M. Gavish and A. Weiss, "Array geometry for ambiguity resolution in direction finding," *IEEE Transactions on Antennas and Propagation*, vol. 44, pp. 889–895, June 1996.

[56] J.-W. Liang and J. Paulraj, "On optimizing base station antenna array topology for coverage extension in cellular radio networks," in *IEEE Vehicular Technology Conference*, pp. 866–870, July 1995.

[57] J. S. Petko and D. H. Werner, "Interleaved ultrawideband antenna arrays based on optimized polyfractal tree structures," *IEEE Transactions on Antennas and Propagation*, vol. 57, pp. 2622–2632, Sept. 2009.

[58] A. Manikas, A. Alexiou, and H. R. Karimi, "Comparison of the ultimate direction-finding capabilities of a number of planar array geometries," *IEE Proceedings: Radar, Sonar and Navigation*, vol. 144, pp. 321–329, Dec. 1997.

[59] N. Dowlut and A. Manikas, "A polynomial rooting approach to super-resolution array design," *IEEE Transactions on Signal Processing*, vol. 48, pp. 1559–1569, June 2000.

[60] A. Manikas, H. Karimi, and I. Dacos, "Study of the detection and resolution capabilities of a one-dimensional array of sen-

sors by using differential geometry," *IEE Proceedings - Radar, Sonar and Navigation*, vol. 141, no. 2, pp. 83–92, 1994.

[61] A. Manikas and J. Ng, "Crossed-dipole arrays for asynchronous DS-CDMA systems," *IEEE Transactions on Antennas and Propagation*, vol. 52, pp. 122–131, Feb. 2004.

[62] H. Akaike, "A new look at the statistical model identification," *IEEE Transactions on Automated Control*, vol. 19, pp. 716–723, Dec. 1974.

[63] R. Liu, R. Ying, and G. Xu, "The ultimate capacity of MIMO channels and its realization," in *18th IEEE European Conference on Circuit Theory and Design*, pp. 695–698, Aug. 2007.

[64] C. H. Y. Eugene, K. Sakaguchi, and K. Araki, "Experimental and analytical investigation of MIMO channel capacity in an indoor line-of-sight (LOS) environment," in *15th IEEE International Symposium on Personal, Indoor and Mobile Radio Communications*, vol. 1, pp. 295–300, Sept. 2004.

[65] E. Bjornson, J. Hoydis, M. Kountouris, and M. Debbah, "Massive MIMO systems with non-ideal hardware: Energy efficiency, estimation, and capacity limits," *IEEE Transactions on Information Theory*, vol. 60, pp. 7112–7139, Sept. 2014.

[66] R. Blum, "MIMO capacity with interference," *IEEE Journal on Selected Areas in Communications*, vol. 21, pp. 793–801, June 2003.

[67] K. I. Ziri-Castro, W. G. Scanlon, and N. E. Evans, "Prediction of variation in MIMO channel capacity for the pop-

ulated indoor environment using a radar cross-section-based pedestrian model," *IEEE Transactions on Wireless Communications*, vol. 4, pp. 1186–1194, May 2005.

[68] A. A. Abouda, H. M. El-Sallabi, and S. G. Haggman, "Impact of antenna array geometry on MIMO channel eigenvalues," in *2005 IEEE 16th International Symposium on Personal, Indoor and Mobile Radio Communications*, vol. 1, pp. 568–572, Sept. 2005.

[69] P. Chandhar, D. Danev, and E. G. Larsson, "On ergodic rates and optimal array geometry in line-of-sight massive mimo," in *2016 IEEE 17th International Workshop on Signal Processing Advances in Wireless Communications (SPAWC)*, pp. 1–6, 2016.

[70] Y. Alem, Z. Khalid, and R. Kennedy, "3D spatial fading correlation for uniform angle of arrival distribution," *IEEE Communications Letters*, vol. 19, pp. 1073–1076, Mar. 2015.

[71] M. Choi, G. Grosskopf, D. Rohde, B. Kuhlow, G. Przyrembel, and H. Ehlers, "Experiments on DOA-estimation and beamforming for 60 GHz smart antennas," in *IEEE Semiannual Vehicular Technology Conference*, vol. 2, pp. 1041–1045, 2003.

[72] S. Affes, H. Hansen, and P. Mermelstein, "Interference subspace rejection: a framework for multiuser detection in wideband CDMA," *IEEE Journal on Selected Areas in Communications*, vol. 20, pp. 287–302, Feb. 2002.

[73] Y. Zhang and M. Amin, "Array processing for nonstationary interference suppression in DS/SS communications using subspace projection techniques," *IEEE Transactions on Signal Processing*, vol. 49, pp. 3005–3014, Dec. 2001.

[74] G. R. Maccartney Jr, J. Zhang, S. Nie, and T. S. Rappaport, "Path loss models for 5G millimeter wave propagation channels in urban microcells," in *IEEE Global Conference on Communications*, pp. 3948–3953, Dec. 2013.

[75] H. Yang, P. Smulders, and M. Herben, "Channel characteristics and transmission performance for various channel configurations at 60 GHz," *EURASIP Journal on Wireless Communications and Networking*, vol. 12, May 2007.

[76] S. Akoum, O. El Ayach, and R. W. Heath, "Coverage and capacity in mmwave cellular systems," in *IEEE ASILOMAR Conference on Signals, Systems and Computers*, pp. 688–692, Nov. 2012.

[77] E. Torkildson, H. Zhang, and U. Madhow, "Channel modeling for millimeter wave MIMO," in *IEEE Workshop on Information Theory and Applications*, pp. 1–8, Jan. 2010.

[78] W. Roh, J. Y. Seol, J. Park, B. Lee, J. Lee, Y. Kim, J. Cho, K. Cheun, and F. Aryanfar, "Millimeter-wave beamforming as an enabling technology for 5G cellular communications: theoretical feasibility and prototype results," *IEEE Communications Magazine*, vol. 52, pp. 106–113, Feb. 2014.

[79] B. Yin, S. Abu-surra, G. Xu, T. Henige, E. Pisek, Z. Pi, and J. R. Cavallaro, "High-throughput beamforming receiver for millimeter wave mobile communication," in *IEEE Global Conference on Communications (GlobeCom)*, pp. 3802–3807, Dec. 2013.

[80] G. H. Song, J. Brady, and A. Sayeed, "Beamspace MIMO transceivers for low-complexity and near-optimal communication at mm-wave frequencies," in *IEEE International Conference on Acoustics, Speech and Signal Processing (ICASSP)*, pp. 4394–4398, May 2013.

[81] T. S. Rappaport and S. Sun, "Multi-beam antenna combining for 28 GHz cellular link improvement in urban environments," in *IEEE Global Conference on Communications (GlobeCom)*, pp. 3859–3864, Dec. 2013.

[82] Jinho Choi, "On coding and beamforming for large antenna arrays in mm-wave systems," *IEEE Wireless Communications Letters*, vol. 3, pp. 193–196, Apr. 2014.

[83] O. E. Ayach, S. Rajagopal, S. Abu-Surra, Z. Pi, and R. W. Heath, "Spatially sparse precoding in millimeter wave MIMO systems," *IEEE Transactions on Wireless Communications*, vol. 13, pp. 1499–1513, Mar. 2014.

[84] A. Alkhateeb, O. E. Ayach, G. Leus, and R. W. Heath, "Channel estimation and hybrid precoding for millimeter wave cellular systems," *IEEE Journal of Selected Topics in Signal Processing*, vol. 8, pp. 831–846, Oct. 2014.

[85] J. Ng and A. Manikas, "Diversely polarised arrays in DS-CDMA: A space-time channel estimation approach," in *IEEE International Conference on Acoustics, Speech and Signal Processing (ICASSP)*, vol. 3, May 2002.

[86] J. Ng and A. Manikas, "Polirisation-angle-delay estimation using crossed-dipole array for DS-CDMA systems," in *International Conference on Digital Signal Processing (DSP)*, July 2002.

[87] J. Ng and A. Manikas, "Polarisation-sensitive array in blind MIMO CDMA system," *Electronics Letters*, vol. 41, pp. 970–972, Aug. 2005.

[88] S. Supakwong, *Diversely Polarized Antenna Array Systems*. PhD thesis, Imperial College London, 2009.

[89] P. Chevalier, L. Albera, A. Ferreol, and P. Comon, "On the virtual array concept for higher order array processing," *IEEE Transactions on Signal Processing*, vol. 53, pp. 1254–1271, Apr. 2005.

[90] M. Willerton and A. Manikas, "Virtual linear array modelling of a planar array," in *Proceedings of IMA Mathematics in Defence*, vol. 2, pp. 15–21, Oct.

[91] H. Commin and A. Manikas, "Virtual SIMO radar modelling in arrayed MIMO radar," in *Sensor Signal Processing for Defence*, no. 3, Sept. 2012.

[92] R. Schmidt, "Multiple emitter location and signal parameter estimation," *IEEE Transactions on Antennas and Propagation*, vol. 34, pp. 276–280, Mar. 1986.

[93] A. Manikas and M. Sethi, "A space-time channel estimator and single-user receiver for code-reuse DS-CDMA systems," *IEEE Transactions on Signal Processing*, vol. 51, pp. 39–51, Jan. 2003.

[94] A. Manikas and M. Sethi, "Joint multipath delay and direction tracking for CDMA array systems," in *IEEE Vehicular Technology Conference*, vol. 1, pp. 175–179, May 2002.

[95] A. Manikas and L. Huang, "STAR channel estimation in DS-CDMA communication systems," *IEE Proceedings - Communications*, vol. 151, pp. 387–393, Aug. 2004.

[96] T. S. Naveendra and A. Manikas, "Spatio-temporal array (STAR) DS-CDMA systems: Localized scattering channel estimation," in *IEEE Global Telecommunications Conference*, vol. 1, pp. 399–403, Nov. 2002.

[97] T. S. Naveendra and A. Manikas, "Blind estimation of diffused multipath vector channels for DS-CDMA systems," in *International Symposium on Wireless Communication Systems*, pp. 41–45, Sept. 2004.

[98] F. Rashid and A. Manikas, "Arrayed MC-CDMA Reception in Space-Time Diffused Multipath Vector Channels," *Wireless Communications and Mobile Computing Journal*, vol. 8, pp. 575–584, June 2008.

[99] F. Rashid, H. H. Peh, and A. Manikas, "Diffused Channel Estimation and Reception for Cyclic Prefix-free MC-CDMA Arrayed-MIMO Communication Systems," *International Journal of Wireless Information Networks*, vol. 15, pp. 148–160, Aug. 2008.

[100] L. Huang and A. Manikas, "Space-Doppler parameter estimation for space-time-Doppler reception in time-varying multipath DS-CDMA systems," in *International Conference on Digital Signal Processing Proceedings (DSP)*, vol. 2, pp. 1309–1312, 2002.

[101] Z. Chen and A. Manikas, "Direction-of-departure estimation using cooperative beamforming," in *International Symposium on Wireless Communication Systems*, pp. 120–124, Sept. 2010.

[102] Z. Chen and A. Manikas, "Joint space-time transmitter-receiver beamforming," in *IEEE Global Telecommunications Conference (GlobeCom)*, Dec. 2010.

[103] H. H. Peh, A. Manikas, T. Tjhung, and W.-c. Wong, "Joint transmitter-receiver beamforming in downlink cyclic prefix-free spatio-temporal MC-CDMA," in *IEEE International Conference on Communications (ICC)*, pp. 1–6, June 2009.

[104] T. Zhang and A. Manikas, "Joint transmitter-receiver beamforming over space-time fading channels," *IEEE International Conference on Communications*, pp. 4913–4918, June 2007.

[105] S. Affes and P. Mermelstein, "A new receiver structure for asynchronous CDMA: STAR-the spatio-temporal array-receiver,"

IEEE Journal on Selected Areas in Communications, vol. 16, pp. 1411–1422, Aug. 1998.

[106] G. Efstathopoulos and A. Manikas, "Extended array manifolds: Functions of array manifolds," *IEEE Transactions on Signal Processing*, vol. 59, pp. 3272–3287, July 2011.

[107] P. D. Karaminas and A. Manikas, "Super-resolution broad null beamforming for cochannel interference cancellation in mobile radio networks," *IEEE Transactions on Vehicular Technology*, vol. 49, pp. 689–697, May 2000.



Imperial College London

Department of Electrical and Electronic Engineering